NTNU – Trondheim
Norwegian University of
Science and Technology

Chitosan-based siRNA delivery to rat brain endothelial and glioma cells for optimization of P-glycoprotein knockdown in vitro

Christian Winther Wold

Biotechnology

Supervisor: Kjell Morten Vårum, IBT
Co-supervisor: Sabina Strand, IBT

Norwegian University of Science and Technology
Department of Biotechnology

Christian Winther Wold

Chitosan-based siRNA delivery to rat brain endothelial and glioma cells for optimization of P-glycoprotein knockdown *in vitro*

Master of Science Thesis
Trondheim, Norway – May 2012

Norwegian University of Science and Technology
The Faculty of Natural Sciences and Technology
The Department of Biotechnology

Academic Supervisors: Kjell Morten Vårum
                      Sabina P. Strand
                      Jostein Malmo

Preface

This Master of Science thesis in biotechnology was submitted to the Department of Biotechnology belonging to the Faculty of Natural Sciences and Technology at the Norwegian University of Science and Technology. The experiments were performed within the Department of Biology, the Department of Physics, as well as the Department of Laboratory Medicine, Children´s and Women´s Health in the time period September 2011 to April 2012.

Trondheim, May 14, 2012

_____

Christian Winther Wold

Abstract

The purpose of this thesis was to investigate the transfection efficiencies of chitosan-siRNA nanoparticles in the two rat brain-derived cell lines C6 and RBE4. Furthermore, the main goal was to silence P-glycoprotein (P-gp) expression in these cell lines and to assess the possibility of implementing them in a future glioma-blood-brain barrier (BBB) model *in vitro*. Finally, previously developed serum-stable chitosans were screened for transfection efficiencies in the RBE4 cell line to evaluate their potential in *in vivo* applications.

Linear (LIN350) and self-branched (SB300) chitosans were tested for their transfection efficiencies in the C6 glioma cell line. Uptake of the nanoparticles was measured using fluorescent siRNA by flow cytometry. Knockdown of GAPDH was measured using a GAPDH protein activity assay, and P-gp knockdown was measured by flow cytometry using a Rhodamine123 (R123) efflux assay.
The uptake efficiency was optimal at N/P ratio 30 and with a siRNA concentration of 100 nM. SB300 was more cytotoxic than LIN350, as indicated by the decrease in GAPDH protein activity when using negative control siRNA. It was found by reverse transcriptase PCR (RT-PCR) that the C6 cells did not initially express the *Abcb1a* gene, but expression was initiated after several passages in cell culture. The results show that the C6 cell line has the potential to be implemented in a future glioma-BBB model, however there is a need for optimization of the transfection when using chitosan-siRNA nanoparticles for P-gp silencing in this cell line.

Rat Brain Endothelial (RBE4) cells were used as an *in vitro* BBB-model, and several chitosans were investigated in regards to transfection efficiencies in this cell line. LIN350 and SB300 mediated efficient transfection at N/P 30 and a siRNA concentration of 100 nM. An uptake kinetics experiment was also carried out showing that the siRNA is removed within two days from RBE4 cells when using these chitosans. From a P-gp knockdown kinetics experiment measuring R123 efflux, it was found that repeated transfection with LIN350-based nanoparticles prolonged the knockdown of P-gp. LIN350 was used for transfecting confluent RBE4 cells; mediating knockdown efficiencies of GAPDH comparable to non-confluent cells. This indicates that RBE4 cells could be used as endothelial cells in a future glioma-BBB model.

In addition to LIN350 and SB300, several modified chitosans with increased serum stability ((DP_{85} (4AM), $F_a=0$ (2% PEG) and chitosans coated with hyaluronic acid (HA)), developed for efficient *in vivo* siRNA delivery were screened for their *in vitro* transfection efficiencies, measuring uptake, GAPDH protein activity and R123 efflux. The serum-stable chitosans mediated high uptake but did not produce RNA interference (RNAi), indicating that these chitosans need further modifications before they can be utilized for *in vivo* experiments.
It was found by transmission electron microscopy (TEM) that nanoparticles with LIN350, LIN350 w/HA, DP_{85} (4AM) and $F_a=0$ (2% PEG) were internalized by the RBE4 cells in vesicles larger than 500 nm, indicating that macropinocytosis is a highly possible uptake mechanism utilized by these chitosans. LIN350 was the only chitosan among these formulations that mediated RNAi, and the TEM showed that this chitosan is taken up in large aggregates, possibly bursting the vesicles by osmotic swelling.

Sammendrag

Hensikten med denne oppgaven var å undersøke transfeksjoneffektiviteten til kitosan-siRNA-nanopartikler i de to rottehjerne-baserte cellelinjene C6 og RBE4. Det overordnede målet var å hemme ekspresjonen av P-glykoprotein (P-gp) og å undersøke om disse cellelinjene kunne implementeres i en fremtidig glioma-blod-hjernebarriere-modell (glioma-BBB-modell) *in vitro*. Tidligere utviklede serum-stabile kitosaner ble også testet for transfeksjonseffektivitet i RBE4-celler for å undersøke hvorvidt de kunne benyttes for framtidige *in vivo* studier.

Transfeksjonseffektiviteten til lineære og selv-forgreinede kitosaner (LIN350 og SB300) ble undersøkt i C6 glioma-celler. Opptak av nanopartikler ble målt ved flowcytometri ved bruk av en fluoriserende siRNA. Knockdown av GAPDH ble målt ved hjelp av en GAPDH proteinaktivitets-analyse, og grad av P-gp knockdown ble bestemt ved å måle Rhodamine123 (R123)-effluks ved flowcytometri.
Det mest effektive opptaket av nanopartiklene ble funnet ved N/P-forhold 30 og en siRNA-konsentrasjon på 100 nM. SB300 var mer toksisk enn LIN350, målt ved nedgang i GAPDH proteinaktivitet ved bruk av negativ kontroll siRNA. Ved å bruke revers-transkriptase PCR (RT-PCR) ble det vist at C6-cellene ikke uttrykket genet *Abcb1a* i tidlige passasjer, men at det etter noen uker i cellekultur begynte å uttrykkes. Resultatene viser at C6-cellelinjen har potensiale til å bli implementert i en framtidig glioma-BBB-modell, men at det er behov for å optimalisere transfeksjon med kitosan-siRNA-nanopartikler ytterligere for å effektivt inhibere P-gp i denne cellelinjen.

Cellelinjen RBE4 stammer fra endotelcellene i blod-hjerne-barrieren til rotter, og ble brukt som en *in vitro* BBB-modell for å undersøke transfeksjonseffektiviteten til ulike kitosaner. og LIN350 og SB300 ga god transfeksjon ved N/P 30 og en siRNA-konsentrasjon på 100 nM. Et opptaks-kinetikkforsøk ble utført, der det ble vist at to dager etter transfeksjon med nanopartikler var nivåene av intracellulær siRNA neglisjerbare ved bruk av LIN350 eller SB30 som vektor. Et P-gp knockdown-kinetikkforsøk ble utført ved å måle R123-effluks, og det ble vist at repetert transfeksjon med LIN350-siRNA nanopartikler forlenget hemmingen av P-gp-ekspresjon. LIN350 ble også brukt til å transfektere konfluente RBE4-celler, og gav en nedgang i GAPDH proteinaktivitet på linje med transfeksjon av ikke-konfluente celler. Resultatene indikerer at RBE4-celler kan implementeres som endotelceller i en framtidig glioma-BBB-modell sammen med C6-celler.
I tillegg til LIN350 og SB300 ble flere kitosaner med god serum-stabilitet (DP_{85} (4AM), F_a=0 (2% PEG) og kitosaner tilsatt hyaluronsyre (HA)) undersøkt for *in vitro* transfeksjonseffektivitet. Det ble målt opptak, GAPDH proteinaktivitet og R123-effluks for å finne ut om de modifiserte kitosanene kunne benyttes for framtidig *in vivo* siRNA-levering. Det ble vist at til tross for høyt opptak, gav ingen av dem effektiv RNAi, noe som tyder på at disse kitosanene har behov for ytterligere modifiseringer for å kunne benyttes for *in vivo*-eksperimenter.
Ved transmisjonselektronmikroskopi (TEM) ble det vist at nanopartikler med LIN350, LIN350 m/HA, DP_{85} (4AM) og F_a=0 (2% PEG) ble tatt opp av RBE4-celler i vesikler større enn 500 nm, noe som indikerer at makropinocytose er en sannsynlig opptaksmekanisme som blir benyttet av disse kitosanene. LIN350 var den eneste av kitosanene undersøkt ved TEM som gav effektiv RNAi, og det ble funnet at dette kan komme av at denne kitosanen blir tatt opp i store aggregater og muligens ødelegger de intracellulære vesiklene ved å øke det osmotiske trykket.

Abbreviations

4AM - GlcNAc-GlcNAc-GlcNAc-GlcNAc-2,5 anhydro-mannofuranose
BBB - blood-brain barrier
bFGF - basic Fibroblast Growth Factor
C6 – A rat glioma cell line derived from astrocytes
CME - Clathrin-dependent endocytosis
CNS – Central nervous system
CvME - Caveolae-dependent endocytosis
DMEM - Dulbecco´s Modified Eagle Medium
DNA - deoxyribonucleic acid
DPn – Number-average degree of polymerization
dsRNA - double stranded RNA
F_a - degree of acetylation
FBS - Fetal bovine serum
FI – Fluorescence intensity
GAPDH - Glyceraldehyde-3-phosphate dehydrogenase
GlcN - 2-amino-2-deoxy-β-D-glucopyranose
GlcNAc - 2-acetamido-2-deoxy-β-D-glucopyranose
HA – Hyaluronic acid
HBSS - Hank's balanced salt solution
HEPES (4-(2-hydroxyethyl)-1-piperazineethanesulfonic acid)
LINxxx - Linear chitosans, xxx denoting approximate DPn
MBG water – Molecular Biology Grade water
MEM-α – Minimal Essential Medium alpha
mRNA - messenger RNA
M_n – Number average molecular weight
M_w – Weight average molecular weight
NEAA - Non-essential amino acids
N/P - the ratio between amino groups in chitosan and phosphate groups in siRNA
NT - Non-targeting (siRNA), notation in figures
P-gp - P-glycoprotein
PBS - Phosphate-buffered saline
pDNA - plasmid DNA
PCR – Polymerase chain reaction
PEG - poly(ethylene glycol)
PEI - polyethyleneimine
PEST - penicillin-streptomycin
PLL - poly-L-lysine
RBE4 – A Rat Brain Endothelial cell line
R123 - Rhodamine123
RISC - RNA-induced silencing complex
RNA - ribonucleic acid
RNAi - RNA interference
RT-PCR – Reverse transcriptase PCR
siRNA - small interfering RNA
STEM – Scanning TEM
T - Targeting (siRNA), notation in figures
TEM - transmission electron microscopy

Table of Contents

1. Introduction

RNA interference (RNAi) is a post-transcriptional gene silencing process, where short RNA molecules such as short interfering RNA (siRNA) and micro RNA (miRNA) bind to mRNA templates with a complementary sequence to silence their expression. Although a conserved endogenous mechanism for gene silencing in all eukaryotic cells, RNAi can also be exploited therapeutically by introducing synthetically produced double-stranded RNA oligonucleotides such as siRNA to cells, with the goal being to inhibit the expression of unwanted genes. This gives a huge potential for the treatment of many diseases, since virtually all genes with a known mRNA sequence could be targeted, such as cancer-promoting genes or genes that cause inheritable diseases.

However, the delivery of exogenous naked siRNAs *in vivo* is generally hampered by rapid degradation in the blood serum by endonucleases. This has been circumvented by the introduction of delivery vectors, which can protect the siRNA molecules from the environment. Different approaches have been attempted regarding this matter. One approach is to use viral vectors, which are considered potent vectors for gene therapy (using DNA) and to some extent RNAi, giving high transfection efficiencies. However, there are several safety issues associated with viral vectors, since they have the potential to produce unwanted immune responses and oncogenesis in the host. Therefore, nonviral vectors are gaining increased interest, especially cationic lipids and polymers. The ability of such cationic vectors to spontaneously form nanoparticles with negatively charged nucleic acids due to electrostatic interactions makes them promising agents for RNAi purposes. However, nonviral vectors still have low transfection efficiencies compared to viral vectors, and ways of resolving these matters are being sought out, for example by modifying the vector with molecules such as poly-ethylene glycol (PEG) to improve serum-stability and cellular uptake of the nanoparticles.

Chitosan, a biocompatible, biodegradable polymer derived from chitin, can be used as a cationic vector that due to its promising safety profile is being investigated for siRNA delivery. Chitosan is versatile biopolymer and can be modified in regards to chain length, degree of acetylation, self-branching of the chain and by substituting it with molecules such as PEG. Although extensive research has lead to improved *in vivo* delivery of chitosan-plasmid DNA (pDNA) nanoparticles, much has yet to be learned for the development of chitosan-siRNA formulations. Since siRNA is a much shorter molecule than pDNA, it requires chitosans with longer chains and a higher charge density for the complexes to become stable. Further, there is also a need for a proper balance between stability of the nanoparticle and intracellular release of siRNA to mediate an efficient mRNA knockdown. If the complex is unstable it cannot survive in serum *in vivo* and is not internalized by the target cells, but if too stable, it might not dissociate intracellularly, thus siRNA is not released, and cannot carry out the RNAi.
Still, chitosan-mediated siRNA delivery is hampered by the low solubility of the polymer at physiological pH and its poor buffering capacity in intracellular vesicles, giving low transfection efficiencies compared to other polymer vectors such as

Polyethyleneimine (PEI). In order to carry out RNAi, the siRNA must dissociate from the nanoparticles complex and escape the vesicles that they are internalized into. There are several ways cells can take up particles from their environment, such as clathrin-mediated endocytosis (CME), caveolae-mediated endocytosis (CvME) and macropinocytosis. These mechanisms internalize particles into vesicles such as endosomes, and they differ in the way they distribute their cargo intracellularly. However, the uptake mechanisms and intracellular trafficking routes of chitosan-siRNA nanoparticles have not been extensively studied, and since the release of siRNA from such vesicles is a crucial step for RNAi to occur, it is of great interest to determine what route is utilized for a given nanoparticle.

The blood-brain barrier (BBB) is a complex and dynamic structure which main purpose is to separate the brain and the blood system, protecting the central nervous system from harmful molecules circulating in the blood. Its main component is an endothelial cell monolayer with tight junctions that prevent xenobiotics and other unwanted substances from entering the brain by paracellular transport. In addition, drug efflux transporters on the apical side of the endothelial cell membranes will pump their substrates back out in the blood when they enter the cells, further restricting passage of such molecules into the brain. Unfortunately, this often prevents therapeutic drugs from reaching targets such as brain tumors. P-glycoprotein (P-gp) is an example of such an efflux transporter. P-gp is located in the cell membrane of various cells, including BBB endothelial cells. Moreover, tumor cells are often shown to overexpress P-gp, thus they can excrete chemotherapeutic drugs and reduce the chances of successful treatment. If using siRNA to target the mRNAs that are translated into P-gp, one can improve drug transport across the BBB, and for example increase the susceptibility of P-gp expressing brain tumors to therapy.

The experiments carried out herein served as an investigation of chitosan-mediated siRNA knockdown in two rat brain-derived cell lines – C6 and RBE4 – with the goal of giving efficient knockdown of P-gp in these cell lines. The C6 rat glioma cell line is astrocyte-derived and is often reported to display multi-drug resistance due to efflux pumps such as P-gp, while Rat Brain Endothelial (RBE4) cells are derived from rat BBB, thus serving as an *in vitro* BBB model. However, *in vitro* BBB models do not resemble the *in vivo* situation because of insufficiently tight junctions between the endothelial cells. One of the goals with this thesis was therefore to investigate these cell lines in regards to chitosan-siRNA nanoparticle-mediated transfection efficiencies, with the hope of implementing them by co-cultivation in a future *in vitro* glioma-BBB model with improved characteristics, since astrocytes can improve tight junction formation. Well-characterized linear and self-branched chitosans were tested for their ability to transfect both cell lines, and optimized in regards to N/P ratios and siRNA concentration. In addition, chitosans with increased serum-stability due to different modifications were screened for their efficiencies in RBE4 cells. Intracellular trafficking routes utilized by the chitosan-siRNA nanoparticles were also examined, using transmission electron microscopy.

Previous work in the RBE4 cell line has found that chitosan-siRNA nanoparticles with similar characteristics to some of the formulations used here mediated efficient P-gp knockdown in this cell line. This knowledge was therefore used when optimizing for transfection efficiencies. Chitosan-based siRNA delivery in C6 cells has not been previously described in the literature, and was demonstrated for the first time herein.

2. Theory

2.1 RNA interference

The discovery that RNA molecules beyond the traditional mRNA, tRNA and rRNA have biological importance revolutionized the understanding of how the cellular machinery works on the gene regulatory level. Since the Nobel Prize-winning discovery of mRNA degradation by short interfering RNA (siRNA) in 1998 [1, 2], numerous types of short non-coding RNAs have been added to this new exciting RNA world. These include the now well-know siRNA and microRNA (miRNA), but new discoveries and inventions are frequently made, such as short-hairpin RNA (shRNA), small nucleolar RNA (snoRNA) and piwi-interacting RNA (piRNA) [3, 4].

RNA interference (RNAi) is a post-transcriptional gene silencing process [5] in which a small RNA oligonucleotide binds to an mRNA target with a complementary sequence, either degrading the target completely or temporarily silencing its translation into a protein [6]. The main executors of RNAi are siRNA and miRNA. There is currently some confusion in the literature regarding the similarities and differences between siRNA and miRNA [7]. The most important distinction between the two is their difference in biogenesis and not necessarily in function [8]. In general, siRNAs are thought to have an exogenous origin (viruses, transposons, clinically introduced etc.), and are normally completely complementary to their mRNA targets, thus binding them strongly and degrading them [7]. miRNAs are endogenous molecules encoded by genes, and are often only partially complementary to their mRNA targets, thus they temporarily prevent their mRNA targets from being translated but might not degrade them (Figure 2.1) [7, 9]. Because of this difference in sequence specificity, one siRNA molecule usually has only one mRNA target, while one single miRNA molecule may target up to several hundred different mRNA templates [9, 10]. However, any siRNA molecule can have partial complementarity to other mRNAs and may repress their translation but not lead to cleavage of the mRNA strand, while some miRNAs can have perfect complementarity to their mRNA targets and thus degrade them [7].
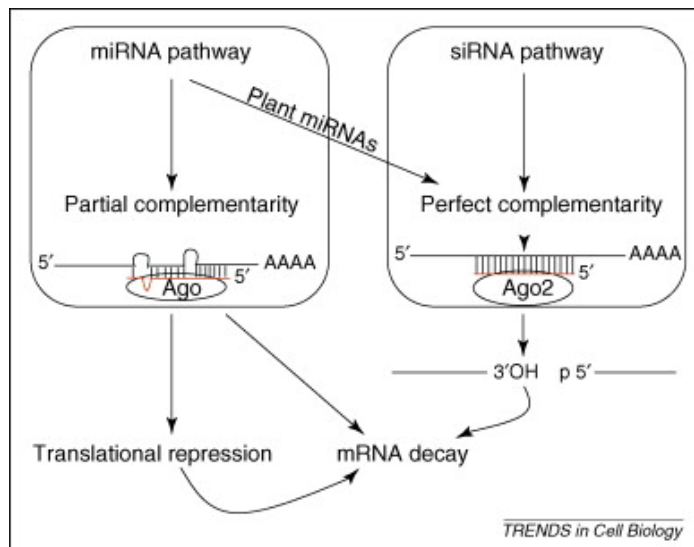
Figure 2.1: The main difference between the miRNA and siRNA pathways. miRNA usually shows only partial complementarity to its mRNA target, which leads to translational repression, while the siRNA pathway leads to degradation of the mRNA. In plants, miRNAs often show characteristics similar to animal siRNAs [9].

In eukaryotic cells, the siRNA based RNAi pathway begins when the RNA specific endonuclease Dicer recognizes and binds a long double-stranded RNA (dsRNA) molecule [11]. Dicer cleaves the dsRNA into a short siRNA of approximately 21 base pairs (bp), which when present in the cytosol is being recognized by a multi protein complex called RNA-induced silencing complex (RISC), as shown in Figure 2.2 [11]. The siRNA-RISC association results in siRNA strand dissociation, retaining only the antisense strand, which is complementary to the mRNA target. Argonaute proteins (for example AGO2) - the catalytically active RNases in RISC - are responsible for siRNA loading and mRNA degradation (Figure 2.2). Once a siRNA molecule is loaded onto RISC, the complex may degrade many copies of the target mRNA in a catalytic fashion, explaining the relatively high efficiency of the RNAi pathway [11].
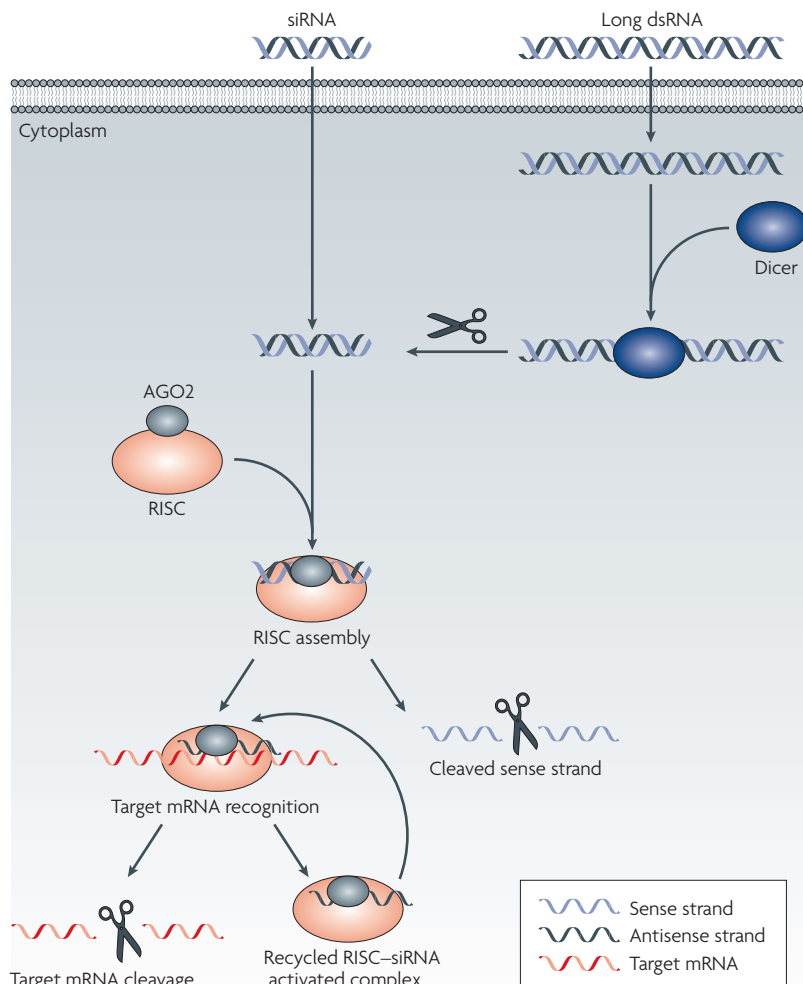
Figure 2.2: RNAi carried out by siRNA. The siRNA may either be produced by the Dicer pathway, or by transfecting the cell with an exogenously derived siRNA duplex. When the siRNA present in the cytosol is recognized by RISC, the siRNA duplex dissociates and the sense strand is cleaved by AGO2. The RISC-siRNA complex then binds and degrades its mRNA target [11].

Although siRNAs usually have short intracellular half-lives of only hours or a few days, depending on factors such as cell type and siRNA design, the catalytic activity of the RISC-siRNA complex may give knockdown effects 3-7 days after transfection in rapidly dividing cells and up to several weeks in non-dividing cells [12]. If siRNA is used clinically, repeated administration is required for prolonged effect because siRNA is eventually degraded or diluted below therapeutic concentrations due to cell division [11, 13, 14, 15].

siRNAs are usually produced synthetically and introduced into cells as a "ready" product of approximately 21 base pairs (bp). This makes it possible to bypass Dicer processing of dsRNA, and more importantly it minimizes the risk for sequence non-specific responses such as the interferon response often observed *in vivo* when long dsRNA is used for RNAi purposes [16].

Due to its half-life in serum of less than 5 minutes [112], many companies put a lot of research effort into chemical modifications of siRNA, with some of the goals being to

enhance the delivery efficiency, decrease potential immune responses in the host and decrease non-specific binding of the siRNA intracellularly [17, 18]

Many modified siRNAs show promising properties, for example in regards to increased serum stability, but prolonged half-life of siRNA intracellularly does not necessarily improve silencing efficiency. This is especially true for rapidly dividing cells because the dilution of siRNA due to cell division will eventually minimize knockdown efficiencies [12].

2.2 Vectors for nucleic acid delivery

Currently, the main obstacles associated with using nucleic acids (DNA or RNA) as therapeutic agents are serum instability, lack of efficient and specific uptake into the target cells and intracellular release from endosomes [19]. Although some reports of successful local delivery of naked siRNA exist for organs such as lung and nose [18, 20], the general consensus is that a delivery vector is needed in order to produce an efficient RNAi response since synthetically produced siRNAs are rapidly degraded in the blood serum by endogenous nucleases and cannot easily cross the cell membrane due to their high negative charge and large size of approximately 13 kDa [11].

Research is therefore currently focused towards developing non-toxic, biodegradable and cell-specific vectors that can deliver nucleic acids such as siRNA to cells with high uptake efficiencies and subsequent release of the siRNA from the endosomes [19].

Using such vectors to deliver nucleic acids into eukaryotic cells with subsequent gene insert or mRNA knockdown is generally defined as transfection (non-viral delivery) or transduction (viral delivery) [21, 22].

2.2.1 Viral vectors

Viral vectors such as adeno- and retroviruses have been used to introduce nucleic acids into cells [23]. Briefly, the undesirable viral genes are removed from the virus and genes of interest are introduced artificially [24]. However, although viral vectors are considered potent gene delivery vessels with high uptake and knockdown efficiencies, the use of these vectors has raised several safety issues, including unwanted immune responses, mutagenesis and oncogenesis [25, 26].

Development of nonviral vectors for siRNA delivery has therefore gained increased interest, with the main attention drawn towards cationic lipids and polymers [19, 25, 27].

2.2.2 Lipid-based vectors

Several cationic lipids can spontaneously aggregate with DNA or siRNA, binding along their surface to form lipoplexes [28, 29] Such lipoplexes can easily associate with the cell membranes due to their cationic and lipophilic character, and are

internalized by endocytosis and will subsequently release the nucleic acids into the cytosol by various mechanisms [21, 30]. Neutral, anionic and cationic lipoplexes have been developed for nucleic acid delivery [21, 30, 31], with the cationic versions showing greater therapeutic potential due to better association with the nucleic acids and higher cellular uptake over the anionic cell membrane [19]. In spite of promising features many lipoplexes show poor toxicity profiles and other health issues have also been addressed [32, 33]. Most lipoplexes are therefore still best suited for *in vitro* experiments.

2.2.3 Polymer-based vectors

Cationic polymers such as polyethyleneimine (PEI), Poly-L-Lysine (PLL) and chitosan can spontaneously form polyplexes (nanoparticles) with DNA or siRNA due to the strong charge interaction between the cationic polymers and the anionic nucleic acids [19, 21, 25, 34].

The relatively small size (in the nanometer scale) and compact packaging of these nanoparticles can prevent serum degradation of the nucleic acids and increase the cellular uptake [27,35]. However, polymer-based nanoparticles are often associated with low transfection efficiencies when used for nucleic acid delivery [21,32].

The tailoring of the polymers with regard to chain length, charge density and chain architecture can to some extent resolve these issues [19, 36, 37], but cationic polymers often show a correlation between cellular toxicity and transfection efficiency [36].

While PEIs give fairly good transfection efficiencies for nucleic acids both *in vitro* and *in vivo*, they are generally considered very cytotoxic at high doses [38]. The mechanisms behind the toxicity are not fully understood but seem to be dose-dependent, with self-branching low molecular weight PEIs (<25 kDa) showing less toxicity than longer chain PEIs [19, 38].

Chitosans on the other hand have an excellent safety profile, as they are considered non-toxic, biocompatible, and biodegradable, but they often show limited transfection efficiency due to low charge density at physiological pH [36].

2.2.3.1 Chitosan

Chitin is a polysaccharide mainly found in the outer skeleton of insects and crustaceans (shrimps and crabs etc.) and the cell walls of certain fungi [39, 40]. It consists mainly of repeating units of β(1-4) linked *N*-acetyl-D-glucosamine (GlcNAc) monomers, making it resemble cellulose in its basic structure but with acetyl instead of hydroxyl in the C-2 position [39, 40]. The polymer chain in chitin is very stiff due to hydrogen bonds between the hydroxyl group and the oxygen of the acetyl group on the neighboring monomer (Figure 2.3) [39].

Chitosan is a large family of co-polymers made from chitin by partial or full deacetylation of the acetyl groups converting them to amino groups (NH$_2$), creating D-glucosamine (GlcN) monomers from GlcNAc by enzymatic conversion as shown in Figure 2.3.
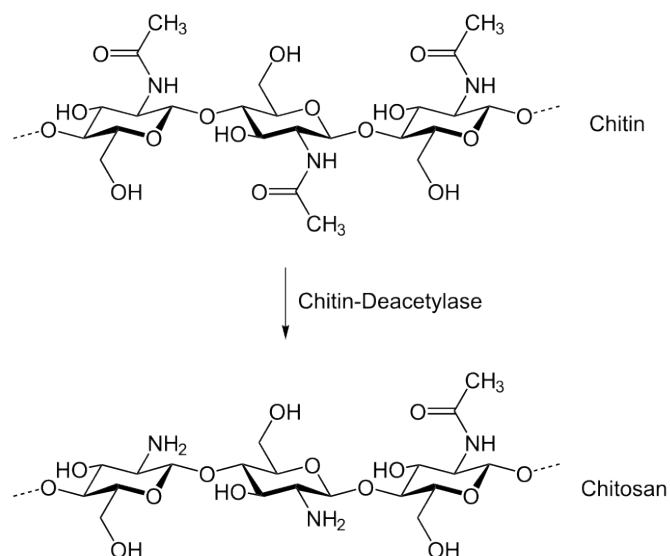
Figure 2.3: The enzymatic conversion of chitin into chitosan by chitin deacetylase. The polymers only differ at the C-2 position where most of the acetyl (–NHCOCH$_3$) groups in chitin are deacetylated into amino (-NH$_2$) groups in chitosan [41].

The deacetylation leads to disruption of the internal hydrogen bonds found in chitin, giving chitosan a more flexible, random coil polymer structure [39]. The amino groups are pH sensitive and are either in a protonated or deprotonated form, with a pK$_a$ of about 6,5 as seen from the following equation:

-NH$_3^+$ ⇌ -NH$_2$ + H$^+$ pK$_a$ ~ 6.5 (for F$_A$ =0.01)   [39, 42]
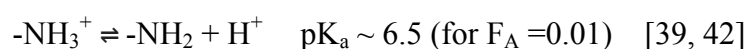
The cationic amino groups make it possible for chitosan to spontaneously form complexes with negatively charged molecules such as nucleic acids and the polymer can therefore be used as a delivery vector in gene therapy and RNAi [40].

A pK$_a$ value of 6.5 indicates that at this pH, about 50 % of the amino groups are protonated and thus positively charged. Below this value chitosan is fully water-soluble but as pH increases more –NH$_3^+$-ions lose their charge, making chitosan less water-soluble at physiological pH (7.4), and less likely to bind anions [36, 43].

Because chitosan has a higher charge density in acidic pH and therefore interact more strongly with nucleic acids such as siRNA, the pH is important to consider when using chitosan for siRNA delivery as it governs how stable and soluble the nanoparticles are both extra- and intracellularly [36, 44].

Chitosan has different characteristics depending on the degree of acetylation (F$_A$), number-average degree of polymerization (DP$_n$), number-average molecular weight

(M_n), weight-average molecular weight (M_w), Polydispersity index (PDI = M_w /M_n) and molecular architecture [36, 39, 44, 45]. Since DP_n, M_n and M_w are average numbers, a given chitosan will have polymer chains with different chain lengths and sizes if the PDI (or M_w/M_n) $\neq 1$ [39].

There are also other factors that influence transfection efficiency, such as the cell type targeted and if the nucleic acid of interest is plasmid DNA (pDNA) or siRNA [44].

It is of interest that chitosan and siRNA interact strongly enough to prevent extracellular dissociation, but the interaction should not be too strong either as this might prevent the siRNA to be released from the complex intracellularly [44]. In contrast to chitosan-pDNA nanoparticles, which can be formed with low M_w chitosans (5-10 kDa) [37, 44], chitosan-siRNA nanoparticles require chitosans with higher molecular weight (above 35 kDa) in order to form stable complexes and give a knockdown effect [45, 46].

Self-branching chitosans have been reported to mediate good transfection efficiencies on gene transfer with pDNA [47] and to some extent with siRNA [45]. Nevertheless, linear medium-sized and fully de-N-acetylated chitosans are currently associated with the highest transfection efficiencies for siRNA delivery, but this may vary among different cell lines [45].

Further, the ratio between chitosan amino groups and siRNA phosphate groups (N/P) may influence nanoparticle stability and size. Higher N/P ratios produce larger nanoparticles when comparing linear chitosans at N/P 10, 30 and 60 [45] and there seems to be a correlation between increased N/P ratio and stability and cellular uptake of the nanoparticles [44, 46].

Because of chitosan's relatively low solubility in aqueous solutions, poor endosomal buffering capacity, lack of cell-specificity and the potential of clearance from blood serum due to aggregation with negatively charged particles and subsequent opsonization by phagocytes [44, 48], ways of modifying the polymer chain have been investigated.

To address the solubility issue, novel chitosan structures such as trimethyl-chitosan (TMC) have been developed with successful outcome, but challenges regarding toxicity still need to be addressed [49]. Substitution of the GlcN amino group in chitosan using the trimer GlcNAc-GlcNAc-2,5 anhydro-mannofuranose (AAM) with different degrees of substitution (d.s.) has also been investigated, resulting in chitosan conjugates with increased solubility at all pH values and increased uptake in HEK293 cells, possibly due to association with cell-membrane lectins and increased colloidal stability (resistance to aggregation) [50, 51].

Polyethylene glycol (PEG) is one of the most characterized modification ligands for nucleic acid delivery. PEGylation refers to the process of attachment of PEG molecules to chitosan or other delivery vectors [44]. The attachment of PEG to nanoparticles has been shown to give numerous positive effects on gene delivery such as increased serum stability and circulation time [52], decreased inter-particular aggregation [53], low toxicity [53] and increased transfection efficiency [54].

Further, several different ligands can be attached to chitosan in order to increase cell specificity through receptor-mediated endocytosis, including transferrin, folic acid [44] and hyaluronic acid [55, 56]. Folic acid in particular is a promising ligand and has been shown to improve the transfection efficiency and cytotoxicity profiles for chitosan-DNA nanoparticles [57].

2.3 Uptake and intracellular trafficking of nanoparticles

In order to release nucleic acids intracellularly, nanoparticles must first be taken up and internalized by the cells [27]. The main mechanisms of uptake are presented in Figure 2.4.
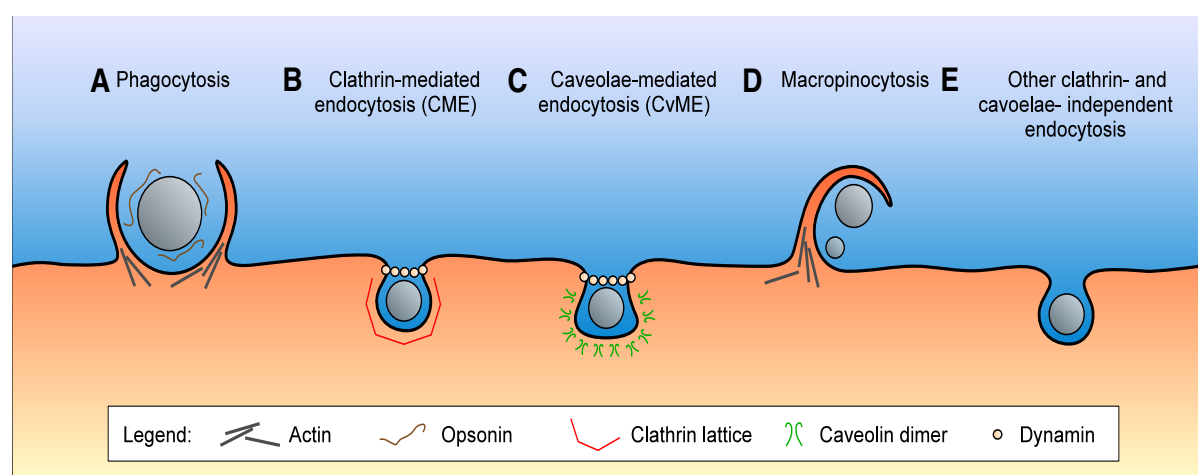
Figure 2.4: The main mechanisms behind nanoparticle uptake in cells. A: The particle is taken up by phagocytosis, most commonly by phagocytes such as macrophages. B: Clathrin-mediated endocytosis (CME), which leads to formation of a clathrin lattice around the endosome. CME can be either receptor-dependent or independent. C: Caveolae-mediated endocytosis (CvME) occurs in flask-shaped invaginations where caveolin dimers are located below the cell membrane. D: Macropinocytosis is dependent on actin and operates with poor selectivity, creating large vesicles. E: Other endocytosis mechanisms independent on clathrin and caveolae can also internalize nanoparticles [27].

In most cell types, clathrin- and caveolae-mediated endocytosis and macropinocytosis are the most common mechanisms for nanoparticle uptake, but other pathways independent on clathrin and caveolin are currently being explored [58].
Phagocytosis is usually a mechanism used by immune cells such as macrophages, neutrophils and dendritic cells to internalize larger particles (0,5 μm and above), and will not be covered any further here [27].

Clathrin-mediated endocytosis (CME) occurs when nanoparticles associate with the cell membrane in a region rich in the coating protein clathrin. Clathrin molecules polymerize and form a basket-like structure that governs vesicle formation [27]. The rate and specificity of the endocytosis is dependent on the presence of ligands attached to the nanoparticles. If the nanoparticles are associated with ligands such as transferrin or epidermal growth factor (EGF), they can interact with membrane

components and the cellular uptake is more specific and faster than without ligands [27]. Usually CME creates vesicles with a size around 100-120 nm, which mature and eventually fuse with lysosomes as shown in Figure 2.5.

Caveolae-mediated endocytosis (CvME) is an alternative pathway to the more characterized CME. It usually creates small vesicles of around 50-100 nm when the dimer protein caveolin is present in the cell membrane, and is common in endothelial cells [27]. CvME is a highly regulated process with complex signaling and occurs at a much slower rate than CME. Interestingly, CvME does not lead to endosomal fusion with lysosomes and can therefore possibly be exploited by vectors such as chitosan to by-pass lysosomal degradation (Figure 2.5).

Macropinocytosis is a non-selective, actin-driven internalization process, which creates membrane protrusions that internalize extracellular fluids and particles such as nanoparticles in vesicles larger than 1 μm [27, 59]. Usually such macropinosomes acidify and shrink to fuse with lysosomes, or recycle their content to the surface of the cell by transcytosis (Figure 2.5) [27, 60]. Uptake of hydrophobically modified glycol chitosan nanoparticles by macropinocytosis was recently reported [61].
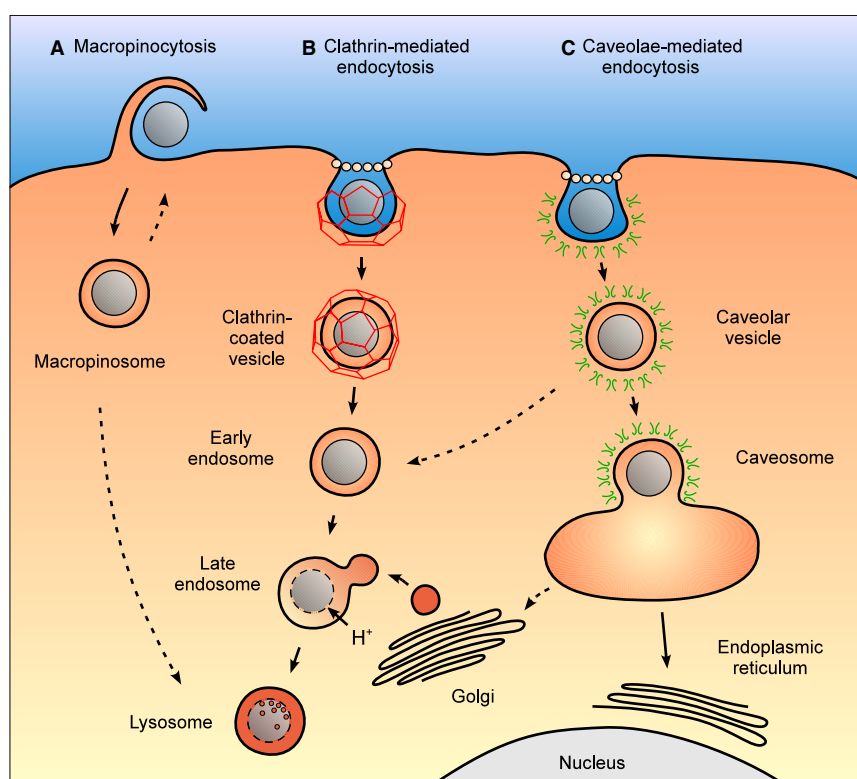
Figure 2.5: Intracellular trafficking of vesicles from A: Macropinocytosis, B: Clathrin-mediated endocytosis and C: Caveolae-mediated endocytosis. Usually both macropinosomes and clathrin-mediated endosomes acidify and fuse with lysosomes as they mature through the cytosol, while caveolar vesicles increase in size and interact with Golgi or endoplasmic reticulum, preventing enzymatic degradation of the internalized cargo [27].

Parameters such as size and surface charge of the nanoparticles may affect what intracellular trafficking pathway is used and the efficiency of association with the cell membrane, respectively. One study using fluorescent microspheres showed that

particles below 200 nm were internalized by clathrin-mediated endocytosis, with a shift toward caveolae-mediated endocytosis for bigger particles up to 500 nm [62], which is somewhat surprising since CvME usually are found to produce vesicles with smaller sizes [27]. As for surface charge, cationic polymers may spontaneously associate with components in the cell membrane such as negatively charged lipids, making internalization faster and more efficient [63].

If the nanoparticles are internalized via the CME pathway, and to some extent via macropinocytosis, they follow the endosomal/lysosomal pathway in the cytosol. Due to the presence of a proton pump in the vesicle membrane, the early endosomes or the macropinosomes become increasingly acidified as they venture through the cytosol and (for the CME pathway) mature into late endosomes with a pH around 5-6. Eventually the vesicles may fuse with lysosomes where the pH is even lower and the contents of the vesicles are degraded by lysosomal enzymes [27].

To mediate RNAi, it is crucial for the siRNA to escape the vesicles before fusing with the lysosomes. Cationic polymers with good buffering capacities at pH 4-7, such as PEI, can rupture such vesicles via the proton sponge effect [64, 65, 66, 67]. If the polymer has uncharged amine/amino groups it can take up the incoming H^+, acting as a sponge, which prevents acidification and leads to an even higher influx of H^+, and also Cl^- counter-ions to balance out the net positive charge. This gives higher ion concentration inside the vesicle, and water therefore flows into it, resulting in rupture due to osmotic swelling [66, 68]. In addition, it is speculated that the polymer may stretch out in size due to electrostatic repulsions between the now charged amine groups if not restrained by steric hindrances. Termed *the umbrella effect*, this hypothesis helps explain the potential increase in polymer size, which can contribute to the swelling and destruction of the vesicle [25]. Once the vesicle is ruptured, intact nanoparticles or free siRNA molecules are released into the cytosol. The siRNA molecules can now associate with RISC, but if the nanoparticles are still intact siRNA must dissociate from the complex in order to bind to RISC. However, in contrast to PEI, unmodified chitosan show poor buffering capacity in vesicles due to its low pK_a of 6.5. Chitosan-based nanoparticles are therefore thought to be more dependent on degradation of the polymer chain, which produce oligo- and monosaccharides and subsequent osmotic swelling so that the vesicular content can be released into the cytosol [64, 65].

2.4 The Blood-Brain Barrier

2.4.1. Structure of the Blood-Brain Barrier

In humans and animals such as rodents, the blood-brain barrier (BBB) is a complex, dynamic structure which main purpose is to separate the central nervous system (CNS) from the blood system and thus regulate the flow of molecules into the brain [69]. The structural basis of the BBB is a lining of endothelial cells where the cells are linked together by tight junctions efficiently blocking paracellular transport. The formation and maintenance of the tight junctions is dependent on signals and interactions from other cells, such as astrocytes, pericytes and neurons, as shown in Figure 2.6.
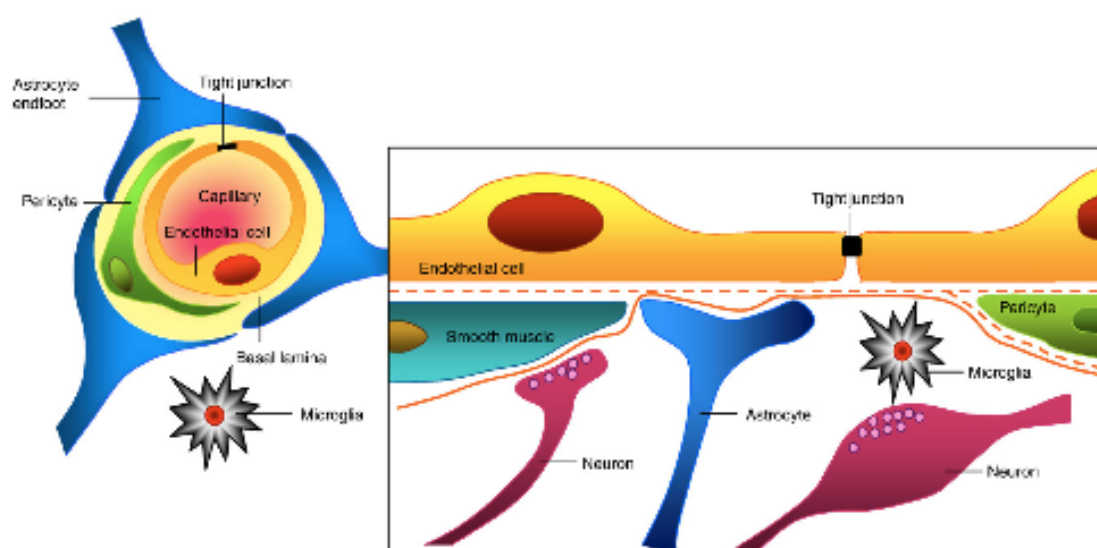
Figure 2.6: The structural composition of the BBB. Endothelial cells surround the blood capillaries, preventing solutes from freely entering the brain by tight junction formation. Pericytes are closely associated with the endothelial layer, while astrocytes create a structural network that surrounds the endothelial cells and are important for induction and maintenance of barrier properties such as tight junction maintenance. Axons from neural cells may interact with muscle cells close by to provide regulatory neurotransmitters and peptides. Microglia are immunocompetent cells in the brain that complements barrier functions [69].

The tight junctions of the BBB prevent small hydrophilic molecules from entering the brain via paracellular transport. The two ways that a substance may pass from the blood stream into the brain are therefore either via passive diffusion as small lipophilic substances may pass through the cell membrane, or receptor catalyzed transport [70]. However, studies have shown that although a given molecule/drug has the right chemical properties to pass through the BBB by passive diffusion, specific efflux transporters in the endothelial cell membrane often pump the molecule back into the blood stream. If a therapeutic drug with affinity for such efflux transporters is systemically introduced into a patient´s blood, it may therefore be unable to reach its therapeutic target [71, 72].

2.4.2. P-Glycoprotein

P-glycoprotein (P-gp) is an example of such efflux transporters present in the BBB endothelial cells. In humans P-gp is encoded by the gene *Abcb1*, while in rodents there are two genes for P-gp – *abcb1a* and *abcb1b* (also called *mdr1a* and *mdr1b*) – with partial overlapping substrate specificity, which combined replace the one gene found in humans [73]. P-gp is an ATP Binding Cassette transporter (ABC-transporter). Functioning as a multi-substrate ATP driven molecular pump, P-gp regulates the flow of substrates such as xenobiotics (chemotherapy drugs etc.) and endogenous substances in various tissues, including the BBB where its main role is to protect the brain from unwanted or toxic substances [74, 75]. In the BBB, P-gp is located in the apical cell membrane, which is in contact with the blood stream, but not in the basolateral membrane, which is connected to the CNS (Figure 2.7). Thus, P-gp always pumps its substrates back into the blood stream. Other efflux pumps, such as the Multidrug Resistance-associated Proteins (MRPs) are also present in the apical or basolateral cell membranes of BBB endothelial cells, where they protect the brain from unwanted substances. Furthermore, certain efflux proteins such as OAT3 are also present in the basolateral membrane to remove xenobiotics at the brain-side of the BBB (Figure 2.7) [76].
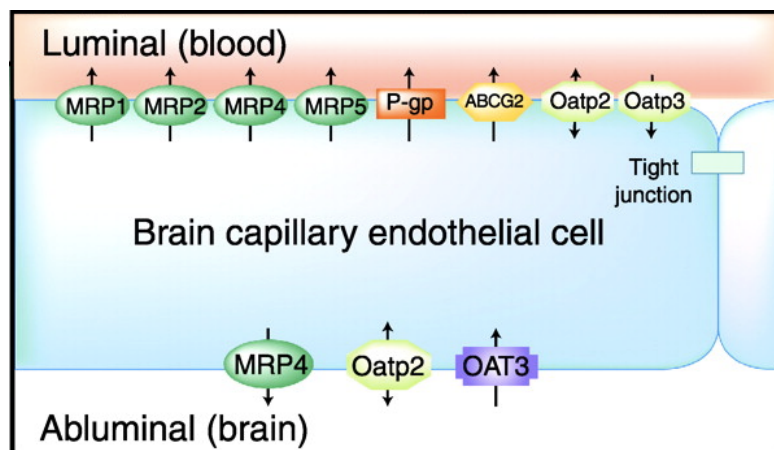
Figure 2.7: Transport proteins present in the apical (luminal) and basolateral (abluminal) membranes of endothelial cells in the blood-brain barrier. P-gp and MRP 1-5 as well as other protein pumps (e.g. ABCG2, Oatp2 and Oatp3) are located in the apical side of the endothelial cells, mainly preventing different molecules from entering the brain. Protein pumps are also present in the basolateral membrane, such as MRP4, Oatp2 and OAT3. These pumps will either transport molecules from brain to blood (OAT3, Oatp2) or vice versa (MRP4, Oatp2) [76].

Since many drugs have the potential to cure or treat diseases in the brain such as tumors and epilepsy but cannot enter their target site because of P-gp, attention has been drawn to how this transporter may be inhibited. Although several molecules (for example verapamil) are P-gp inhibitors [77], such drugs are usually toxic in large doses and may show poor inhibitory effects [78]. siRNA-mediated inhibition of the P-gp transporter may therefore provide novel, interesting attributes, since siRNA is generally considered non-toxic and may linger in cells for several days [11]. Also,

since a delivery vector most often is required for siRNA delivery, it might be possible to tailor the vector with ligands so that it specifically reaches its target, thus limiting the transfection of unspecific cells [44].

Many cancers including various brain tumors are shown to overexpress P-gp [79], which often confers multidrug-resistance to the tumors because P-gp pumps certain chemotherapy drugs back out of the cells upon entry [78, 80]. Further, these chemotherapeutic drugs will not easily enter the brain because of the presence of P-gp in BBB endothelial cells, and therefore a siRNA-mediated knockdown of P-gp is interesting in this regard since it may knock down P-gp expression in both the BBB and the tumor cells, thus making chemotherapy treatment more effective.

2.4.3 *In vitro* BBB models

Because it is difficult to investigate the BBB *in vivo*, it is of interest to develop *in vitro* BBB models that resemble the *in vivo* situation. The general principle is to use immortalized endothelial cells from a BBB cell line, which can create a cell monolayer when grown in a specialized environment [71]. One way of doing this is to grow endothelial cells on the apical side of a filter membrane in a two-chambered well, such as the transwell model, as shown in Figure 2.8. However, there are still severe limitations to such systems, especially due to lack of proper tightness of the tight junctions between the endothelial cells compared to the *in vivo* phenotype, creating a leaky monolayer that permits paracellular transport [71]. This could, at least to some degree, be overcome by co-culturing the endothelial cells with tight junction-inducing cell types such as astrocytes, which are found to improve tight junction formation in several endothelial cell lines both by means of structural support and from astrocyte-derived soluble factors [71, 81, 82]. If using a two-chambered well such as a transwell, one could thus grow astrocytes on the basolateral side of the filter or on the bottom of the well, hoping to reduce paracellular transport over the endothelial monolayer.
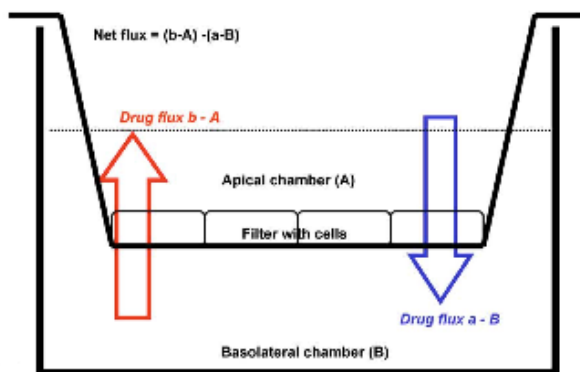
Figure 2.8: An in vitro BBB model using a transwell model, with a well consisting of an apical and a basolateral chamber. Endothelial cells are grown on a filter in the apical chamber, and drug flux is measured from both sides of the filter to determine the amount of paracellular transport of the drugs, given by the net flux. A second cell line, such as astrocyte cells, could be included in the model either grown on the bottom of the well or on the basolateral side of the filter (not shown) [71].

2.5 Experimental theory

2.5.1 Flow cytometry

Flow cytometry is a technique used for various biomedical purposes, including cell counting, -separation and –examination [83, 84].

Briefly, a flow cytometer is a machine that focuses light (usually laser beams) of specific wavelengths towards cells, which then scatter or fluorescence the incoming light, as shown in Figure 2.9 [85]. The principle of flow cytometry is based on a flowing suspension of particles, such as cells. Every cell is measured separately, giving flow cytometry unique properties. It is therefore possible to obtain statistical information of a large population of cells in a very short time [83].

The scattered light reflected by the cells provide information on their physical properties, and have the same wavelength as the incoming light, which is usually 488 nm. The Forward Scatter (FCS) is located in the forward direction along the path of the laser beam and detects the volume (size) of the cells. The side scatter (SSC) collects light that has been scattered in larger angles, and can give information on granularity and irregularities in cell membrane, cytoplasm and nucleus [83].
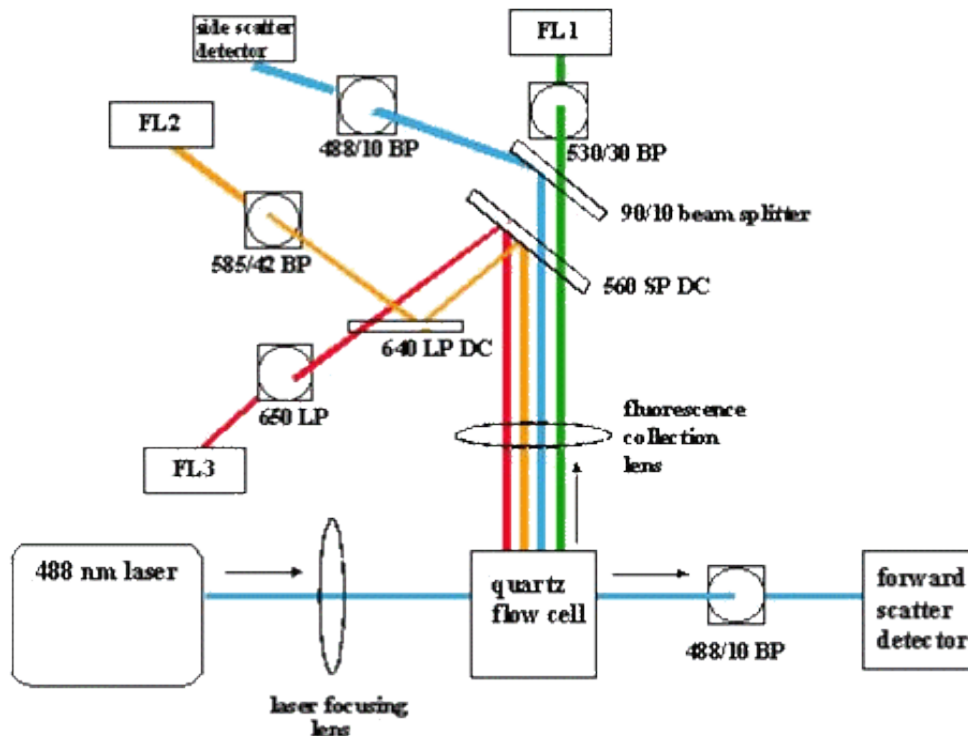
Figure 2.9: The general principle behind flow cytometry. A laser beam of a certain wavelength (e.g. 488 nm) is directed into a liquid suspension consisting of cells or large molecules. The laser beam is reflected or absorbed by the cells at a specific analysis point. When the light is scattered it is detected by the forward- and side scatter photodetectors, depending on the angle of the scattered light. Light can also be absorbed and emitted by fluorescent molecules or dyes and is then collected by wavelength specific detectors such as FL1, FL2 and FL3, depending on the wavelength of the emitted light. All detectors have wavelength specific lenses and filters to ensure accurate detection of the signals [85].

There are also detectors collecting light from fluorescent molecules, such as green fluorescent protein or rhodamine. When a photon from the laser beam hits such a fluorescent molecule, it is absorbed. An electron is then temporarily exited into a higher energy state, and when it goes back to its ground state, another photon with a different wavelength is emitted (usually with lower energy/longer wavelength than the absorbed light). In contrast to the detectors collecting scattered light (which are only sensitive to light intensity), the fluorescent light detectors contain wavelength specific filters and mirrors, ensuring that only light with a given wavelength is detected. This property makes it possible to obtain quantitative, phenotypic information about specific molecules or cells. For example, if a siRNA labeled with a fluorescent dye is introduced into a population of cells, a flow cytometer can measure and compare the relative amount of the intracellular siRNA between different samples. Modern flow cytometers usually have around 6-10 fluorescence detectors, each with its own wavelength specificity, making it possible to detect many fluorescent molecules at the same time [83, 84, 85].

The flow cytometer converts the light signals from the cell samples into data, usually presented in histograms, as shown in Figure 2.10. Each photodetector produces one histogram; therefore a huge amount of data is often generated in one experiment. The histograms are presented either in a linear scale (for example when measuring difference in cell volume) or a logarithmic scale (when there is a large difference in light intensities between samples, such as cells positive or negative for a specific fluorescent dye).
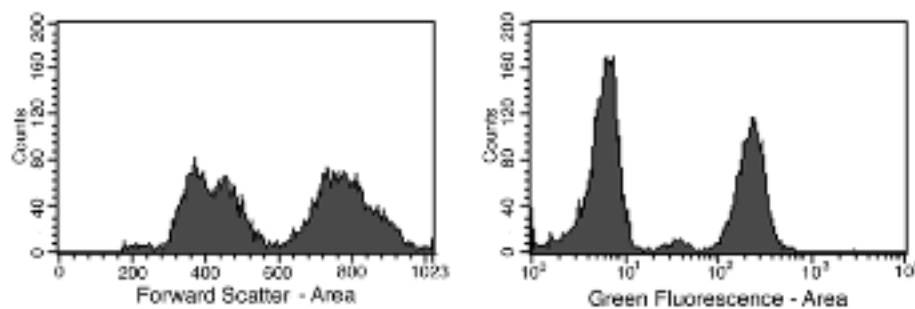
Figure 2.10: Histograms presenting light intensities from forward scatter light (left, showing a linear light intensity scale) and green fluorescence (right, showing a logarithmic light intensity scale). The columns represent the number of cells counted, the y-axis being the number of cells with a specific light intensity [83].

Another interesting feature of flow cytometry is the possibility of gating cells, which is used for filtering out unwanted cells from the analysis. For example, if cells contain some auto-fluorescence, one can use gating to exclude cells that have light intensities below this value.

2.5.2 Reverse transcriptase Polymerase Chain Reaction (RT-PCR)

Polymerase chain reaction (PCR) is a technique used in molecular biology to identify and amplify DNA sequences. The principle is based on a thermostable polymerase (for example Taq polymerase) that in the presence of site-specific primers and deoxynucleoside triphosphates (dNTPs) can make millions of copies of the DNA sequence of interest. For most PCR experiments, the primers are synthesized so that they completely match the DNA sequence, one forward and one reverse primer [86].

In the first step, the denaturation, the reaction is heated up to about 95°C so that the hydrogen bonds in the double-stranded DNA will break and give single-stranded DNA. Then, in the annealing step, the temperature is lowered to around 55°C-65°C so that single-stranded DNA and primers will anneal to each other. In the elongation step, the temperature is increased to the optimal working temperature for the thermostable polymerase. In presence of dNTPs and cations such as K^+ and Mg^{2+}, the polymerase binds to the DNA/primer sequence and start amplifying the DNA template. This process is repeated many times until enough DNA is obtained (usually 30-40 cycles) [86].

In modern quantitative real-time PCR (qrtPCR), the presence of fluorescent molecules (dyes) makes it is possible to follow the amplification process on a computer during the PCR reaction. The two most common techniques are based on either a DNA probe with a fluorescent dye and a quencher attached to it (Taqman® probes), or fluorescent dyes that bind the DNA directly (e.g. SYBR® Green), as presented in Figure 2.11 [87]. In a probe-based assay, a fluorescent dye and a quencher are attached to a DNA probe that is complimentary to a short sequence on the DNA template. As long as the DNA probe is not attached to its target, the quencher absorbs the fluorescent light because of its proximity to the reporter molecule. Only when the DNA probe binds the template, the 5´to 3´exonuclease activity of the polymerase will release both the quencher and the reporter, and these will now be sufficiently apart so that the fluorescent signal is not quenched but can be detected by the apparatus.
In a fluorescent dye-based assay, fluorescent molecules usually bind directly to all double-stranded DNA. When the DNA template is denatured, the fluorescent molecules are released and fluorescence is greatly reduced, and only upon generation of double-stranded PCR products will the dyes re-bind the DNA, resulting in a net increase in fluorescence that is detected by the apparatus (Figure 2.11) [86, 87].
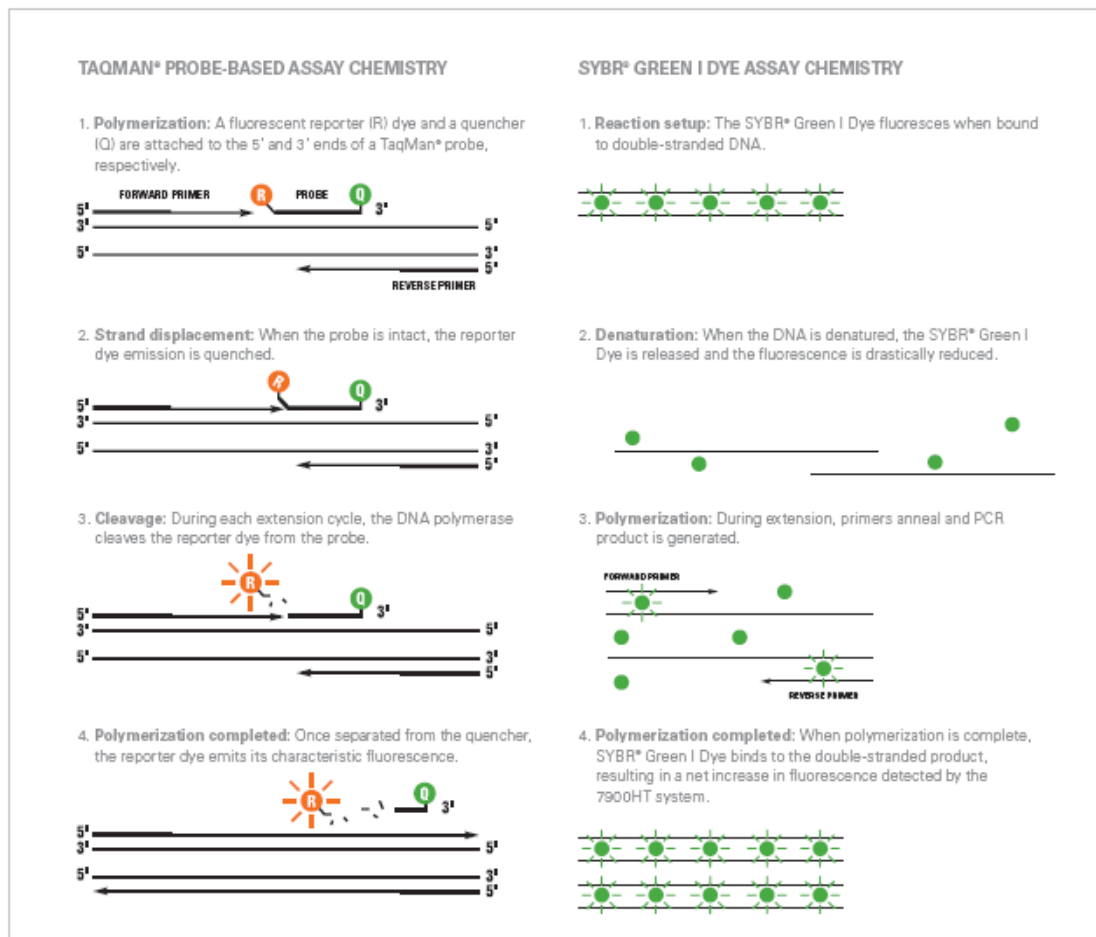
Figure 2.11: The general principle behind real-time PCR, using either a Taqman® probe-based assay or SYBR® Green 1 dye assay. In the probe-based assay (left) the DNA strands are separated before primers and a probe (bound to a fluorescent dye and a quencher) anneal to their complimentary strand. The polymerase will now start extending the DNA template and the fluorescent dye and the quencher separate so that the PCR machine can detect the fluorescence. In the SYBR® Green 1 dye assay (right), fluorescent molecules will bind all double-stranded DNA, before they are released upon denaturation. The process will be repeated for 30-40 cycles [87].

In reverse transcriptase PCR (RT-PCR) the principles are the same as in standard PCR, however the nucleic acid of interest is mRNA and not DNA. To be able to carry out the RT-PCR in a regular fashion, a DNase is often first added to the samples to remove all DNA. The samples are then treated with the enzyme reverse transcriptase. This enzyme reverts mRNA back to DNA in the form of cDNA, and the sample is ready for qrtPCR. cDNA differs from regular DNA in that they do not contain introns. The advantages of RT-PCR are obvious; many viruses such as HIV and influenza viruses have RNA based genomes, and RT-PCR has made it possible to copy up and isolate interesting genes from such medically important organisms. Further, while DNA only tells us about the *presence* of a certain sequence in the genome, the mRNA tells us if that sequence (gene) has been transcribed. Since RT-PCR most often is quantitative, the amount of mRNA can be found and therefore give indications of how much of a certain gene that is expressed by the cell [86].

2.5.3 Transmission Electron Microscopy (TEM)

A transmission electron microscope is a magnification device that uses electrons to magnify objects [88]. The principles behind it resembles traditional light microscopy, but is based on the fact that electrons have much shorter wavelengths than photons and can magnify object up to 2 million times, which is substantially higher than standard light-based optical microscopes (which can only magnify object up to 2.000 times). The resolution (the smallest distance that can be measured between two points) is also extremely high in TEM, giving detailed images. One can therefore use such an instrument to study the inner workings of cells, such as organelle morphology [88, 89].

In short, images are obtained when an electron source such as tungsten emits electrons into vacuum, which are focused into a beam and move through the apparatus before particles in the sample are hit and scatter the incoming electrons, as shown in Figure 2.12 [90].
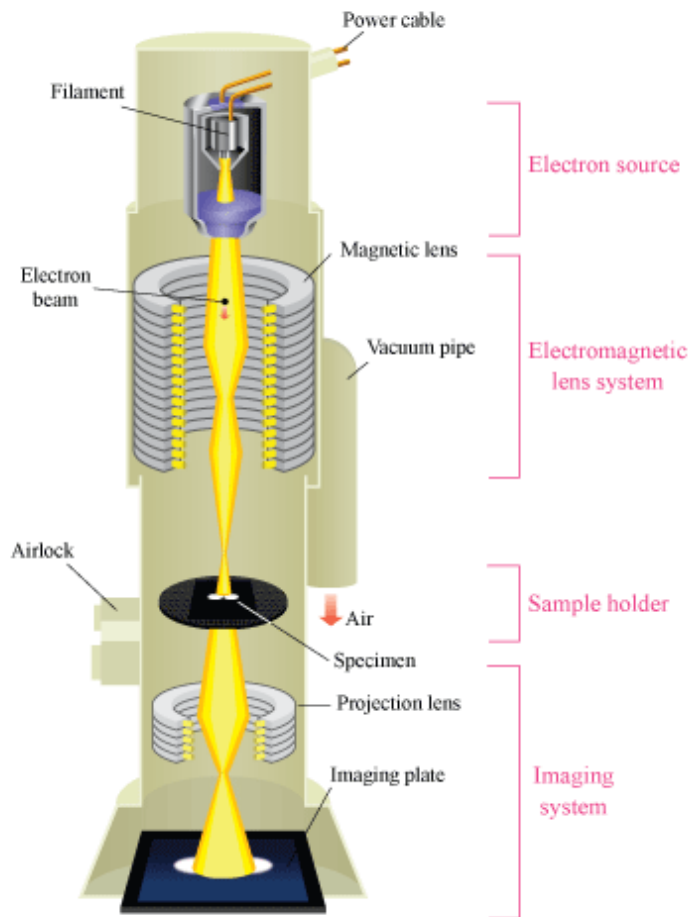
Figure 2.12: The general principle behind TEM. An electron source on top of the apparatus (the filament) emits electrons into a beam. The electron beam moves through vacuum and several lenses before it hits the sample (specimen) and magnifies it onto an imaging plate [90].

Below the sample is an imaging plate that detects the scattering or fluorescence produced from the specimen and give detailed images that can be obtained with a

camera. Several lenses, such as the magnetic lens and the projection lens work together to produce the high magnification and accurate resolution of the images (Figure 2.12) [88, 90]. It is important that the specimen is very thin since the electrons must pass through it to produce the image. Accordingly, cells are usually fixated and isolated in a thin plastic foil and put on a small grid (3 mm) before it the sample is analyzed [88].

It is also possible to scan specimens using Scanning TEM (STEM), which is an extension of TEM. This has several advantages, for example can the atomic numbers in a sample be determined with a high-angle detector if the electron beam is strong enough (using high voltage), and one can thus obtain information such as whether a specific atomic element is presence in the sample or not [88].

3. Materials and Methods

3.1 Cells, chitosans and siRNAs

C6 rat glioma cells and Rat Brain Endothelial cells (RBE4) were both supplied by Professor Tore Syversen (Dept. of Neuroscience, NTNU).

The chitosans used have been developed at the Dept. of Biotechnology (NTNU). All chitosans are presented and characterized in Table 3.1. The siRNAs used are listed in Table 3.2. For manufacturers and production number of all reagents and chemicals used in the experiments, see Appendix A.

Note: LIN300 and LIN400 have similar characteristics and are shown to give the same transfection efficiencies in several cell lines (Jostein Malmo, unpublished results), and the name LIN350 is used for both these formulations, since we run out of LIN400 stock and had to use them interchangeably.

Table 3.1: Physical and chemical characteristics of the different chitosans used herein. Name of chitosans, DP_n, M_n, M_w, PDI, Chain Architecture, F_A and d.s. are provided.

Name	DP_n	M_n	M_w	PDI	Chain architecture	F_a	d.s.
	-	kDa	kDa	-	-		% 4AM
LIN250	247	49.5	100.3	2.03	Linear	<0.002	0
LIN300 (LIN350)	320	64.1	141.6	2.21	Linear	<0.002	0
LIN400 (LIN350)	375	75.1	203	2.70	Linear	<0.002	0
SB300	312	62.3	169	2.70	Self-branched	<0.002	0
F_a=0 (2% PEG)	365	-	-	-	Linear, PEGylated	<0.002	0
DP_{85} (4AM)	85	-	-	-	Linear, 4AM-substituted	<0.002	8

Legend: LIN: Linear, SB: Self-branched, F_a: Degree of acetylation, DP_n: Number-average Degree of Polymerization, M_n: Number average molecular weight, M_w: Weight average molecular weight, PDI: Polydispersity Index, PEG: Polyethylene glycol, d.s.: Degree of AAM-substitution, 4AM: GlcNAc-GlcNAc-GlcNAc-GlcNAc-2,5 anhydro-mannofuranose, kDa: 1,000 Daltons.

Table 3.2: Names and functions of the siRNAs used throughout the experiments. Full names are given in Appendix A.

siRNA name	Target/Function
Alexa 647	Non-targeting siRNA labeled with a fluorescent dye to detect nanoparticle uptake
Anti-Abcb1a	Targets *Abcb1a* mRNA
Anti-GAPDH	Targets GAPDH mRNA
Anti-Luciferase	Targets luciferase mRNA, but was used herein as a non-targeting negative control
Negative control	Has no known mRNA target and was used as a non-targeting negative control

3.2 RNAiMAX

Lipofectamine RNAiMAX was in some occasions included in the experiments as a positive control when measuring uptake and knockdown efficiencies. RNAiMAX is a liposome-based transfection agent and a well-established siRNA delivery system for *in vitro* experiments.

Solutions containing RNAiMAX and siRNA were prepared by following the procedure given by the manufacturer, dissolving siRNA and RNAiMAX in opti-MEM to a final concentration of 50 or 100 nM of siRNA (13.3 μL RNAiMAX reagent/μg siRNA). After the solutions were made, they were incubated at room temperature for 20 min before use. For an example of how the RNAiMAX nanoparticles were assembled, see Appendix B.

3.3 Cell culture

Note: Volumes and cell numbers for 75 cm^2 T-flasks are used in this protocol. For RBE4 cell culture with 25 cm^2 T-flasks, volumes and cell numbers were 1/3 of what described here.

C6 or RBE4 cells were thawed and incubated in 75 cm^2 or 25 cm^2 T-flasks (Nunc, T75-flasks, T25-flasks) containing Dulbecco's modified eagle medium (DMEM) or Minimal essential medium-alpha (α-MEM), respectively, supplemented with 10 % Fetal Bovine Serum (FBS) at 37 °C and 5 % CO_2. DMEM was supplemented with 1% non-essential amino acids (NEAA), while α-MEM was supplemented with basic fibroblast growth factor (bFGF, 1 ng/mL) and G418 selection antibiotic (300 μg/mL). α-MEM and Opti-MEM used for RBE4 experiments were always incubated at 37 °C, 5 % CO_2 overnight prior to use. After two days the growth medium was changed, and when the cells had grown confluent the culture was further passaged. Medium was removed, and the cells were washed with 13 mL warm PBS (37 °C), before 2 mL trypsin/EDTA (0.05 %, room temperature) was added. A volume of 1 mL was removed, and the flask was put in the incubator (37 °C, 5 %). After 3 min, the flask was taken out and shaken to detach all cells. Detachment was confirmed by light microscopy. A volume of 7 mL warm growth medium (37 °C) was added and after re-suspending a couple of times to remove cell clusters the solution was transferred to a 50 mL falcon tube (Corning). Fresh medium was added to a total volume of 10 mL before re-suspending again. A small volume was transferred to an eppendorf tube and prepared for cell counting, while the falcon tube was centrifuged at 1,500 rpm for 5 min. Cells were counted manually using a haemocytometer and a light microscope. After determining the cell density, the growth medium was carefully removed from the falcon tube and fresh medium was added to the calculated volume (e.g. 1 mL medium/million cells). A cell suspension of 1-2 million cells was transferred to a new T-75 flask, and fresh medium was added to a total volume of 15 mL. The new cell culture was then kept in the incubator at 37 °C, 5 % CO_2 until about 90-100% confluency was reached (about 3-4 days), before it was split again.

To induce expression of P-gp, C6 cells were cultivated for approximately five weeks with DMEM supplemented with doxorubicin (1 ng/mL).

3.4 Collagen coating

All well plates and flasks that were used for cultivating the RBE4 cells were coated with type I collagen. Acetic acid was first diluted from a 5 M stock solution to 20 µM in DNase and RNase free Molecular biology grade water (MBG water), and the solution was sterile filtrated using a syringe and a 0.22 µm filter (Millipore). Rat-tail type I collagen stock solution (8.58 mg/mL) was then diluted in the acetic acid to 50 µg/mL. The collagen solution was added to 96-well plates (Corning, 65 µL/well) and T-25 flasks (1.5 mL), and incubated at room temperature for 2 h. Excess solution was removed, and the well plates and flasks were washed with a double volume of PBS, sealed with parafilm (plates), and stored in the fridge (4 °C) until use. Prior to seeding with cells, the containers were again washed with PBS.

3.5 Transfection

Cells were seeded in 96-well plates by adding 100 µL cell suspension (usually with 5,000, 7,500 or 15,000 cells/well) and incubated for 24 h. The growth media used for transfection experiments were supplemented with Penicillin and Streptomycin (PEST, 100 U/mL). When preparing the nanoparticles siRNA stock solution (50 µM) was diluted in the required amount of water, before chitosan (0.1 mg/mL) was added during vortex mixing (1,200 rpm) for about 10 seconds. The solutions were then incubated for 30 min in room temperature, to make sure the nanoparticles were properly assembled before use. For the nanoparticle formulations with hyaluronic acid (HA, 50 kDa, 1mg/mL), HA was added after the first incubation to a 3:1 charge ratio against the chitosan amino groups, and incubated for 1 h.

While the nanoparticles were assembling, the growth medium was removed from the cells and 200 µL HBSS (37° C) was added. After incubating properly, the nanoparticles were diluted with an equal volume of hypertonic opti-MEM (Opti-MEM supplemented with 20 mM HEPES and 270 mM mannitol), HBSS was removed from the cells, and 50 µL of nanoparticle solution was added to each well. The cells were then put in the incubator for 5 h (4 h if measuring uptake) before the solution was removed and 200 µL fresh growth medium was added to each well. The medium was changed after 24 h and measurements were typically carried out either 48 or 72 h after transfection (5 h when measuring uptake of Alexa 647). Cell densities in the different experiments are presented in Table 3.3. siRNA dosages were typically 33.3 or 66.67 ng/well (50 or 100 nM). N/P ratios were always 10, 30 or 60. Samples containing non-transfected cells (treated with MBG water instead of nanoparticles)

were always included as an untreated control, and sometimes samples treated with naked siRNA were included.

For calculations and examples on how the chitosan-siRNA nanoparticle were assembled, see Appendix B.

Table 3.3: Cell-seeding densities used in the different experiments. The densities shown are the number of cells seeded out 24 h prior to transfection.

Cell line	Experiment	Application	Plate	Cell density (cells/well)
C6/RBE4	Alexa 647 Uptake	Flow cytometer	96 well	15,000
	R123 efflux assay	Flow cytometer	96 well	7,500
	KDalert	Spectrophotometer	96 well	5,000

3.6 Uptake

C6 or RBE4 cells were seeded in 96-well plates and transfected with nanoparticles using fluorescent Alexa 647 siRNA. After 4 h, growth medium was added to the wells to incubate for 30 min to allow for internalization of possible cell surface bound nanoparticles. The medium was then removed and replaced with 200 μL medium containing heparin (1 mg/mL) to incubate another 30 min to dissociate siRNA from possible remaining nanoparticles on the cell surface. The cells were washed two times with 200 μL PBS (37° C), before adding 25 μL trypsin/EDTA (room temperature), and put in the incubator for 5 min. To make sure all cells were detached, the well plate was hit gently a couple of times on the side walls, before checking in a light microscope. A volume of 150 μL ice-cold PBS containing 5 % FBS was added to each well, and then re-suspended 5 times, before the cells solutions were transferred to flow-cytometry tubes (BD Biosciences) and put on ice. The samples were then analyzed using a Gallios flow cytometer (Beckman Coulter, Inc.). The Alexa 647 was excited using a 633 nm laser line and emitted light was collected at FL6 using a 660/20 nm band pass filter to estimate the levels of intracellular Alexa 647 conjugated siRNA. To determine a threshold value for auto-fluorescence, a sample with untreated cells was measured first.

The Kaluza analysis software (Version 1.1, Beckman Coulter) was used to interpret and process the data obtained from all flow cytometry experiments. Microsoft Excel 2010 was used for graphical presentation of all results.

Uptake Kinetics experiment: A kinetics experiment with transfections using fluorescent Alexa 647 siRNA was carried out to measure intracellular levels of siRNA over time. The standard uptake protocol was followed but instead of only measuring uptake 4 h after transfection, measurements were carried out after 4, 24, 48, 72 and 96 h.

3.7 Rhodamine 123 (R123) Efflux Assay

C6 or RBE4 cells were seeded in 96-well plates and transfected with nanoparticles using anti-Abcb1a or negative control siRNA. At 48 h (or 72 h) after transfection, a working solution of Rhodamine 123 (R123) was made by diluting a stock solution of R123 (10 mg/mL) in opti-MEM to a concentration of 10 μM.
The growth medium was removed from the cells before being washed with 200 μL PBS (37 °C) and added 100 μL of the 10 μM R123 solution. The well plate was covered with aluminum foil and put in the incubator for 45 min. Afterwards, the cells were washed with 200 μL PBS (37 °C) before adding 200 μL growth medium and incubating for 2 h. Finally, the cells were washed with 200 μL PBS and prepared for flow cytometry as described earlier.

R123 Kinetics experiment: RBE4 cells were transfected with anti-Abcb1a or negative control siRNA and measured for intracellular R123 levels over six days using flow cytometry. The cells were transfected one, two or three days in a row (repeated transfection). Flow cytometry was carried out on day 1, 2, 3, 4, 5 and 7 after the first transfection.

The R123 was excited using a 488 nm laser line and emitted light was collected at FL1 using a 525/40 nm band pass filter to estimate the intracellular levels of R123 fluorescence.

3.8 KDalert GAPDH Assay

C6 or RBE4 cells were seeded in 96-well plates and transfected as previously described using anti-GAPDH or negative control siRNA. At 48 h after transfection, a KDalert Master Mix was prepared according to the manufacturers protocol (Ambion KDalert GAPDH Assay Kit).
The Master Mix was vortexed at 1,200 rpm and kept on ice until use. The medium was removed from the cells, and 150 μL KDalert lysis buffer was added to each well before covering the well plate with parafilm and storing it in the refrigerator (4°C) for 20 min. The cell lysate was then resuspended before transferring 10 μL from each well to a 1/2 area well plate (Corning). Wells with 10 μL MBG water served as a reference for determining GAPDH activity. A volume of 90 μL Master Mix was then added to each well, and after 15 min the absorbance was measured at 615 nm using a spectrophotometer (Spectramax plus, Molecular devices).

3.9 P-gp inhibition by verapamil

C6 or RBE4 cells were transfected with anti-Abcb1a or negative control siRNA as previously described. A 10 μM working solution of the P-gp inhibitor verapamil was made by diluting the stock solution (10 mg/mL) in opti-MEM.

The growth medium was removed and 50 μL verapamil was added to some of the untreated cells as a positive control. The rest of the wells were added 50 μL opti-MEM. The cells were incubated for 45 min. A 50 μL R123 solution (10 μM) was then added to all wells (without removing the original 50 μL) and the cells were analyzed for R123 efflux as previously described, except that the verapamil-treated cells were added growth medium containing 5 μM verapamil instead of regular growth medium.

3.10 Transmission electron microscopy

RBE4 cells were transfected with chitosan-gold-siRNA nanoparticles and prepared for transmission electron microscopy (TEM and scanning TEM (STEM)). The gold particles were a gift from Wilhelm R. Glomm (Dept. of Chemical Engineering, NTNU) and had a size of 30 nm. To make chitosan-gold siRNA nanoparticles, the transfection protocol was used, except that anti-Luciferase siRNA (used as non-targeting siRNA) and gold particles were mixed in MBG water before adding the chitosan. A stock solution of gold ($1 \cdot 10^{11}$ particles/mL) was diluted in MBG water to a concentration of $2.5 \cdot 10^8$ particles/mL. The siRNA concentration was 100 nM, and N/P 30 was used.

To investigate nanoparticle uptake in RBE4 cells by TEM, cells were grown in T25-flasks until they reached confluency, transfected with nanoparticle solution (4.3 mL) and incubated as usual (37 °C, 5 % CO_2, 5 h) before growth medium was added. Cells treated with either gold solution or MBG water were included as controls. 16 h after transfection, the cells were prepared for TEM.

Preparation of the cells for TEM was carried out by senior engineer Linh Hoang (Dept. of Laboratory Medicine, Children's and Women´s Health, NTNU). In short, the cells were fixated (2 % GA in 0.1 M Hepes), encapsulated in gelatin, dehydrated with ethanol, infiltrated in epoxy and sectioned to 70 nm slices using a diamond knife (Diatome) before placing them on copper grids (200 mesh, 3 mm).

Pure chitosan-gold-siRNA nanoparticle solutions were also prepared for TEM and STEM analysis, to determine their shape, size and atomic content. A 2 μL pure gold-nanoparticle solution was placed on a copper grid 4 h after assembly of the complexes, and dried overnight before use.

TEM/STEM analysis was performed using the Tecnai 12 transmission electron microscope (FEI) with a voltage of 80 kV (TEM) or 120 kV (STEM). Pictures were taken using an integrated camera (Morada).

TEM pictures were obtained and processed using the iTEM software. STEM pictures were obtained and processed using TEM imaging and analysis (TIA).

3.11 Reverse Transcriptase (RT) PCR

In order to identify the expression of the *Abcb1a* gene in C6 cells, a real-time reverse transcriptase polymerase chain reaction (RT-PCR) was carried out using the ABI 7500 system (Applied Biosystems). mRNA was harvested and cDNA synthesized using the Cells-to-C_T kit (Applied Biosystems) as described in the manufacturer's protocol using DNase to degrade the genomic DNA. cDNA synthesis was performed at 37 °C for 60 min. Quantitative Real-Time PCR was performed using the following cycle conditions: 95 °C for 10 min, 40 cycles at 95 °C for 15 s, and 60 °C for 1 min. SYBR Green I dye (Applied Biosystems) was used for detection of the PCR products. The PCR primers used are presented in Table 3.4. The primers were used at 250 nM and the efficiencies were determined using standard curves. In addition to identification of the *Abcb1a* gene, the housekeeper gene *ACTB* (encoding β-actin) was included as an internal control in the experiment.

Table 3.4: Primers used for RT-PCR to identify expression of the Abcb1a gene (encoding P-gp), including name of protein/gene, nucleic acid sequence and manufacturer. ACTB (encoding β-actin) identification served as internal control.

Protein (*gene name*)	Primer	Sequence (5′-3′)	Manufacturer
P-gp (*Abcb1a*)	Forward	AGCCCTGTTCTTGGACTG	Sigma
P-gp (*Abcb1a*)	Reverse	AGTTCTGATGGCTGCTAAGAC	Sigma
β-actin (*ACTB*)	Forward	TCCACCTTCCAGCAGATGTG	MWG Operon
β-actin (*ACTB*)	Reverse	GCATTTGCGGTGCACGAT	MWG Operon

4. Results

The overall goal of this thesis was to investigate siRNA-mediated knockdown of P-glycoprotein (P-gp) using chitosan-siRNA nanoparticles in the two rat brain derived cell lines C6 and RBE4 *in vitro*, to potentially increase drug delivery efficiency to brain cancer cells. The idea was to characterize the possibility for P-gp silencing in both these cell lines in order to possibly implement them in a future glioma-Blood-Brain Barrier (BBB) *in vitro* model by co-cultivation in a transwell system.

C6 rat glioma cells were investigated in regards to transfection efficiencies, with the main goal being to silence P-gp expression in this cancer cell line to possibly increase susceptibility of these cells toward chemotherapeutic treatment. Gliomas are tumors arisen from glial cells in the brain [79]. The C6 cell line originates from astrocytes; specialized glial cells that interact with the endothelial cells in the BBB and help induce and maintain tight junction formation in these cells [71, 81]. To successfully deliver drugs to brain targets such as glioma cells, the drugs must first penetrate the BBB, but this is often prevented by P-gp efflux of the drugs by the BBB endothelial cells [74, 75]. Therefore, Rat Brain Endothelial Cells (RBE4) were used as an *in vitro* model of the BBB to investigate how to efficiently silence P-gp expression in these cells, to hopefully improve drug flow across the BBB for future experiments.

Furthermore, the uptake mechanisms and intracellular trafficking pathways utilized by different chitosan-siRNA nanoparticles in RBE4 cells were investigated using transmission electron microscopy (TEM). This was performed in order to evaluate the differences in transfection efficiencies by nanoparticles developed for systemic delivery for future *in vivo* P-gp silencing studies, and for investigating the intracellular trafficking pathways utilized by the different nanoparticles.

Chitosans of different number-average degree of polymerization (DP_n) and either linear (LIN) or self-branched (SB) chain architecture were used in most experiments (LIN350, SB300). Some other chitosans formulations, such as LIN250, in addition to previously developed formulations with improved colloidal stability; F_a=0 (2% PEG), DP_{85} (4AM) as well as chitosans coated with hyaluronic acid (HA), were screened to test their effectiveness as vectors for siRNA. All experiments were carried out using three or four parallels for every sample, and thus the data presented are mean values of these parallels, +/- one standard deviation.

Note: The term nanoparticle is used for both chitosan- and RNAiMAX-based formulations. The abbreviation T (targeting siRNA) is used in all figures for anti-Abcb1a or anti-GAPDH siRNA. Negative control siRNA is abbreviated NT (non-targeting) in all figures.

For different examples of flow cytometer overlay plots, see Appendix C. The raw data from all experiments (Uptake, R123 efflux, KDalert GAPDH assay, RT-PCR) are presented in Appendix D. The RT-PCR amplification curves are shown in Appendix E.

4.1. Chitosan-based siRNA delivery in C6 cells

4.1.1 Uptake of Alexa 647 siRNA

C6 cells were transfected with chitosan-siRNA nanoparticles to measure the uptake efficiencies in this cell line. Nanoparticles with LIN350 or SB300 and Alexa 647 siRNA at 50 nM and N/P 10, 30 and 60 were prepared, and intracellular levels of Alexa 647 siRNA were measured. As shown in Figure 4.1A, the highest uptake was observed at N/P 30 for both chitosans, with N/P 10 being least efficient. The uptake experiment was repeated two times with consistent results, and since N/P 30 provided the highest uptake, this formulation was used for further experiments.

As shown in Figure 4.1B, the uptake of nanoparticles with either LIN350 or SB300 at N/P 30 was compared to RNAiMAX at 50 or 100 nM. The cells transfected with RNAiMAX had notably higher uptake of Alexa 647 siRNA than the cells transfected with the chitosans. The naked siRNA was not internalized by the cells.
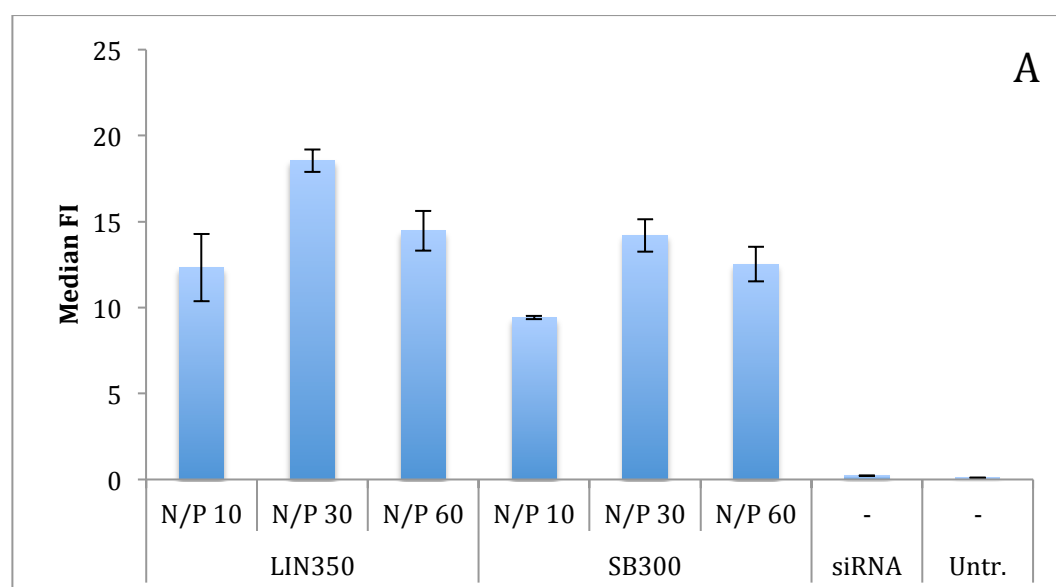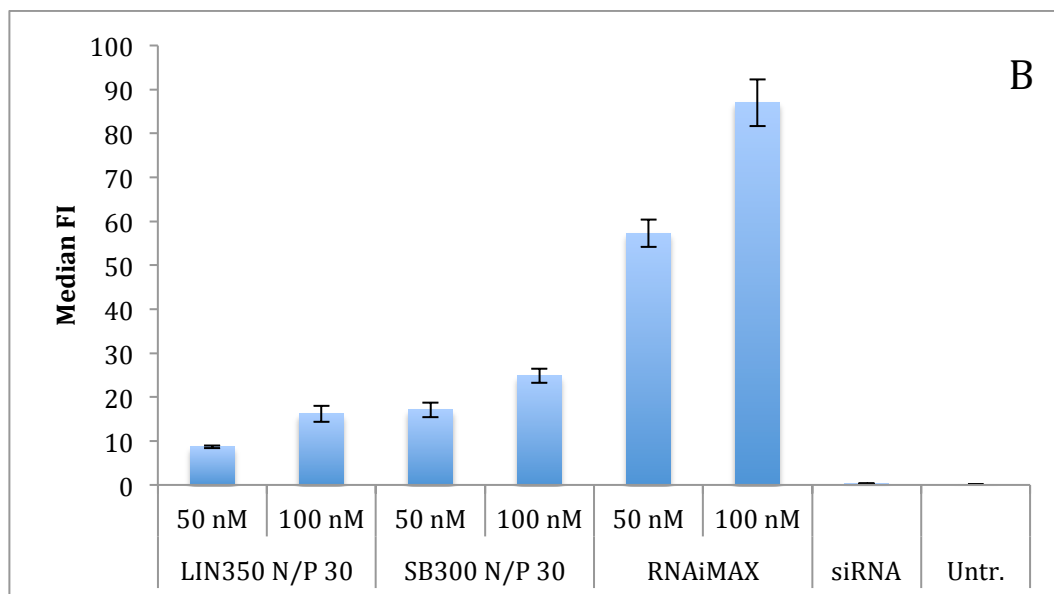
Figure 4.1: Intracellular levels of Alexa 647 siRNA in C6 cells after 5 h given by the median FI measured for different nanoparticles, with cells either untreated (Untr.) or treated with naked Alexa 647 siRNA (siRNA) as controls. ***A:*** *LIN350 and SB300 along with Alexa 647 siRNA at 50 nM and N/P 10, 30 and 60.* ***B:*** *LIN350, SB300 and RNAiMAX along with Alexa 647 siRNA at 50 or 100 nM and (for the chitosan formulations) N/P 30.*

4.1.2 Knockdown of GAPDH

The KDalert GAPDH Assay is often used for optimization of siRNA knockdown experiments. The *GAPDH* gene is a housekeeping gene that is usually expressed by all cells in a culture at constant levels, encoding the protein Glyceraldehyde-3-phosphate dehydrogenase (GAPDH). To test the efficiency of the chitosan-siRNA nanoparticles on GAPDH knockdown in the C6 cell line, the cells were transfected with LIN350, SB300 or RNAiMAX along with anti-GAPDH or negative control siRNA at 50 or 100 nM and N/P 30. As seen in Figure 4.2, all formulations gave reduced levels of GAPDH protein activity. LIN350 (100 nM) and SB300 (at both concentrations) had somewhat low GAPDH levels for their negative control siRNA-treated cells, especially SB300 100 nM which had 45% GAPDH of the untreated cells, indicating toxic effects.
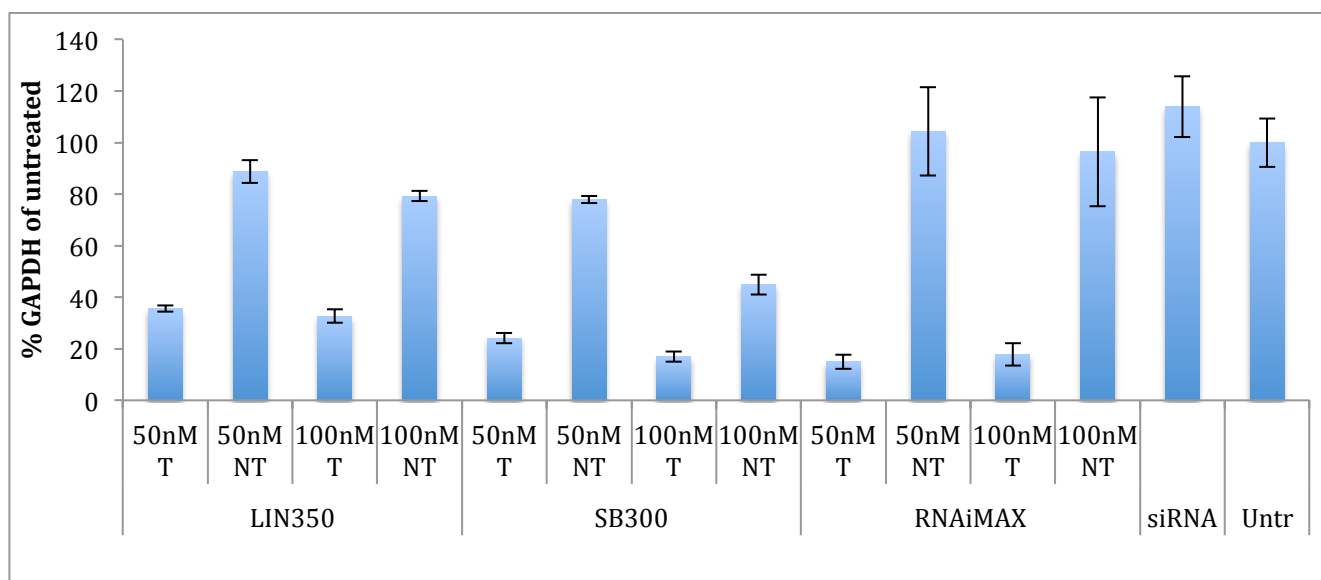
Figure 4.2: Percentages GAPDH of the untreated control after 48 h in C6 cells, transfected with nanoparticles with LIN350 or SB300 at N/P 30 or RNAiMAX, with either anti-GAPDH (T) or negative control (NT) siRNA at 50 or 100 nM. Untreated cells (Untr.) and cells treated with naked anti-GAPDH siRNA (siRNA) were included as controls.

4.1.3 Knockdown of P-glycoprotein expression

Since the GAPDH knockdown experiment gave positive results, it was attempted to knock down P-glycoprotein (P-gp) expression in C6 cells by targeting the *Abcb1a* mRNA. C6 cells from passage number 4 (px 4, about 2-3 weeks after the cells were thawed) were transfected with LIN350 or SB300 along with anti-Abcb1a or negative control siRNA at 50 nM and N/P 30 to test the efficiency of *Abcb1a* mRNA knockdown, using the Rhodamine123 (R123) efflux assay. The results are presented in Figure 4.3, and show high levels of the P-gp substrate R123 in all samples, including the untreated cells. The consistently high R123 levels in all the samples indicate that the cells were not expressing P-gp in significant amount at this time.
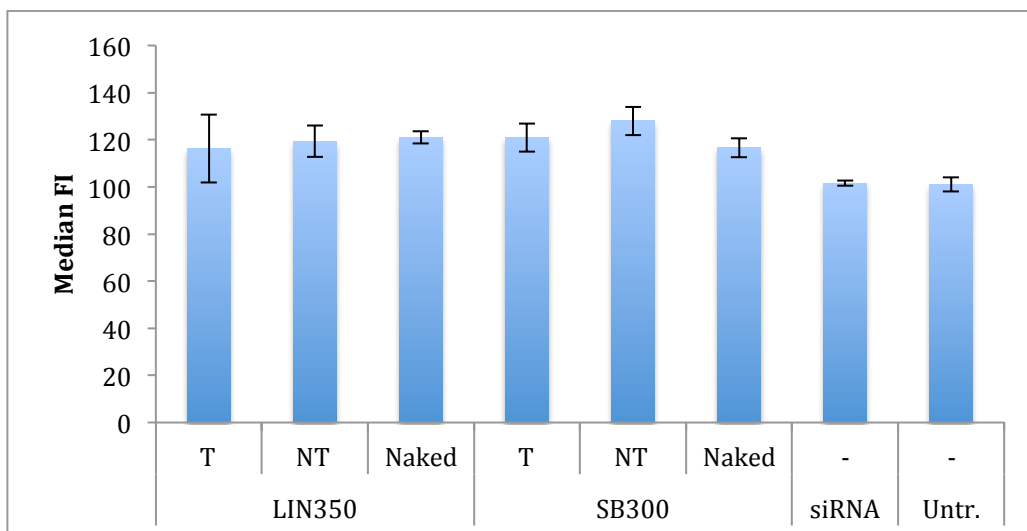
Figure 4.3: Intracellular levels of R123 in C6 cells after 5 h, given by the median FI. The cells were transfected with LIN350 or SB300, containing either anti-Abcb1a or negative control (NT) siRNA at 50 nM and N/P 30. Naked chitosans (Naked), naked siRNA (siRNA) and untreated cells (Untr.) were included as controls.

Since the C6 cells did not show any signs of P-gp expression from the R123 efflux assay, but have been reported previously to be P-gp positive [91], some of the C6 cells were cultured in growth medium containing the P-gp substrate doxorubicin (1 ng/mL) for about five weeks to induce expression of P-gp. An R123 efflux assay was performed when the cells were around px 15, comparing untreated and doxorubicin-treated cells without transfecting the cells with nanoparticles, as presented in Figure 4.4. Both samples had cells with very low intracellular levels of R123 compared to the first experiment (Figure 4.3) at identical experimental conditions, indicating that the C6 cells had started to express P-gp. There were minimal differences in R123 levels between the two samples, suggesting that the C6 P-gp expression increased over time, independent of the doxorubicin treatment.
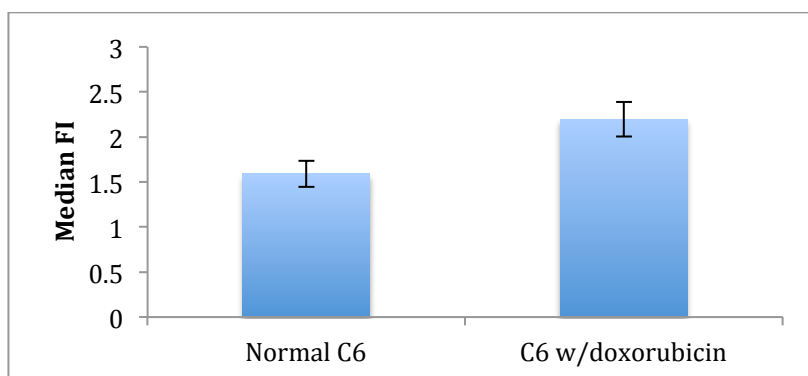
Figure 4.4: Intracellular levels of R123, given by the median FI, in C6 cells that were either untreated or cultured with doxorubicin-containing growth medium (1 ng/mL) for about five weeks.

Another R123 efflux assay was carried out about two months after thawing the cells, at px 19. The cells were transfected with nanoparticles containing LIN350, SB300 or

RNAiMAX and anti-Abcb1a or negative control siRNA at 100 nM and N/P 30, and cells treated with the P-gp inhibitor Verapamil were included as a positive control. Figure 4.5 shows the results from this experiment. In accordance with the previous experiment (Figure 4.4), the median FI values were much lower in this R123 experiment compared to the initial, even though increasing siRNA concentration and flow cytometer voltage; further confirming that the C6 cells had started to express P-gp. The cells treated with anti-Abcb1a siRNA had a higher median FI value than the untreated or negative control siRNA-treated cells, showing a potential P-gp knockdown effect from the anti-Abcb1a siRNA (Figure 4.5A). The verapamil treated cells had notably higher FI values, indicating an efficient inhibition of P-gp (Fig 4.5B).

R123 efflux was also measured after 72 h (not shown) giving similar values to 48 h.
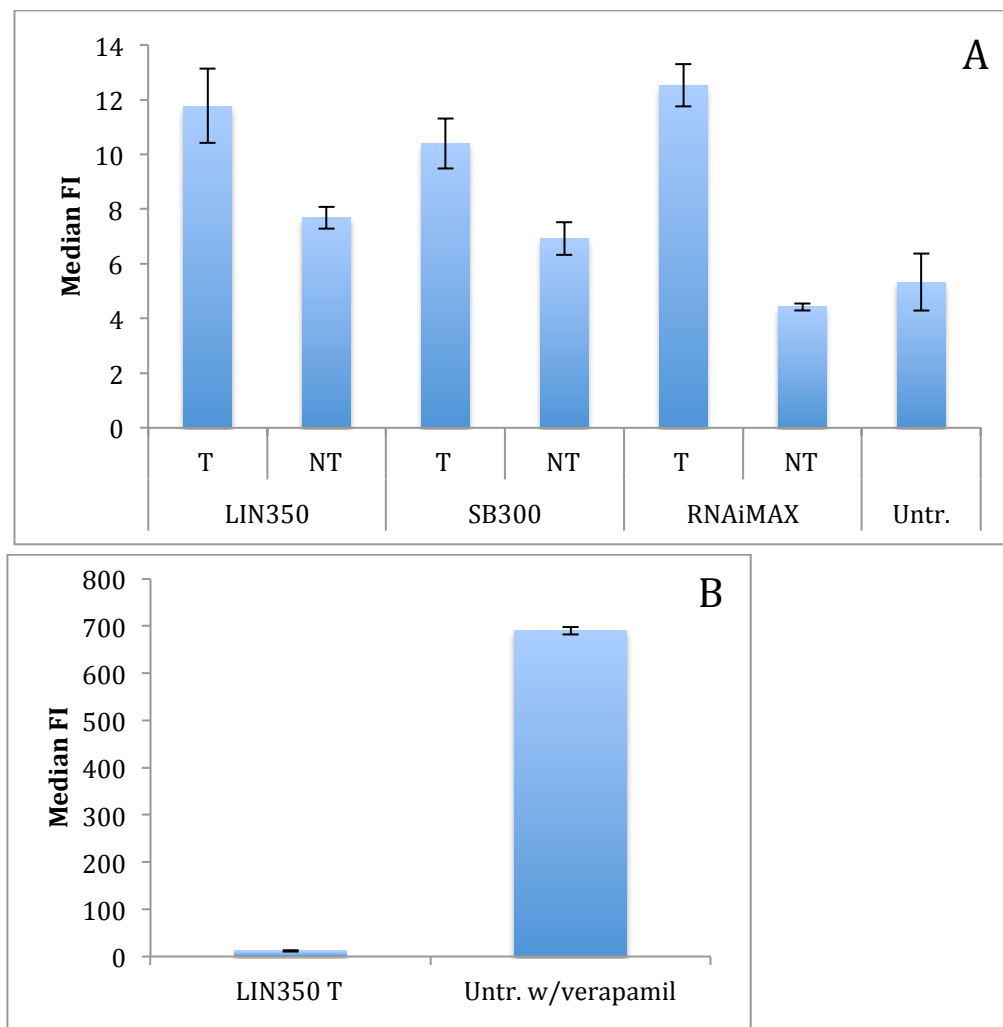
*Figure 4.5: Intracellular R123 levels in C6 cells after 48 h, given by the median FI, after transfection with nanoparticles containing either anti-Abcb1a (T) or negative control (NT) siRNA at 100 nM at N/P 30. As controls, untreated cells (Untr.) with or without verapamil were included. **A:** LIN350, SB300 and RNAiMAX. **B:** A comparison between LIN350 with anti-Abcb1a siRNA and a verapamil-treated sample of cells.*

4.1.4 Reverse Transcriptase-PCR of *Abcb1a* mRNA

To confirm the expression of P-gp, two Reverse Transcriptase-PCR (RT-PCR) experiments were carried out, using C6 cells from px 4 and 19. The results are presented in Figure 4.6; comparing mRNA levels of *Abcb1a* between the two C6 passages and the RBE4 cell line (RBE4 data were borrowed with permission from Ph.D. candidate Jostein Malmo). The results show that the C6 cells from px 19 and RBE4 cells were *Abcb1a* positive, while C6 cells from px 4 did not contain any *Abcb1a* mRNA. RBE4 mRNA levels were set to 100 %, and the mRNA levels in the C6 samples are relative to this value. C6 cells (px. 19) had about 25% *Abcb1a* mRNA of the RBE4 levels, and for C6 (px. 4) *Abcb1a* mRNA was not detected. The mRNA amplification curves of *Abcb1a* and the internal control ATCB (encoding β-actin), including calculations of the relative mRNA levels, are given in Appendix D and E.

Figure 4.6: A comparison of RT-PCR results for Abcb1a mRNA from C6 (px 4 and 19) and RBE4 cells. Percentages are given in relationship to RBE4 Abcb1a mRNA levels, which were set to 100% in order to see the relative amount of Abcb1a mRNA in C6 cells compared to this cell line.

4.2 Chitosan-based siRNA delivery in RBE4 cells

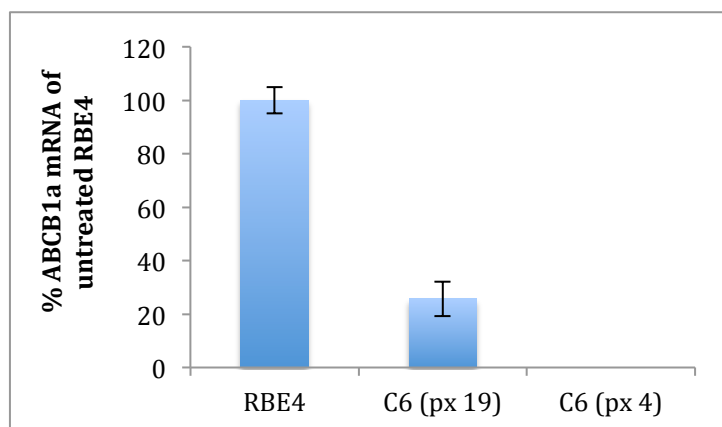The RBE4 cell line was investigated with regards to transfection efficiencies to possibly implement this cell line as endothelial cells in an *in vitro* glioma-BBB model with C6 cells.

Further, since chitosan-based siRNA delivery *in vivo* is often limited by the clearance of the nanoparticles in the blood, it is of interest to develop chitosans that can form serum-stable nanoparticles with siRNA, with increased circulation time and colloidal stability (resistance to aggregation). For a nanoparticle to reach for example the BBB, it must be administered systemically and travel through the blood system, where it might be recognized by immune cells for subsequent phagocytosis and degradation [48]. It is also possible that the nanoparticles themselves can form inter-particular aggregates due to reduced charge repulsions at physiological pH, which reduces the chances of the nanoparticles to reach their target [96]. Furthermore, if the siRNA molecules are exposed to the environment, they are rapidly degraded by endogenous RNases (44). The RBE4 cell line was used for the screening of chitosans previously developed for this purpose, to test their *in vitro* transfection efficiencies.

Since it was found that none of the novel formulations provided efficient RNA interference (RNAi), transmission electron microscopy (TEM) experiments were ultimately carried out to investigate the intracellular fate of these nanoparticles.

4.2.1.1 Uptake of Alexa 647 siRNA

Several chitosan formulations with colloidal stability were screened to test their transfection efficiencies in RBE4 cells. To measure siRNA uptake, LIN250, LIN250 w/HA, LIN350, LIN350 w/HA, DP_{85} (4AM) and F_a=0 (2% PEG) were assembled into nanoparticles using Alexa 647 siRNA at 50 nM and N/P 10 or 30.
As seen in Figure 4.7, DP_{85} (4AM) at N/P 30 and F_a=0 (2% PEG) at both N/P ratios showed the highest uptake of Alexa 647 siRNA; about 1.5 times higher median FI values than for LIN250 and LIN350 were observed. LIN250 w/HA, LIN350 w/HA and DP_{85} (4AM) at N/P 10 showed lower levels of uptake compared to the other chitosans in the experiment.
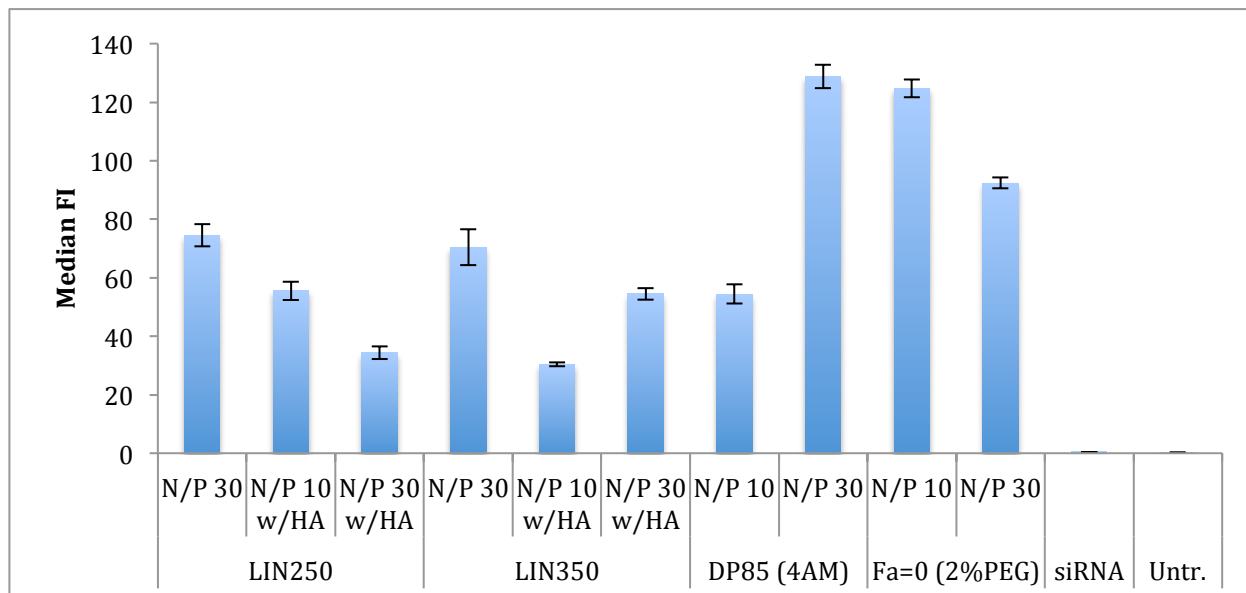
Figure 4.7: Intracellular levels of Alexa 647 after 5 h, given by the median FI, using Alexa 647 siRNA at 50 nM, and LIN250, LIN250 w/HA, LIN350, LIN350 w/HA, DP₈₅ (4AM) and Fₐ=0 (2% PEG) chitosans at N/P 10 or 30. Untreated cells (Untr.) and cells treated with naked Alexa 647 siRNA (siRNA) were included as controls.

4.2.1.2 Uptake kinetics

Since RNAi is dependent on siRNAs, it is of interest to investigate how long the siRNA molecules will be present intracellularly. It was attempted to find this out by using linear and self-branched chitosan to see if there were any differences in the siRNA loss rate regarding chitosan chain architecture.

A kinetics experiment was carried out, using fluorescent Alexa 647 siRNA at 100 nM and either LIN350 or SB300, at N/P 30. The results are shown in Figure 4.8. SB300 mediated a slightly higher uptake of Alexa 647 siRNA than LIN350, but the same loss rate pattern was observed for both samples. After 48 h there were low levels of siRNA present in the LIN350- or SB300-treated cells, indicating a rapid cellular loss of the fluorescent Alexa 647 siRNA.
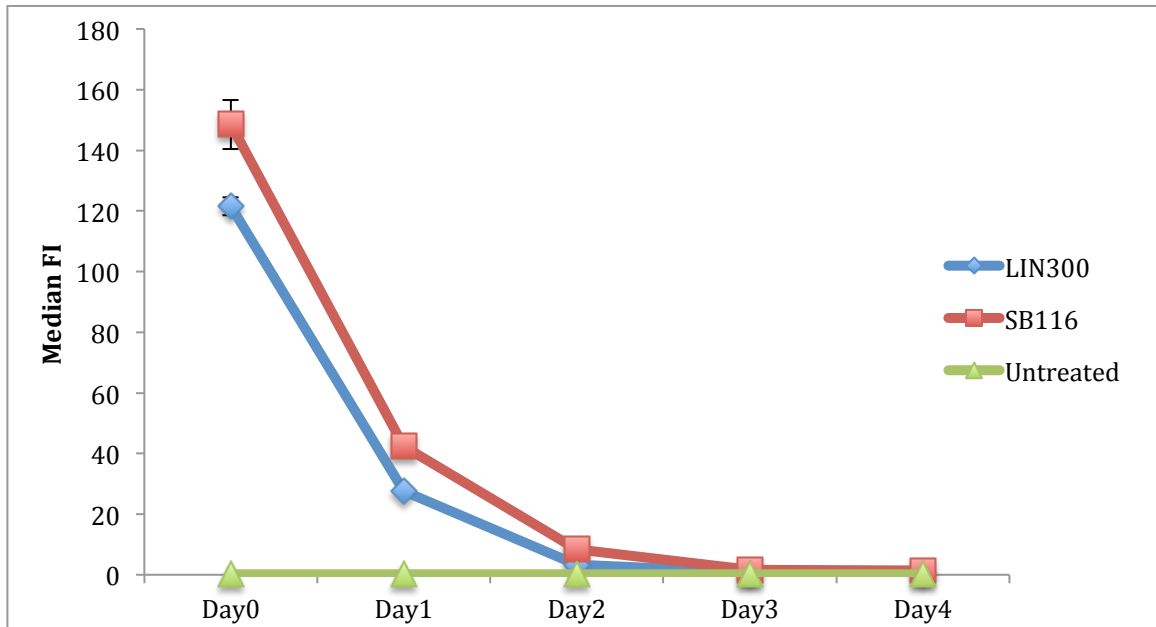
Figure 4.8: Intracellular levels of Alexa 647 siRNA at 100 nM, using either LIN350 or SB300 chitosans at N/P 30, given by the median FI. Uptake of the nanoparticles was measured at 5, 24, 48, 72 and 96 h after transfection (day 0, 1, 2, 3 and 4). The blue line shows LIN350, the red line shows SB300 and the green line shows untreated cells.

4.2.2 Knockdown of GAPDH

A KDalert GAPDH assay was carried out to measure the knockdown-effect on GAPDH protein activity. RBE4 cells were transfected with LIN250, LIN250 w/HA, LIN350, LIN350 w/HA, DP$_{85}$ (4AM) and F$_a$=0 (2% PEG), along with anti-GAPDH siRNA or negative control siRNA at 50 nM and N/P 10 and 30. The results are shown in Figure 4.9. LIN250 and LIN350 provided efficient reductions in GAPDH protein activity without toxicity, while the other formulations had no effect.
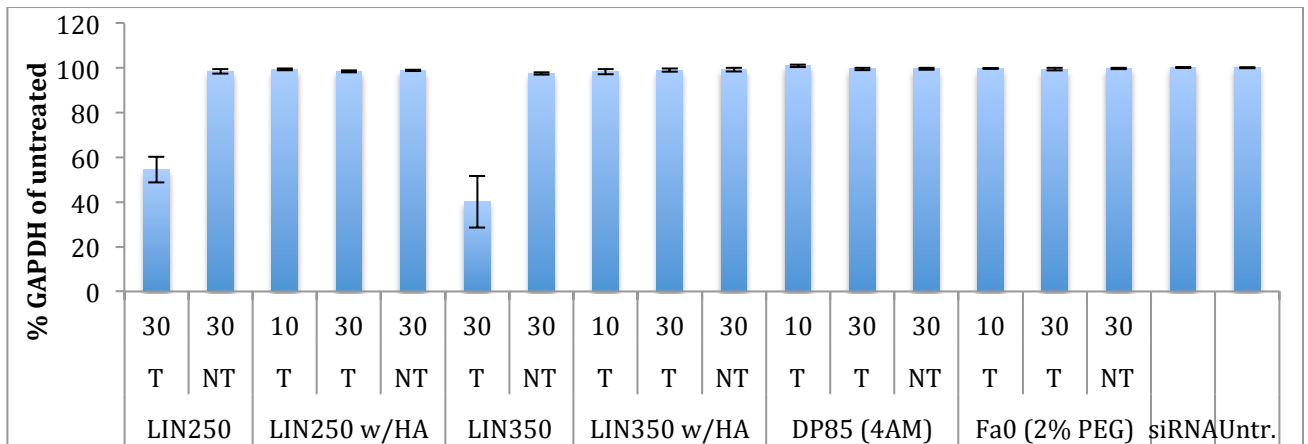
Figure 4.9: Percentages of GAPDH protein activity after 48 h compared to the untreated control, using nanoparticles containing anti-GAPDH (T) or negative control (NT) siRNA at 100 nM and LIN250, LIN250 w/HA, LIN350, LIN350 w/HA, DP$_{85}$ (4AM) or F$_a$=0 (2% PEG) chitosans. N/P ratios of 10 and 30 were used. Untreated cells (Untr.) and cells treated with naked anti-GAPDH siRNA (siRNA) were included as controls.

Currently the main problem associated with *in vitro* BBB models is that the tight junctions between the endothelial cells are not tight enough, thus substances can penetrate the BBB cell layer via paracellular transport [71]. This can be improved by co-culturing RBE4 and astrocyte-derived cells such as C6 cells, since astrocytes are shown to maintain tight junction properties in the BBB *in vivo* both in terms of structural association and provision of growth factors. An implementation of the RBE4 and C6 cells into a transwell *in vitro* glioma-BBB model would require the transfection of confluent RBE4 cells representing the densely layered endothelia. Consequently, to test if a confluent cell layer would affect the knockdown efficiency of the nanoparticles in RBE4 cells, 30,000 cells were seeded in each well (instead of the usual 7,500) and a KDalert assay was used to measure levels of GAPDH protein activity. RBE4 cells were transfected with LIN350 (N/P 10, 30 and 60) or RNAiMAX with anti-GAPDH or negative control siRNA at 50 or 100 nM concentrations. The results are shown in Figure 4.10. LIN350 mediated efficient reductions of GAPDH protein activity, except at N/P 10, 50 nM. LIN350 (at N/P 60, 50 nM and N/P 30 and 60, 100 nM) showed the most promising knockdown effects, giving reduced GAPDH protein activity at similar levels to the RNAiMAX transfected cells. The results show that the nanoparticles were able to efficiently transfect even confluent cells with a reduction in GAPDH protein activity comparable to the non-confluent cells (Figure 4.9, LIN350 T).
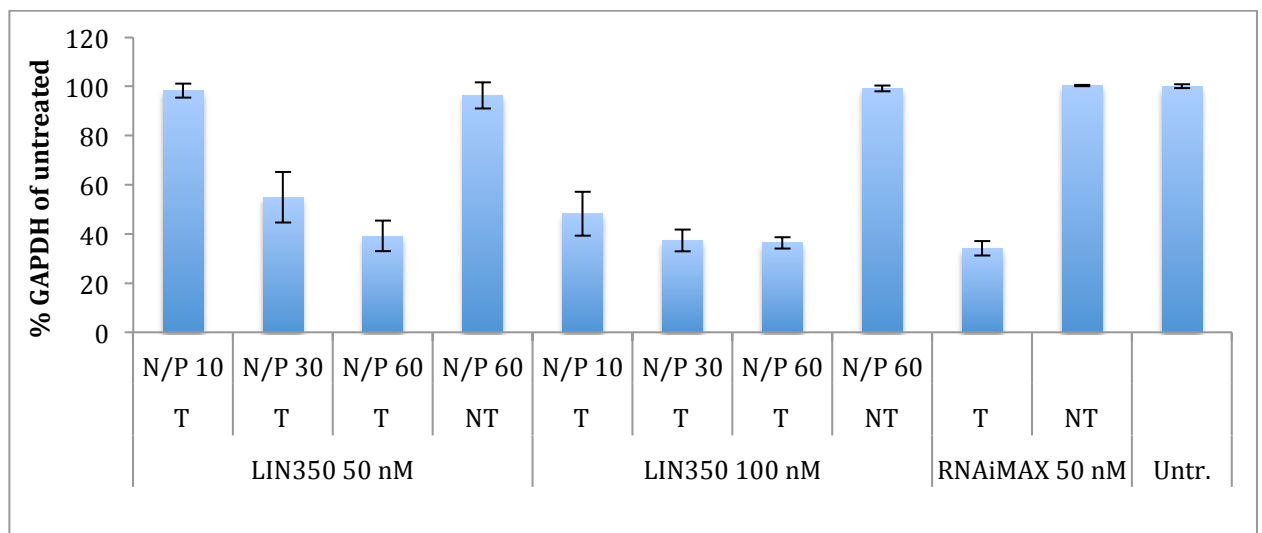

Figure 4.10: Percentages of GAPDH protein activity after 48 h compared to the untreated control, using LIN350 or RNAiMAX along with anti-GAPDH (T) or negative control (NT) siRNA at 50 or 100 nM and N/P 10, 30 and 60. Untreated cells (Untr.) were included as a control.

4.2.3 Knockdown of P-glycoprotein with chitosans with colloidal stability

From the results presented in Figures 4.7 and 4.9 it is clear that some of the modified chitosans (particularly F_a=0 (2% PEG) and DP_{85} (4AM)) provided high levels of uptake but did not give a reduction in GAPDH protein activity in RBE4 cells. It was therefore hypothesized that nanoparticles with these chitosans are too stable and need more time to release the siRNA intracellularly to facilitate mRNA degradation. LIN350 and SB300 were included in the experiment to test if there were any differences between linear and self-branched chitosan chain architectures regarding the kinetics of the P-gp knockdown.

An R123 efflux assay was carried out; measuring intracellular levels of R123 after 48 and 96 h. Anti-Abcb1a or negative control siRNA were used along with different chitosans (LIN350, LIN350 w/HA, SB300, F_a=0 (2% PEG) and DP_{85} (4AM)) to form nanoparticles. N/P 30 and a siRNA concentration of 100 nM were used for all formulations. The results are presented in Figure 4.11. The novel nanoparticles with improved colloidal stability (LIN350 w/HA, F_a=0 (2% PEG) or DP_{85} (4AM)) mediated minimal reductions in P-gp efflux. LIN350 mediated efficient knockdown after 48 h but this effect dropped sharply when measured again after 96 h. SB300 mediated lower knockdown than LIN350 at 48 h but showed minimal difference in median FI values when comparing 48 and 96 h.

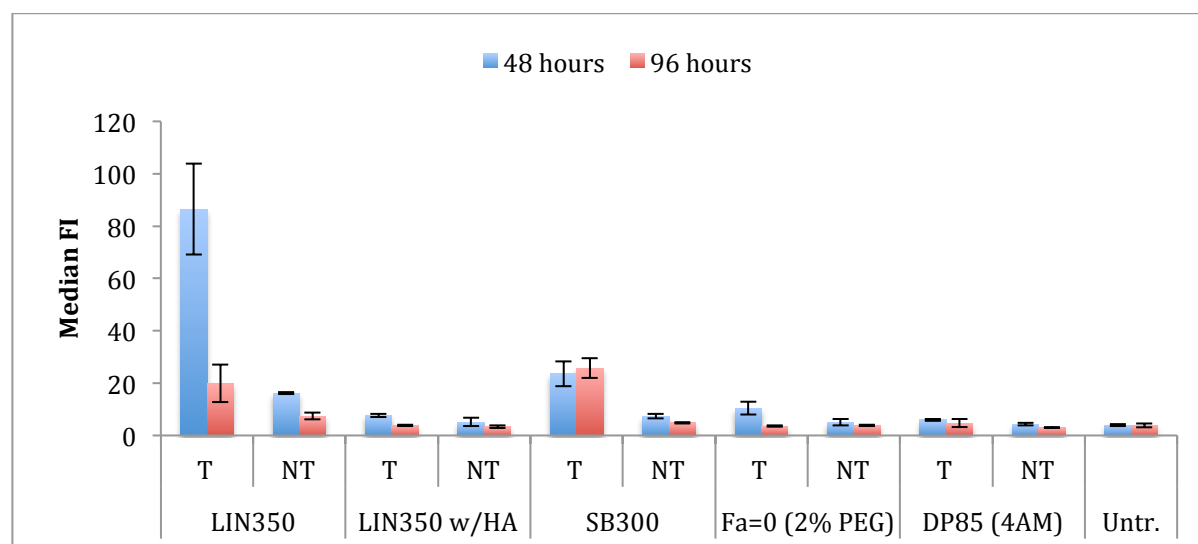*Figure 4.11: Intracellular levels of R123 in RBE4 cells given by the median FI, using nanoparticles consisting of LIN350, LIN350 w/HA, SB300, F_a=0 (2% PEG) or DP_{85} (4AM), along with anti-Abcb1a (T) or negative control (NT) siRNA at 100 nM and at N/P 30. R123 levels were measured after 48 h (blue columns) and 96 h (red columns). Untreated cells (Untr.) were included as a control for fully functional P-gp.*

4.2.4 P-gp knockdown kinetics

To investigate the kinetics of the P-gp knockdown in the RBE4 cells, an R123 efflux assay experiment was carried out over seven days. Nanoparticles with LIN350 and either anti-Abcb1a or negative control siRNA at 100 nM, N/P 30 were prepared to transfect the cells one (T1, NT1), two (T2, NT2) or three (T3, NT3) times with a 24 h interval (repeated transfection). R123 levels were measured at 24, 44, 72, 96, 120 and 168 h after the first transfection (day 1, 2, 3, 4, 5 and 7, respectively). The results are presented in Figure 4.12. Intracellular levels of R123 were highest after three days for all samples, with the cells transfected three times (T3) showing slower R123 efflux over time compared to the cells transfected only one or two times. At day 4 and 5, respectively, T1 and T2 treated cells had R123 levels close to those of the untreated control. After 44 h (day 2) there was minimal P-gp silencing for all samples.
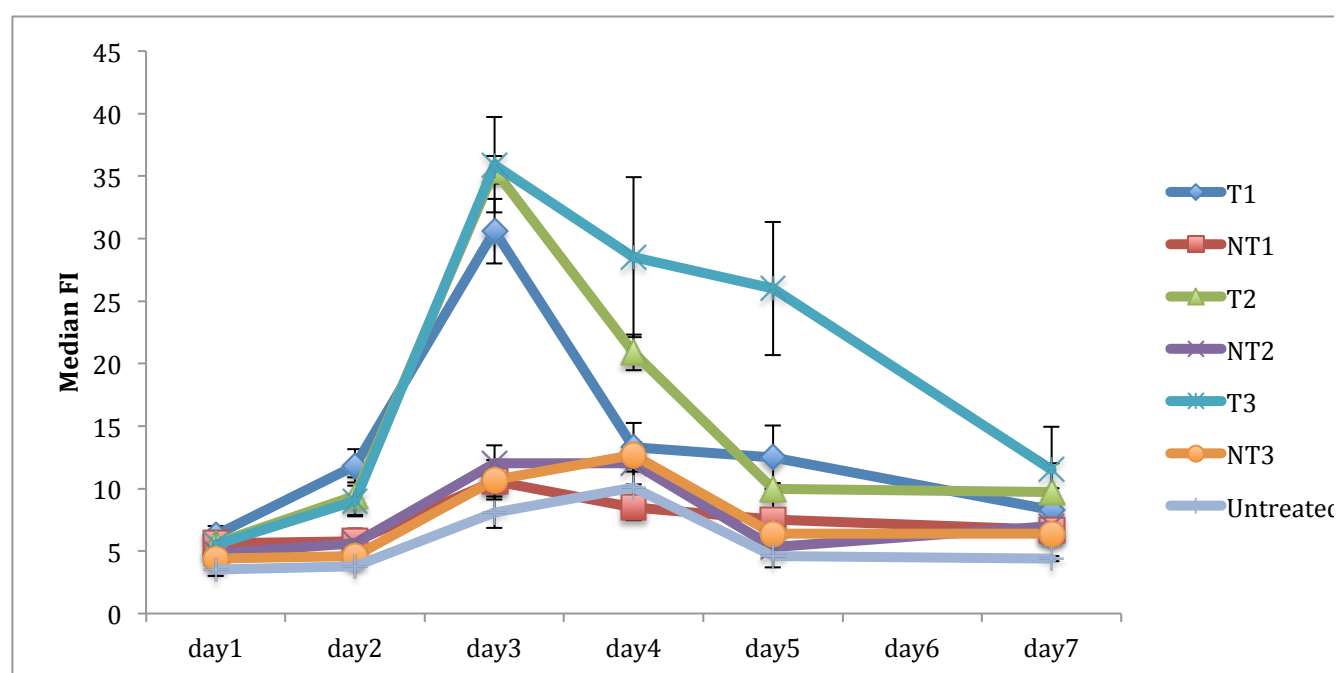
Figure 4.12: Intracellular levels of R123 in RBE4 cells given by the median FI. The measurements were carried out over seven days, using LIN350 and anti-Abcb1a (T1, T2, T3) or negative control siRNA (NT1, NT2, NT3) at 100 nM and N/P 30. R123 levels were measured at 24, 44, 72, 96, 120 and 168 h after the first transfection (day 1, 2, 3, 4, 5 and 7, respectively). At day 6 no measurements were carried out. Untreated cells were included as a control for fully functional P-gp.

Linear chitosans have previously been shown to give optimal P-gp knockdown efficiencies after 48 h in RBE4 cells (Jostein Malmo, unpublished results). In Figure 4.12 it was shown that LIN350 mediated highest knockdown efficiencies after 72 h (day 3), and these contradicting results were investigated. Since the measurements at day 2 were carried out after 44 h instead of 48 h (Figure 4.12), this could be the reason for the low knockdown observed. An R123 efflux assay was performed, measuring intracellular levels of R123 43, 48, 53 and 72 h after transfection, and the

results are shown in Figure 4.13. From this experiment it was confirmed that the knockdown efficiency of LIN350 and anti-Abcb1a siRNA was highest after 72 h in the RBE4 cells. There were minimal differences between the results 43, 48 and 53 h after transfection.
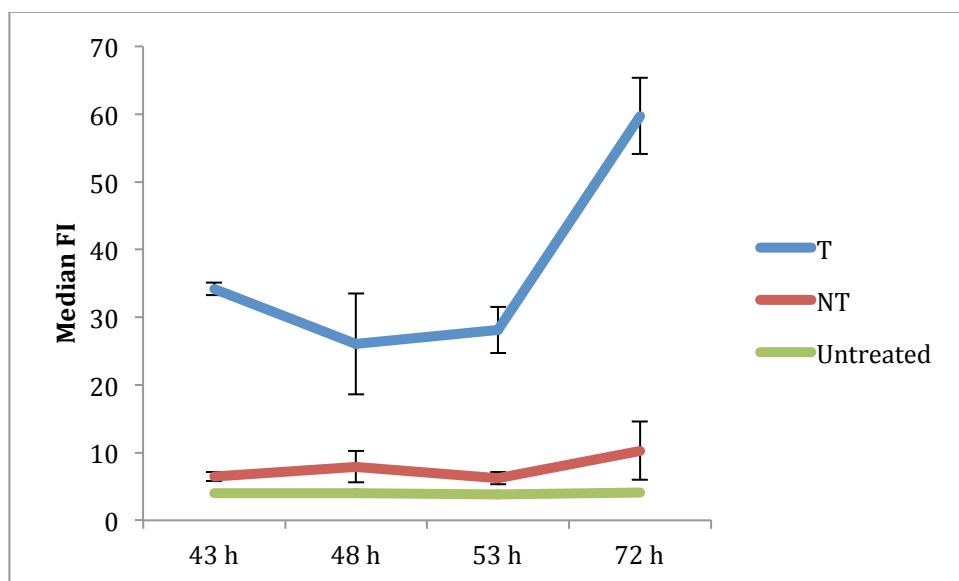
Figure 4.13: Intracellular levels of R123 in RBE4 cells transfected with LIN350 and anti-Abcb1a (T) or negative control (NT) siRNA at 100 nM and N/P 30, given by the median FI. Measurements were carried out after 43, 48, 53 and 72 h. The blue graph shows results from the anti-Abcb1a siRNA treated samples (T), the red graph shows results from the negative control siRNA treated samples (NT). The green line shows untreated cells, which were included as a control for fully functional P-gp.

Note: After it was found that LIN350 mediated the most efficient P-gp knockdown after 72 h in RBE4 cells, follow-up experiments with the C6 cell line measuring R123 efflux at this time were also carried out, but these experiment did not improve transfection efficiencies compared to 48 h and were therefore not included here.

4.3 Transmission Electron Microscopy of RBE4 cell samples treated with nanoparticles

The chitosan formulations with improved colloidal stability (F_a=0 (2% PEG), DP_{85} (4AM) and chitosans coated with HA) did not give promising results regarding transfection efficiencies. Since some of these chitosans mediated high uptake but did not provide efficient knockdown (Figure 4.7, 4.9 and 4.11), the uptake mechanisms and intracellular trafficking pathways of the different nanoparticles were investigated in order to identify the intracellular obstacles associated with each formulation. This could provide valuable insight into what uptake mechanism the nanoparticles utilize, and how to develop new chitosans with better transfection efficiencies and the same level of colloidal stability for future *in vivo* siRNA delivery.

For the transmission electron microscopy (TEM) experiments, gold particles (30 nm) were mixed with chitosan and siRNA for detection of the nanoparticles. Gold particles are reported to associate with nucleic acids in a wide range of diameters (2 – 250 nm) [92], and therefore seemed suitable for our experiments, since gold particles are very electron dense and can be easily spotted by TEM when investigating cell samples.

RBE4 cells were transfected with chitosan-gold-siRNA nanoparticles stained with gold and prepared for TEM. LIN350, LIN350 w/HA, F_a=0 (2% PEG) and DP_{85} (4 AM) were used along with anti-Luciferase siRNA (100 nM, as a non-targeting siRNA) and gold to form the nanoparticles, using N/P 30. There were two parallels for each sample. Since the cell samples were sectioned into 70 nm large slices, many of the cells were somewhat damaged or cut in two, etc. The pictures from the cell samples are presented in Figure 4.14 – 4.48. The pictures presented here are only a fraction of the actual amount of pictures taken, but serve as a representative selection for each of the samples. There are some overview pictures included, showing cell and organelle morphology, and some zoomed-in pictures giving a more detailed look on vesicles and uptake patterns where gold was present. In general, the samples did not contain as many gold particles as expected. For the chitosan samples, there were on average one gold particle in about every third cell, with some cells and some vesicles having more than this. In the gold control sample only a very small fraction of the cells had internalized gold particles. In pictures where the gold is difficult to spot, the area containing gold particles is marked with a red circle, as seen in the figures. In general, one gold particle was internalized along with many nanoparticle-looking formations, indicating either that not all complexes associated with gold in the first place, or that most of the gold was lost during cell preparations.
Note: For simplicity, the chitosan-gold-siRNA nanoparticles are sometimes referred to using only the name of the chitosan (e.g. LIN350).

Figure 4.14 shows an overview picture of how the cells looked like through the TEM microscope. The picture is taken from the untreated control sample, but is representative for all samples since the most detailed cell and organelle morphology was not detectable at this magnification.
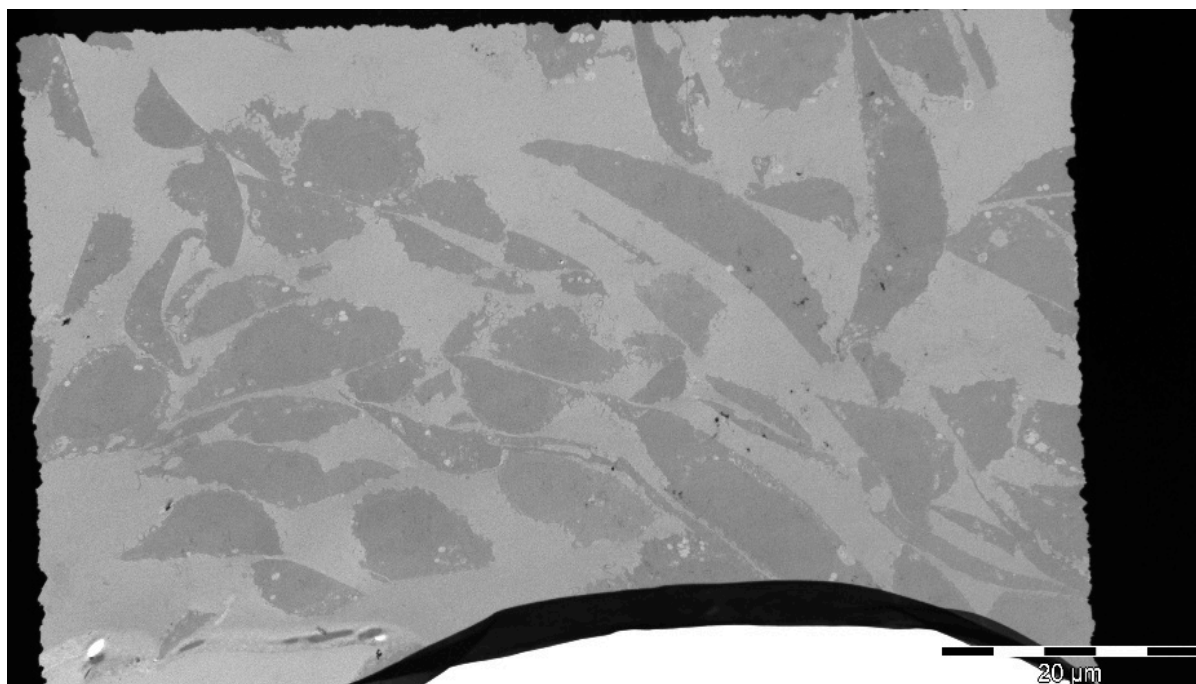
Figure 4.14: An overview picture of how the cells looked like using TEM. The picture is taken from the untreated control sample but is representative for all samples. The scale bar is 20 μm.

4.3.1 Samples treated with LIN350-based nanoparticles

Pictures obtained from the LIN350-treated samples are shown in Figures 4.15-4.22. As seen in the figures, there was no clear proof of nanoparticle presence. However, a repetitive pattern that was unique for the LIN350 samples was observed in both vesicles and in association with the cell membrane, and gold particles were often present around these unclear formations. In general, the gold-containing vesicles were large, from 0.5-2 μm. Although smaller vesicles were present in the cells, very few of these contained formations similar to the ones observed where gold was present; indicating that the nanoparticles possibly were internalized by macropinocytosis, since clathrin- and caveolae-mediated endocytosis usually create vesicles of smaller sizes (ranging from 50-500 nm) [27, 62].
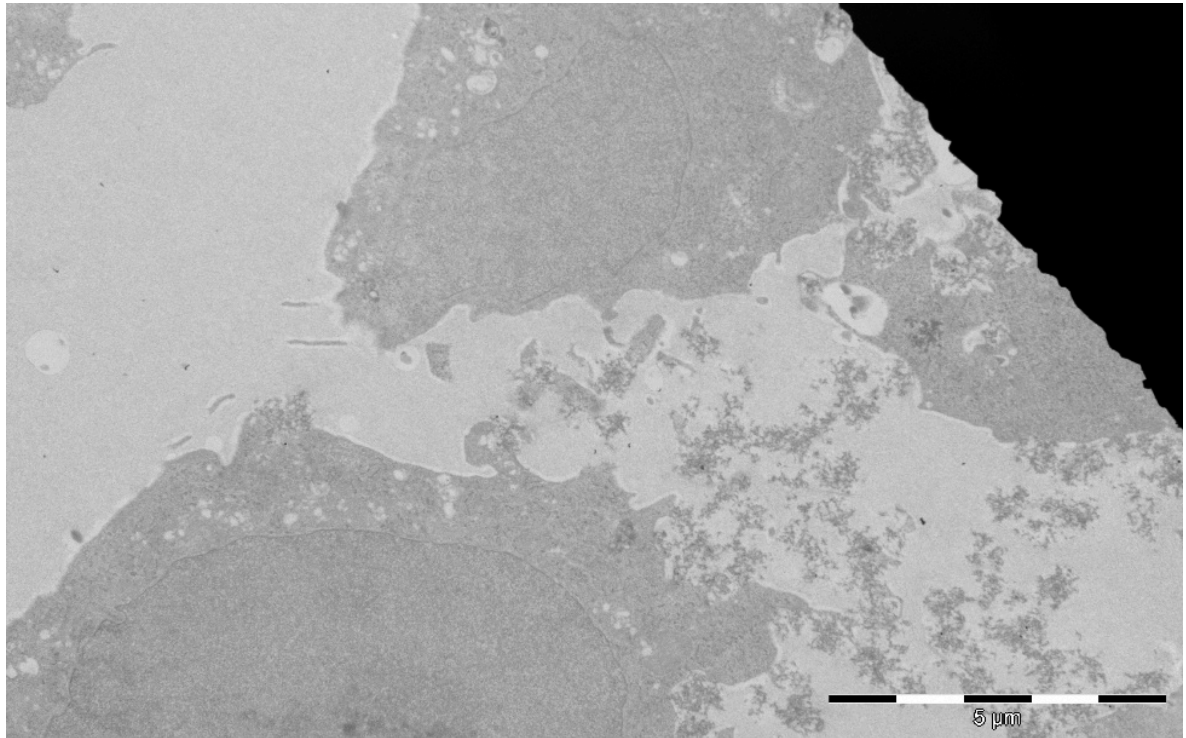
Figure 4.15: An overview picture of cells from the LIN350-treated sample, showing parts of three different cells. Cell nuclei (darker color, middle of the cells) and vesicles are shown. The shapes in the empty space between the cells are possibly nanoparticles. The scale bar is 5 µm.
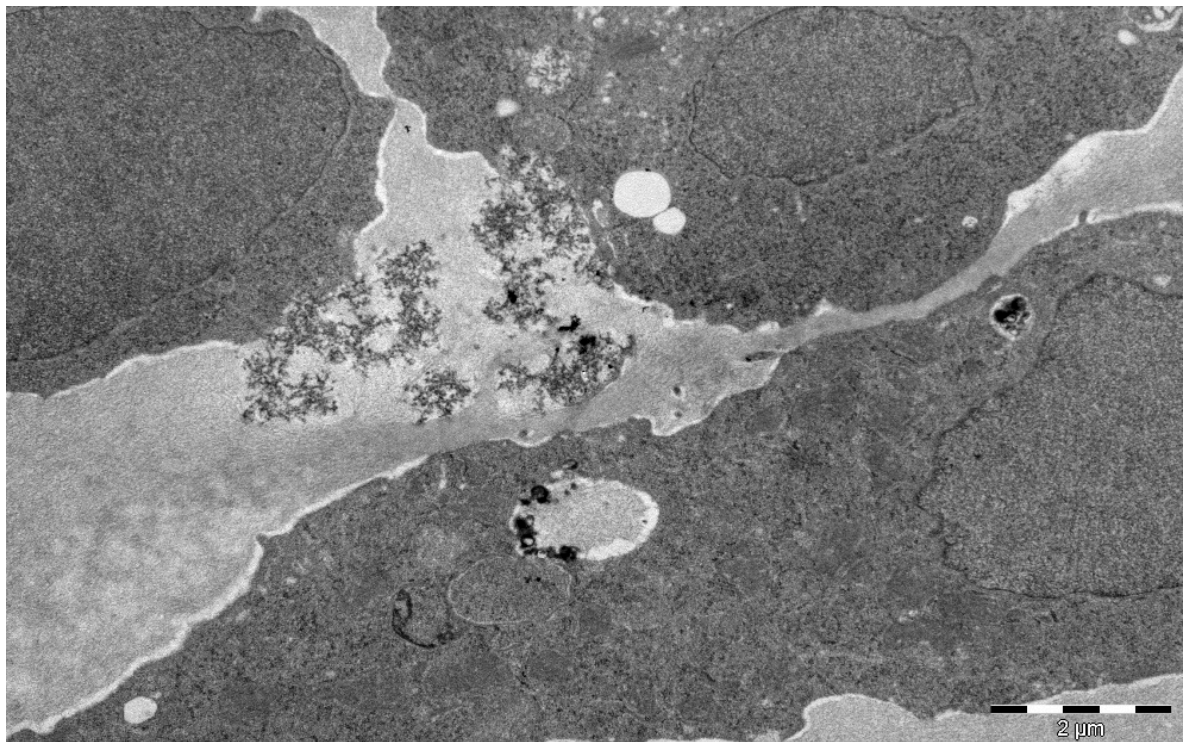
Figure 4.16: A closer look on cell morphology from a LIN350-treated sample, with extracellular content similar to the previous figure. The cells contain some vesicles of various sizes. The scale bar is 2 µm.
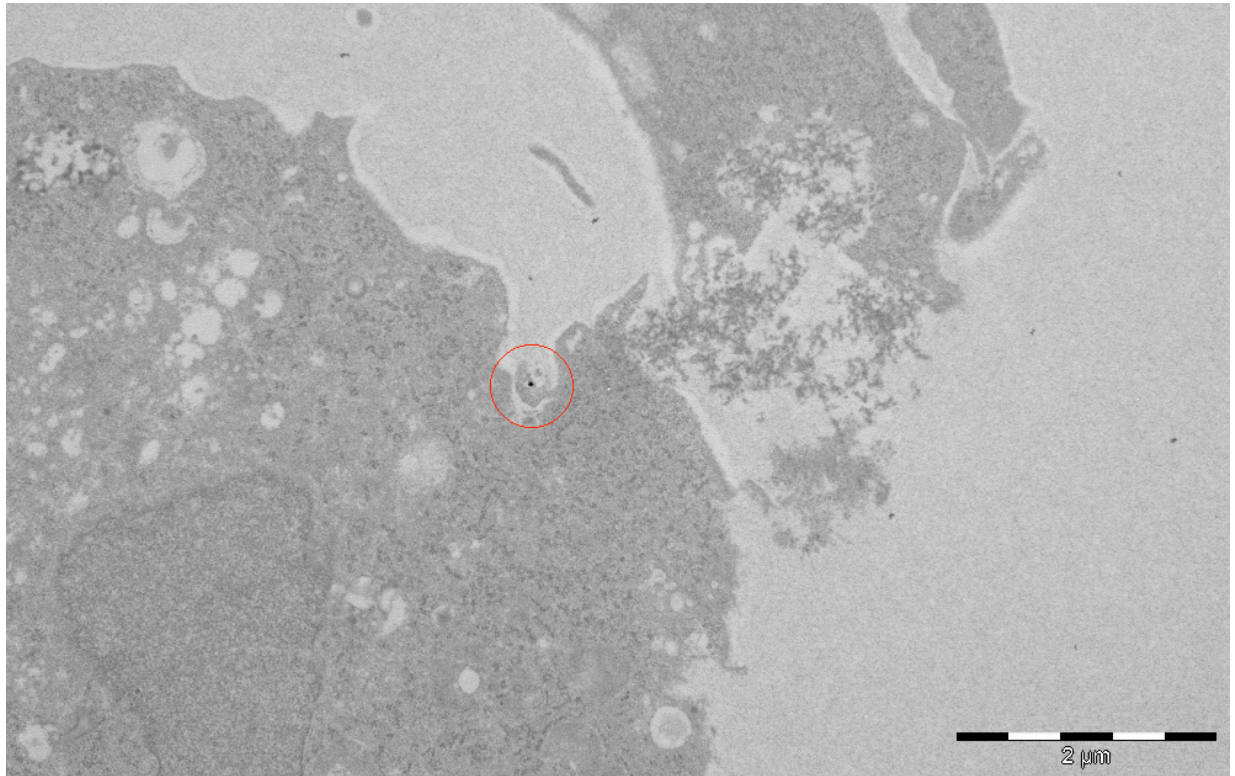
Figure 4.17: LIN350-treated cells, with one cell that is internalizing a gold particle, possibly with a nanoparticle (left), marked by a red circle. The cell to the right is internalizing some components, possibly nanoparticles, into a vesicle. The scale bar is 2 μm.
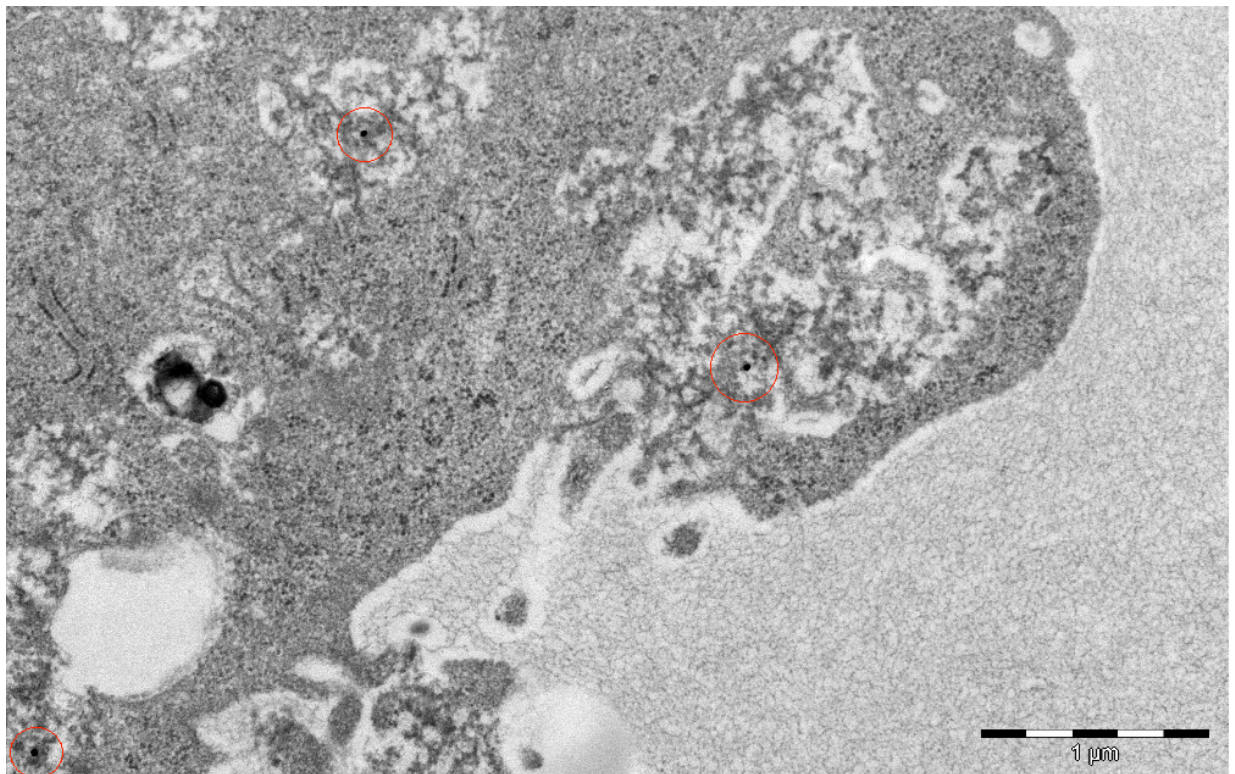
Figure 4.18: Gold particles that have been internalized into vesicles, possibly containing nanoparticles. The gold-containing vesicles are 1-3 μm in size. The picture is taken from a LIN350-treated sample. The scale bar is 1 μm.
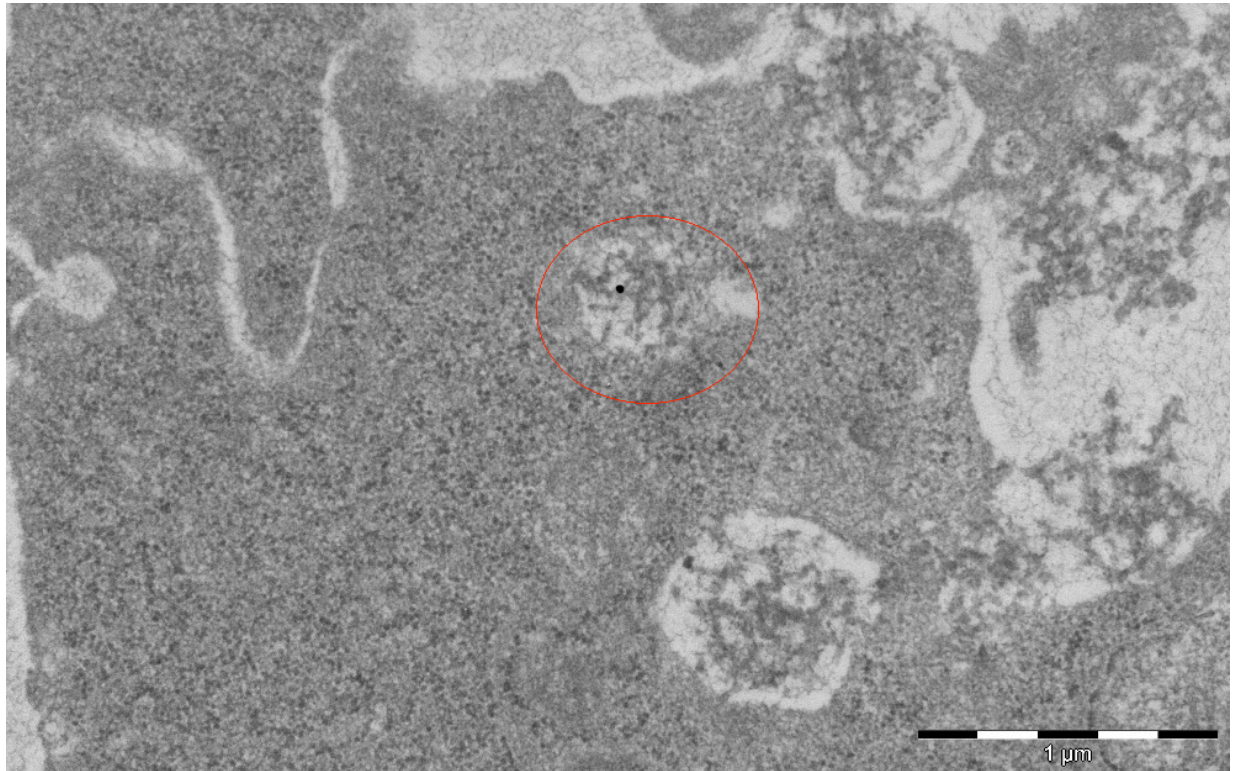
Figure 4.19: A gold particle and possible nanoparticles inside a vesicle. Another vesicle with similar content but without gold is seen below the upper one. To the right, similar formations are seen outside the cell. The picture is taken from a LIN350-treated sample. The scale bar is 1 μm.
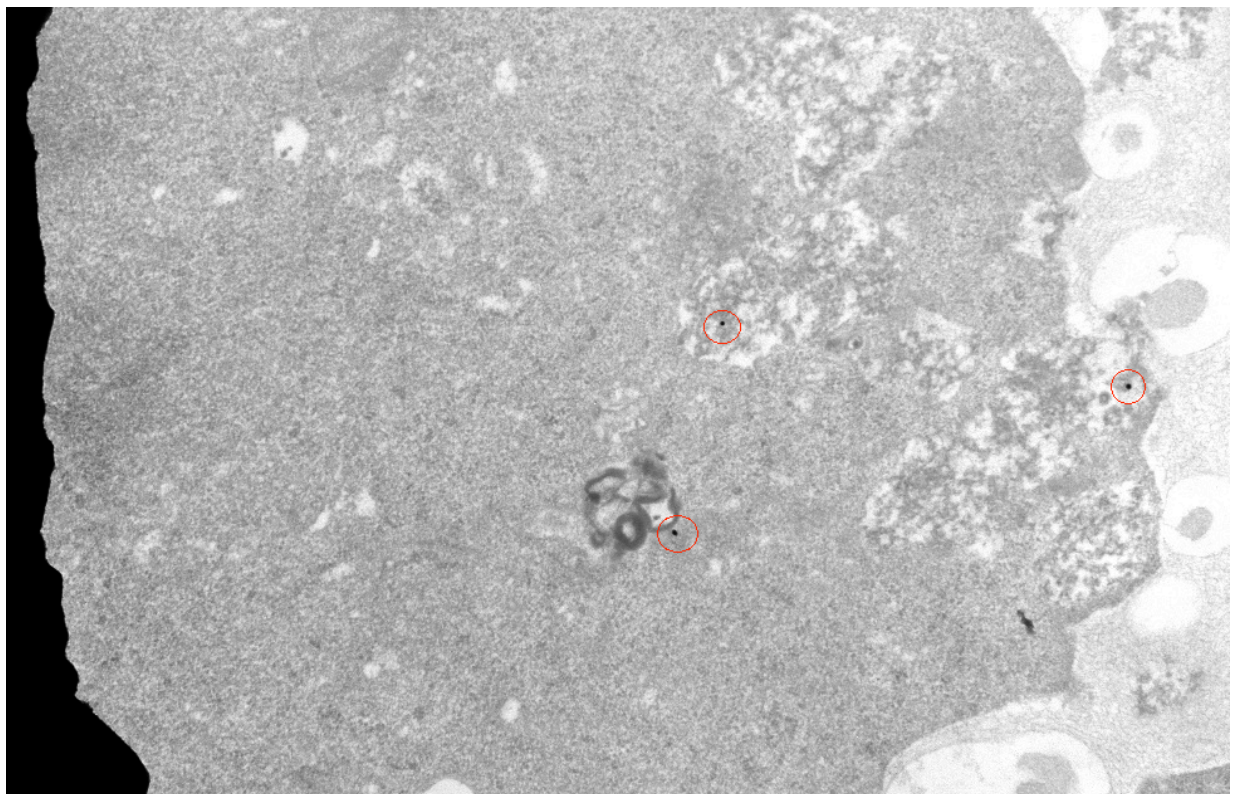
Figure 4.20: Three gold particles inside a cell from the LIN350-treated sample. The leftmost gold particle might be located in the cytosol, but is associated with some unknown structures, possibly in a vesicle. The two other gold particles are on their way to be internalized into a vesicular network, possibly containing nanoparticles.

47
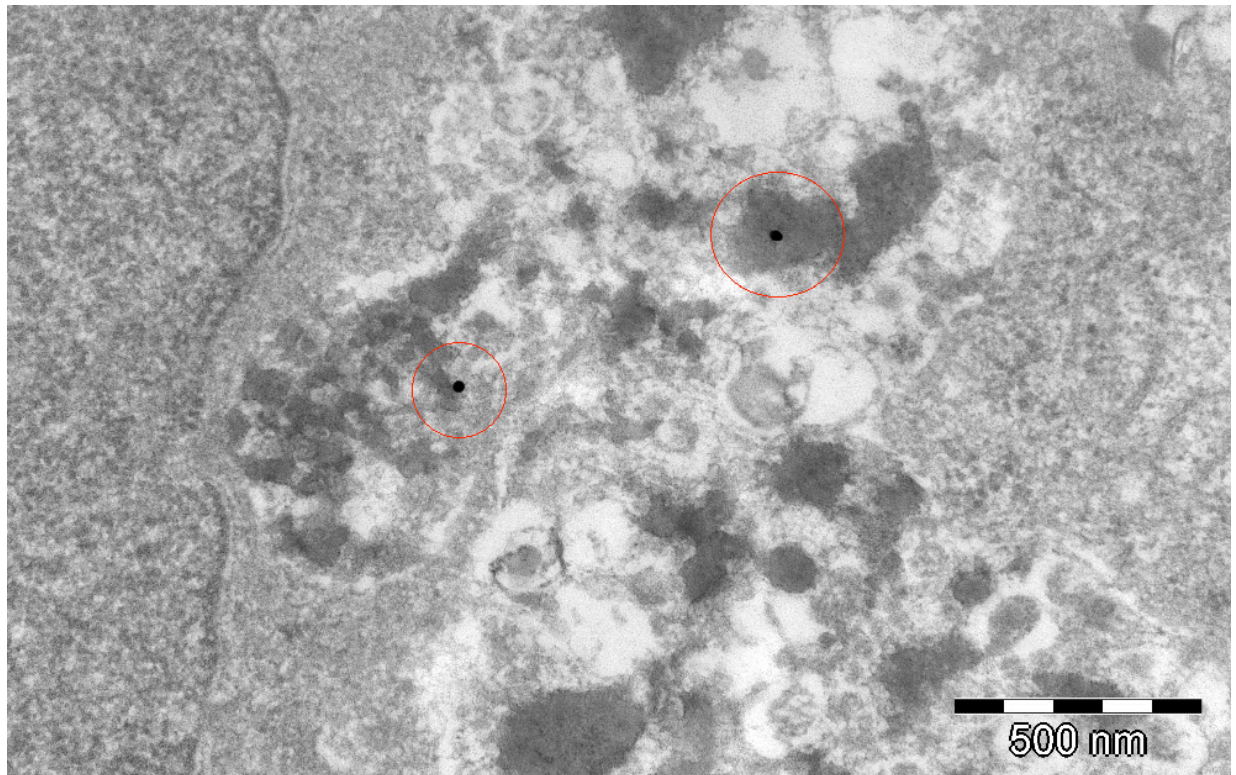
Figure 4.21: Two gold particles seen inside vesicles, with structures that could resemble nanoparticles. The structures vary in size, from 100-400 nm, with the largest ones potentially being nanoparticle aggregates of several hundred nm. The picture is taken from a LIN350-treated sample. The scale bar is 500 nm.
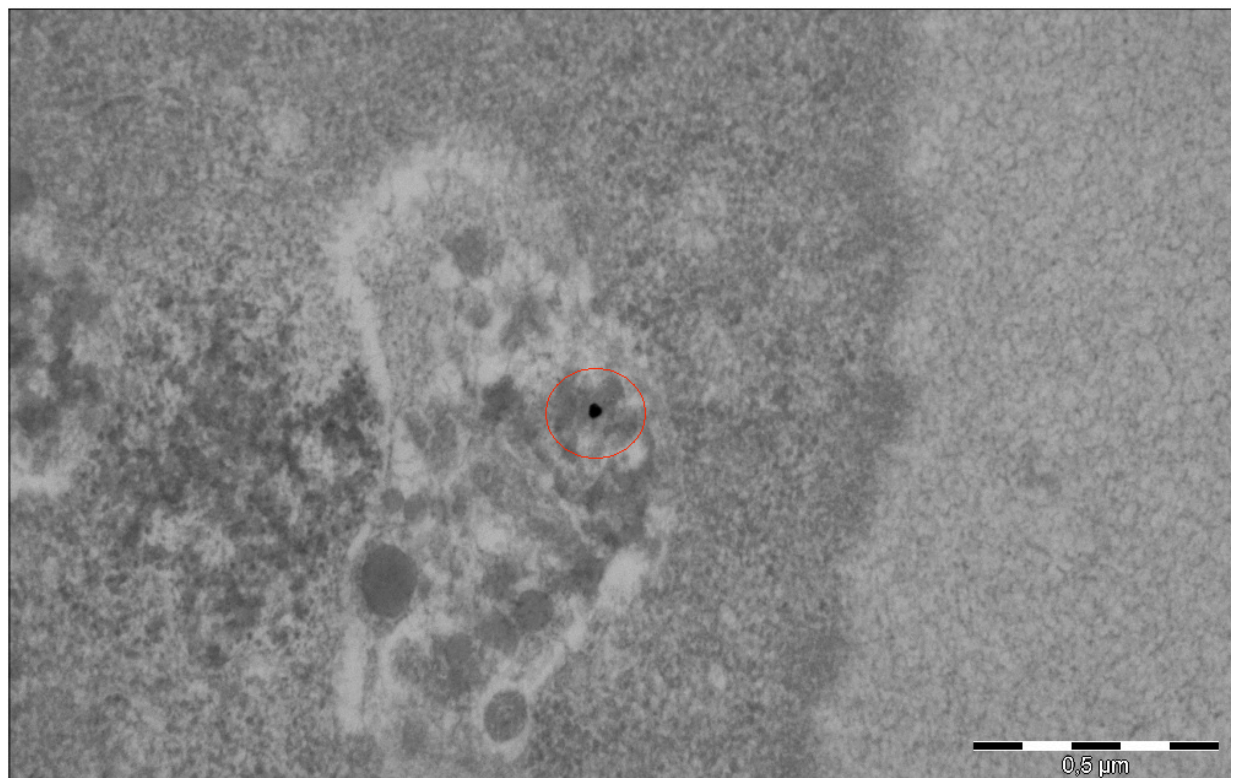
Figure 4.22: Another gold particle-containing vesicle, just inside the cell membrane of a cell from the LIN350-treated sample. The structures inside the vesicle could be nanoparticles but are hard to define as both shape and size vary. The scale bar is 0.5 μm.

4.3.2 Samples treated with LIN350 w/HA-based nanoparticles

Pictures obtained from the LIN350 w/HA-treated samples are shown in Figure 4.23-4.28. As seen in the figures, gold was often seen together with particles that could be LIN350 w/HA-containing nanoparticles. The sizes of these potential nanoparticles varied from 100-500 nm, indicating that some aggregation of the complexes had occurred. As with the LIN350-treated samples, the vesicles were usually larger than 500 nm, pointing toward uptake by macropinocytosis or some other mechanism creating large vesicles.
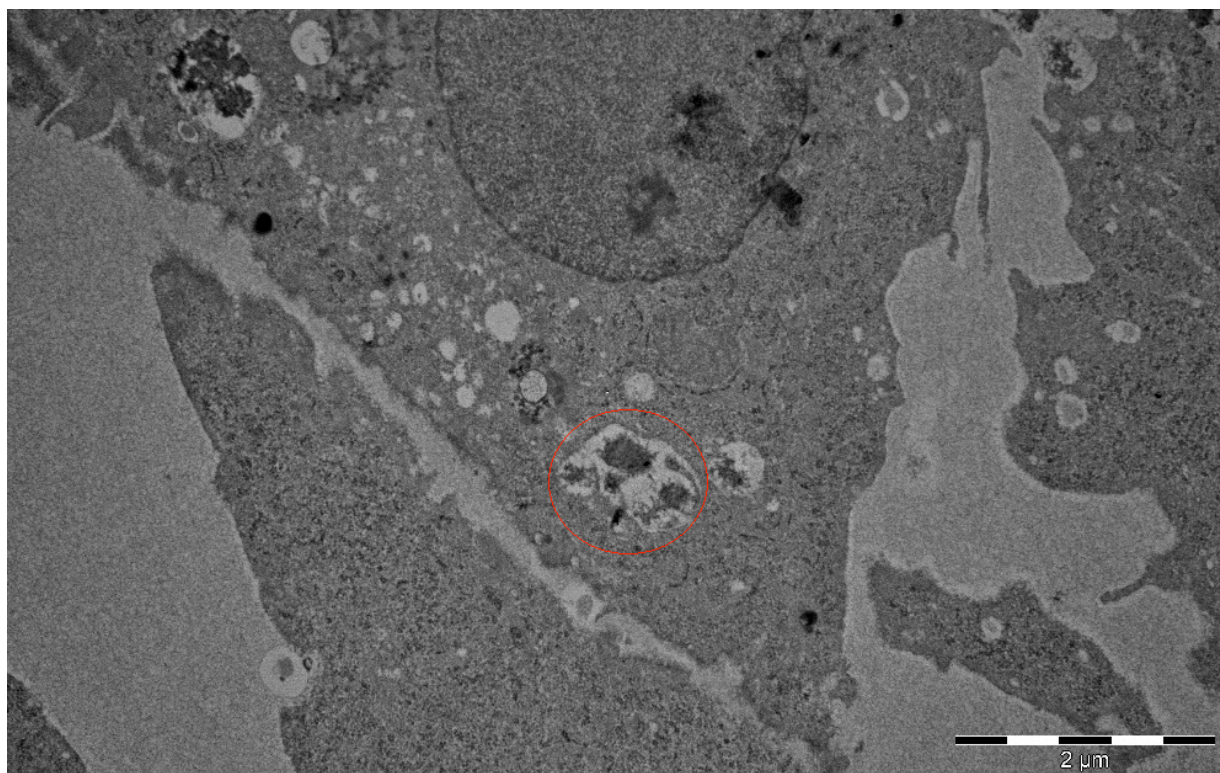
Figure 4.23: An overview picture of cells from the LIN350 w/HA-treated sample. In one of the cells, a vesicle of 1 μm contains a gold particle together with what could be nanoparticles. The scale bar is 2 μm.

49
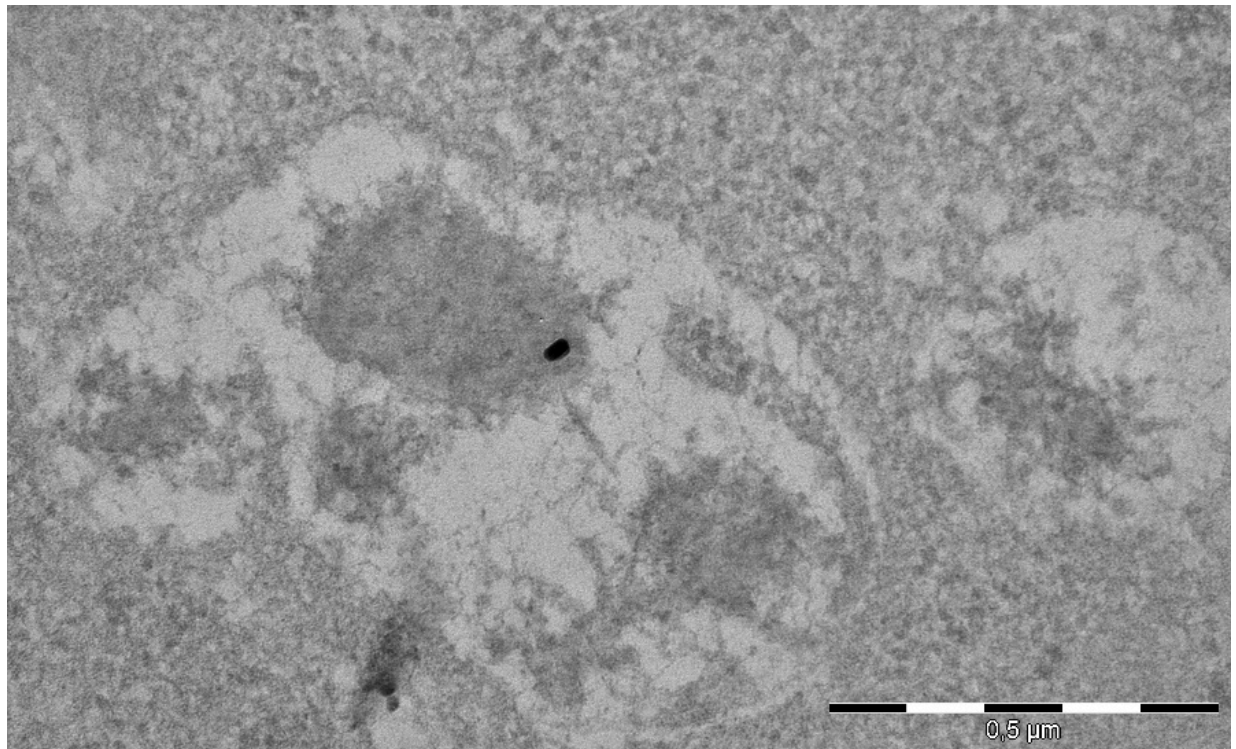
Figure 4.24: A close-up view of the vesicle from the previous figure, showing the vesicle with a gold particle associated with a particle about 200-400 nm large, which could be an aggregation of LIN350 w/HA nanoparticles. The picture is taken from the LIN350 w/HA-treated sample. The scale bar is 0.5 μm.
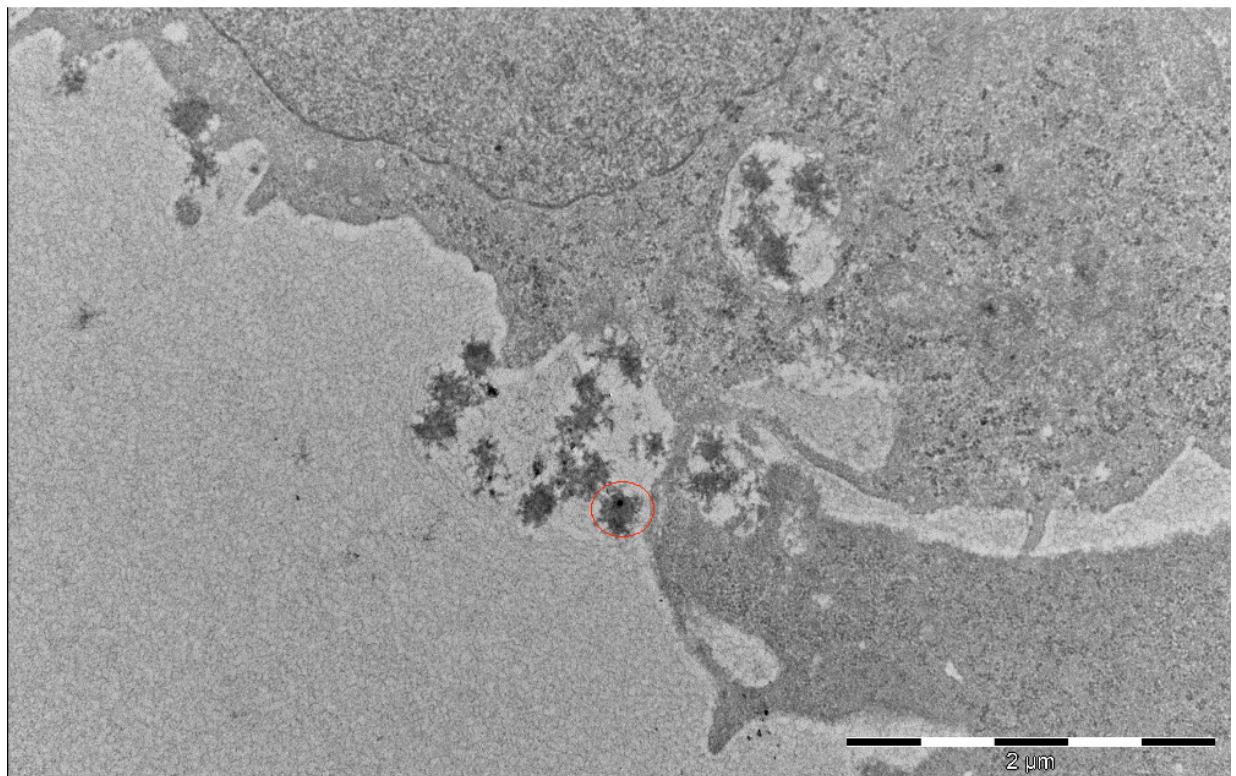
Figure 4.25: A cell from the LIN350 w/HA treated sample internalizes a gold particle and what could be nanoparticles. Right below the cell nucleus is a vesicle of about 500 nm, containing particles similar to the ones outside the cell membrane. The scale bar is 2 μm.
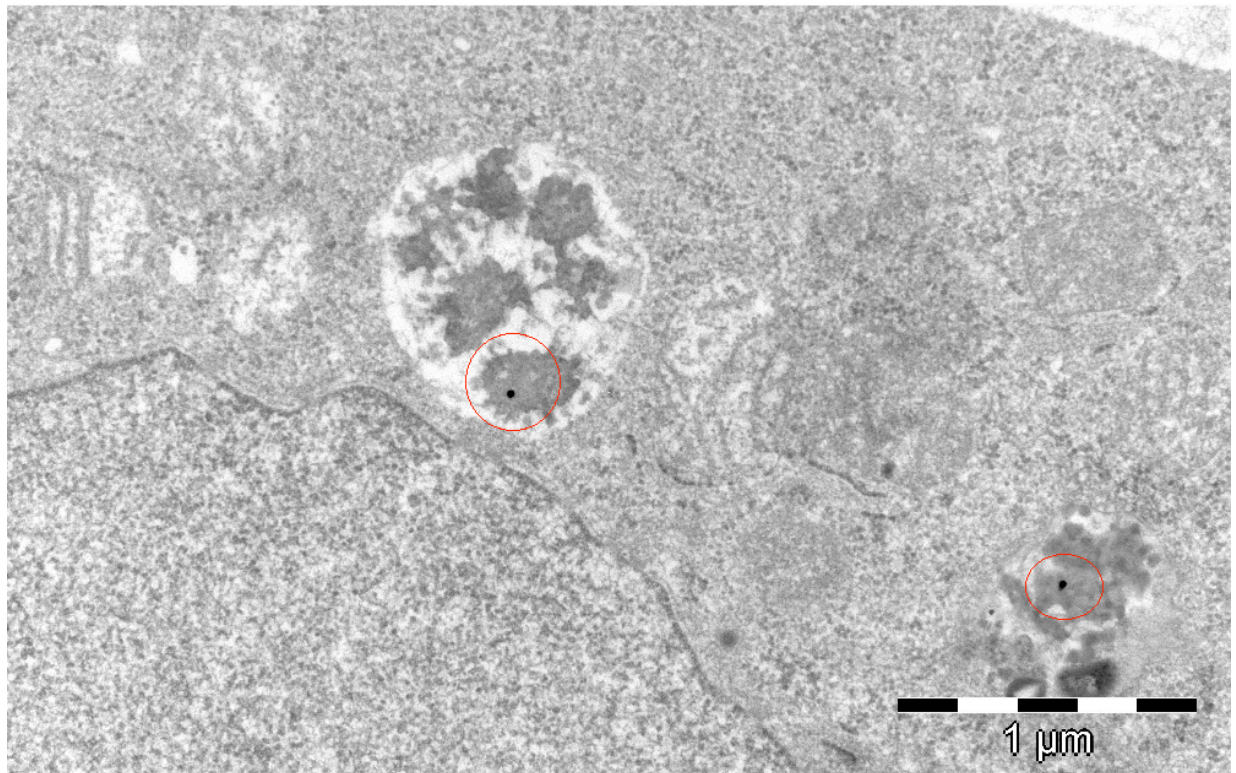
Figure 4.26: Two gold particles inside vesicles in a cell from the LIN350 w/HA-treated sample. The uppermost vesicle contains several nanoparticle-like shapes. The vesicle to the right contains a gold particle along with some undefined shapes, possibly aggregated nanoparticles.
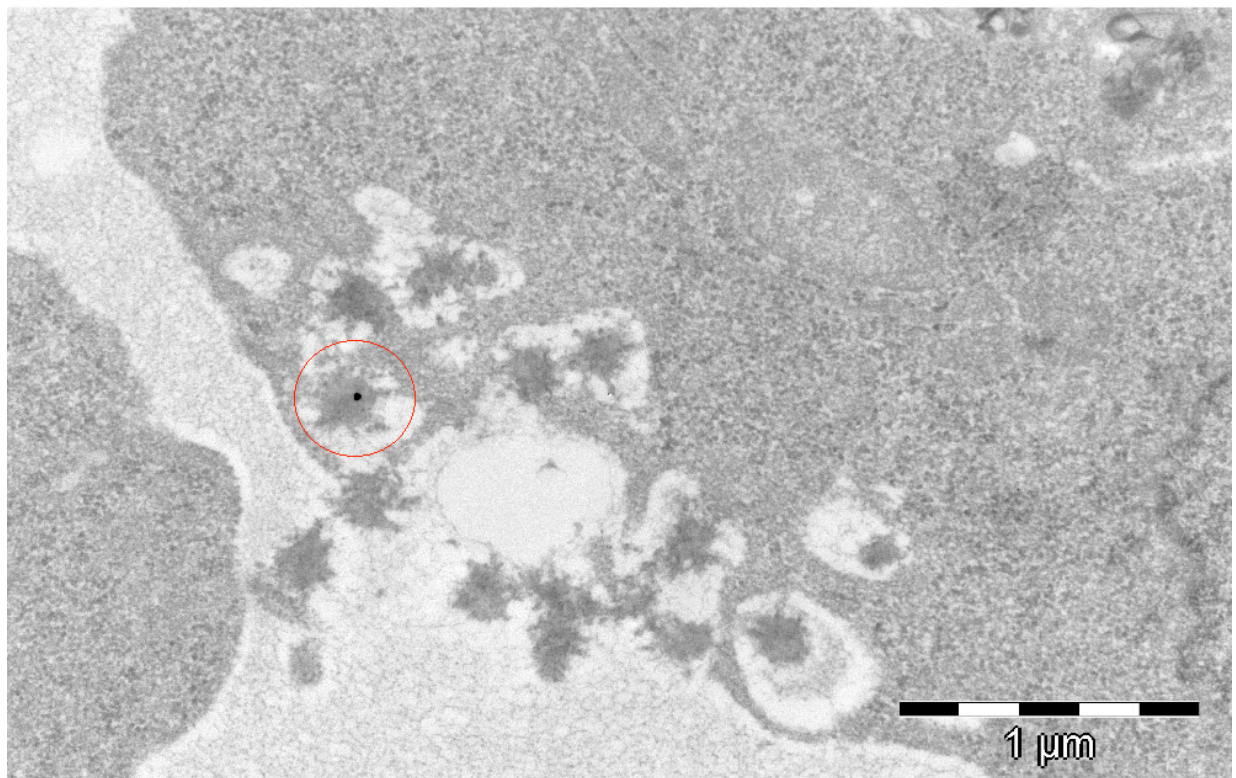
Figure 4.27: Many vesicles of intermediate sizes created in the cell membrane of a cell from the LIN350 w/HA-treated sample. One possible chitosan-gold-siRNA nanoparticle is present to the left (surrounded by the red circle), while the other vesicles contain what look like nanoparticles, but without gold. The scale bar is 1 μm.
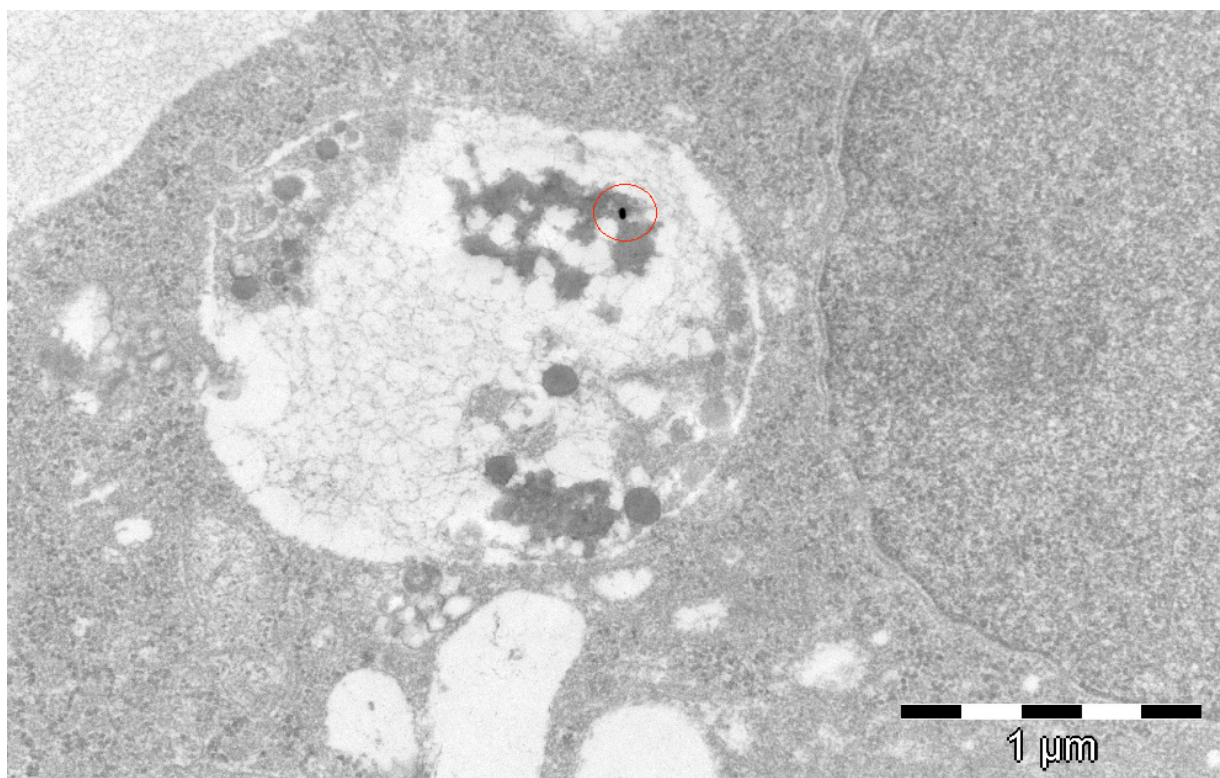
Figure 4.28: A vesicle of 1.5-2 μm, containing a gold particle and possibly nanoparticles, taken from a cell from the LIN350 w/HA-treated sample. The scale bar is 1 μm.

4.3.3 Samples treated with F_a=0 (2% PEG)-based nanoparticles

Pictures obtained from the F_a=0 (2% PEG)-treated samples are shown in Figure 4.29-4.36. These figures show that similar to LIN350 and LIN350 w/HA, the gold particles were found mainly in large vesicles of sizes above 500 nm, again pointing toward uptake by macropinocytosis. Although potential nanoparticles were hard to spot, a repetitive pattern unique for the F_a=0 (2% PEG) samples was found in most of the gold-containing vesicles, indicating presence of either nanoparticles, or fragments or aggregations of these.
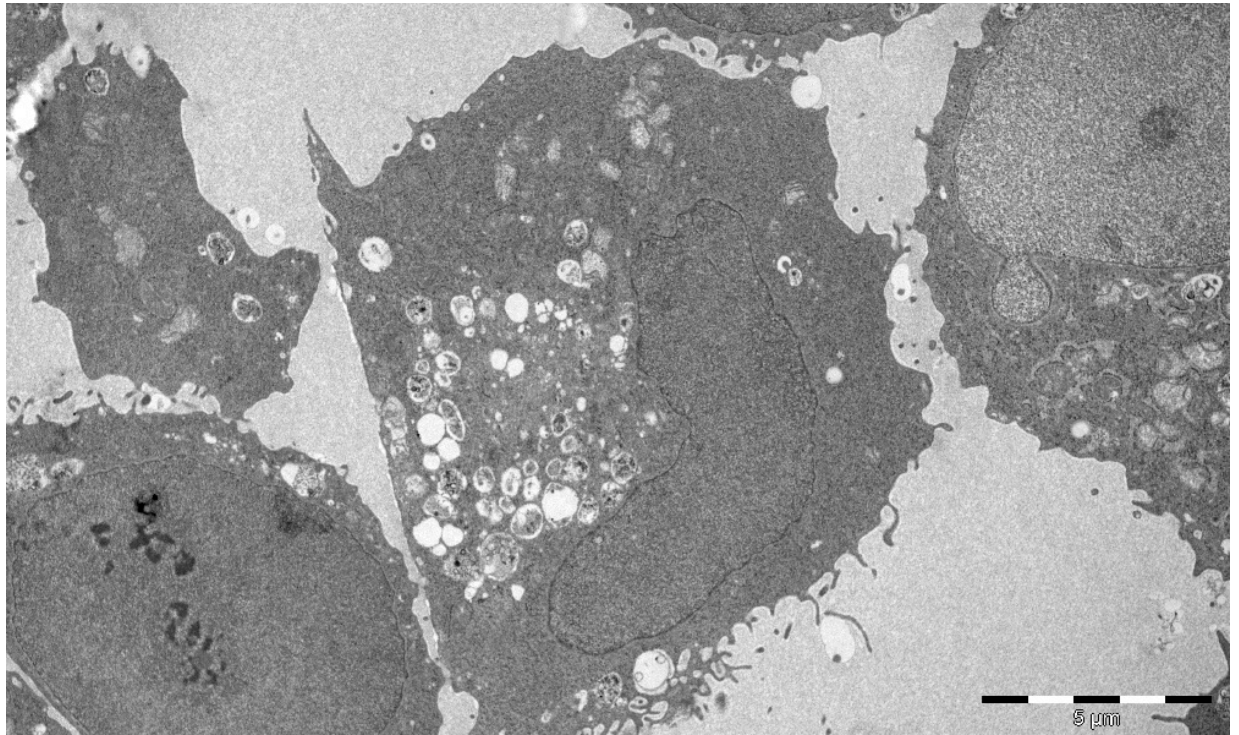
Figure 4.29: An overview of several cells from the F_a=0 (2% PEG) sample. Numerous vesicles are present in the cell located in the middle of the figure. The scale bar is 5 μm.
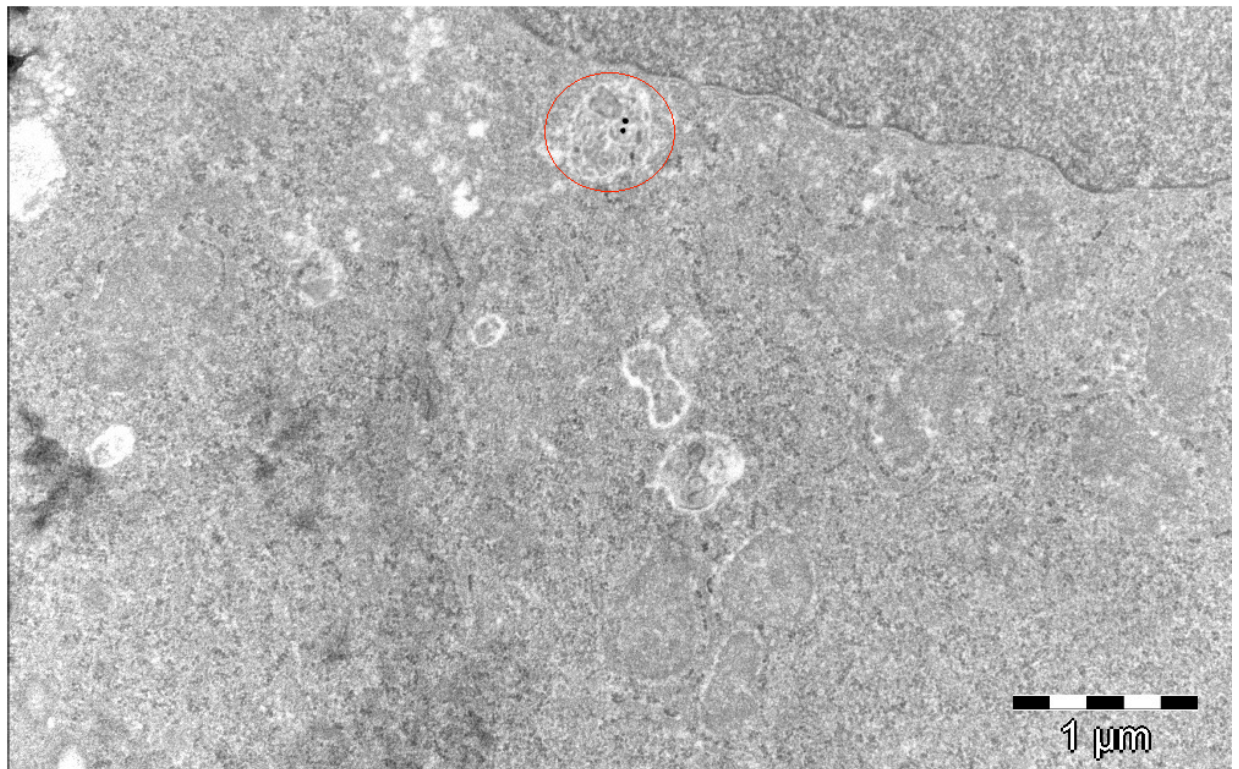
Figure 4.30: A cell from the F_a=0 (2% PEG)-treated sample with several vesicles, one of them being close to the cell nucleus, containing two gold particles. The scale bar is 1 μm.
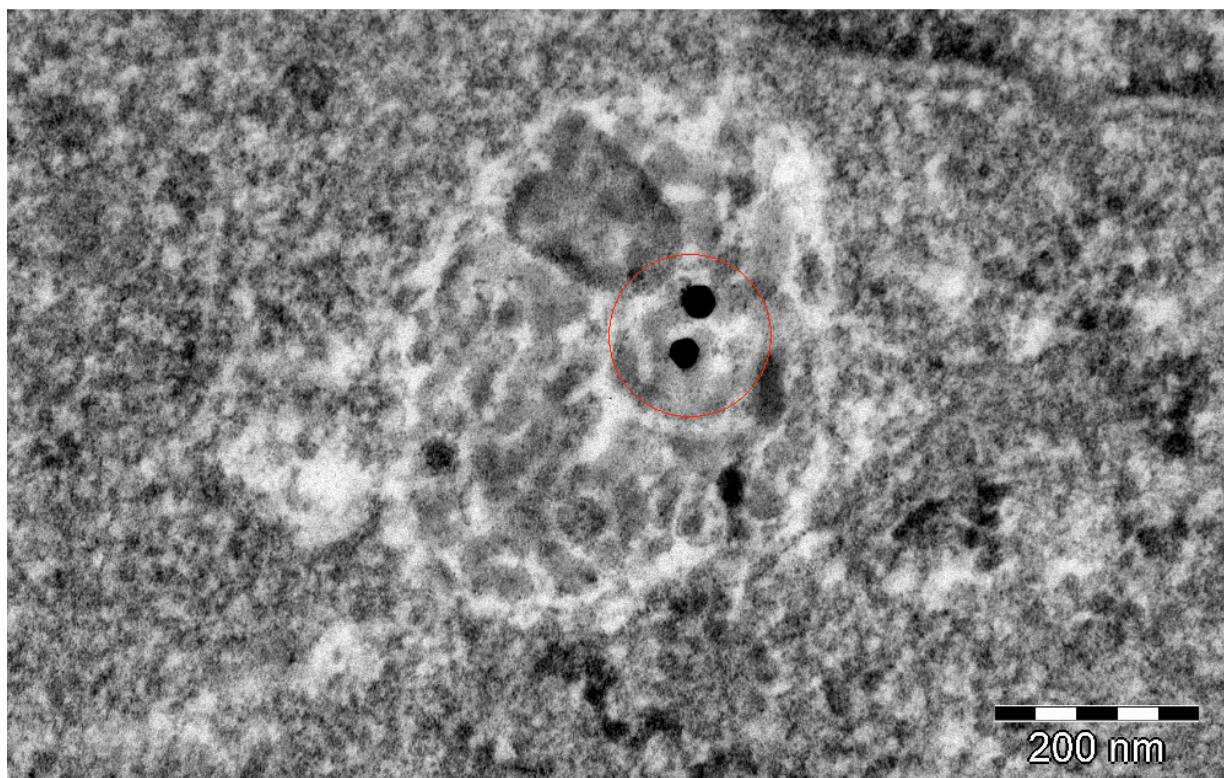
Figure 4.31: A close-up view of the vesicle from the previous figure, showing the two gold particles. Some of the structures inside the vesicle, especially the one top-left of the gold, could be nanoparticles, with a size of about 150-200 nm. The picture is taken from the $F_a=0$ (2% PEG)-treated sample. The scale bar is 200 nm.
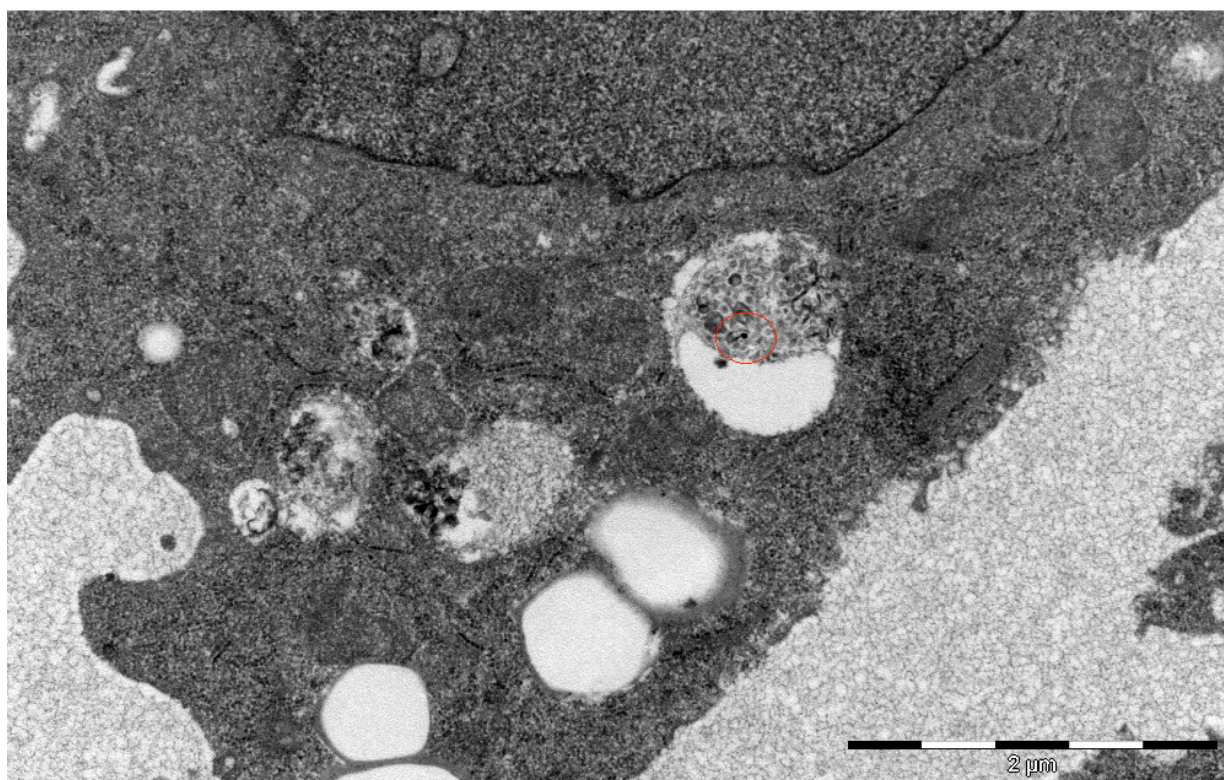
Figure 4.32: A cell from the $F_a=0$ (2% PEG)-treated sample with several vesicles. The red circle shows a gold particle inside a vesicle of 1 µm. The scale bar is 2 µm.
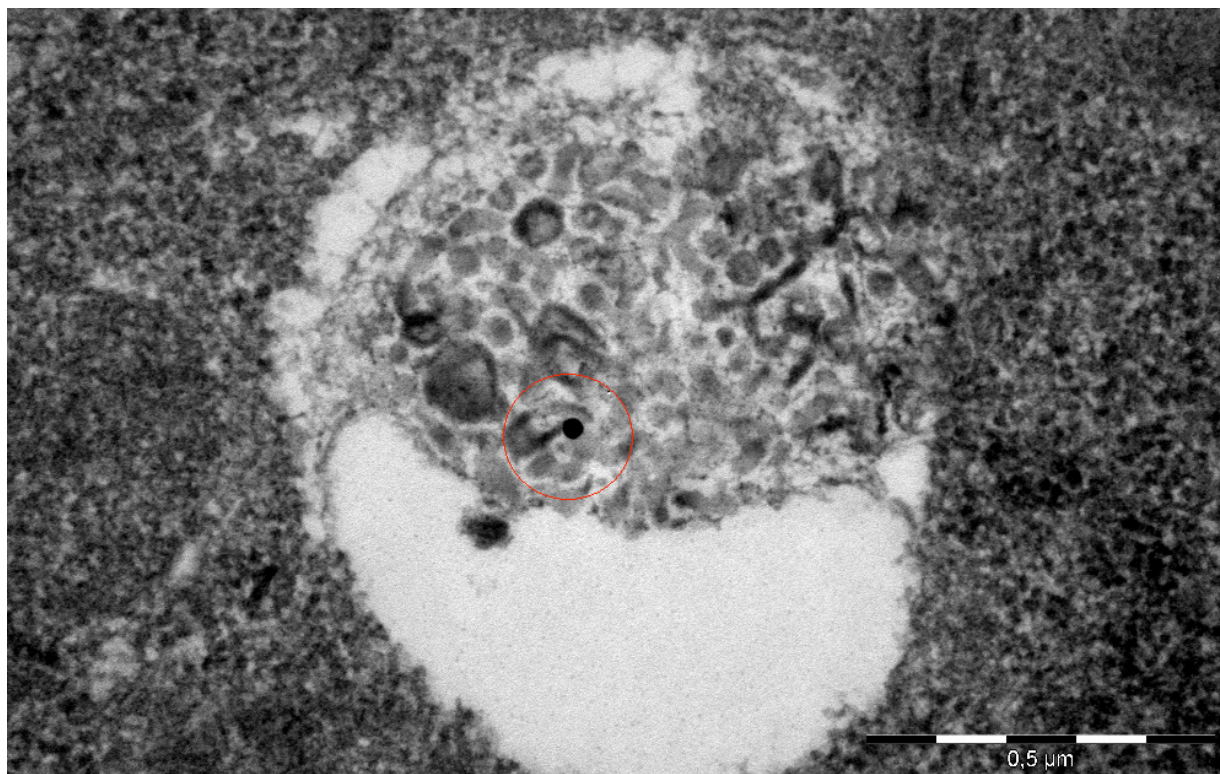
Figure 4.33: A close-up view of the vesicle from the previous figure, showing gold along with a structure similar to the ones found in the other pictures. The picture is taken from the $F_a=0$ (2% PEG)-treated sample. The scale bar is 0.5 μm.
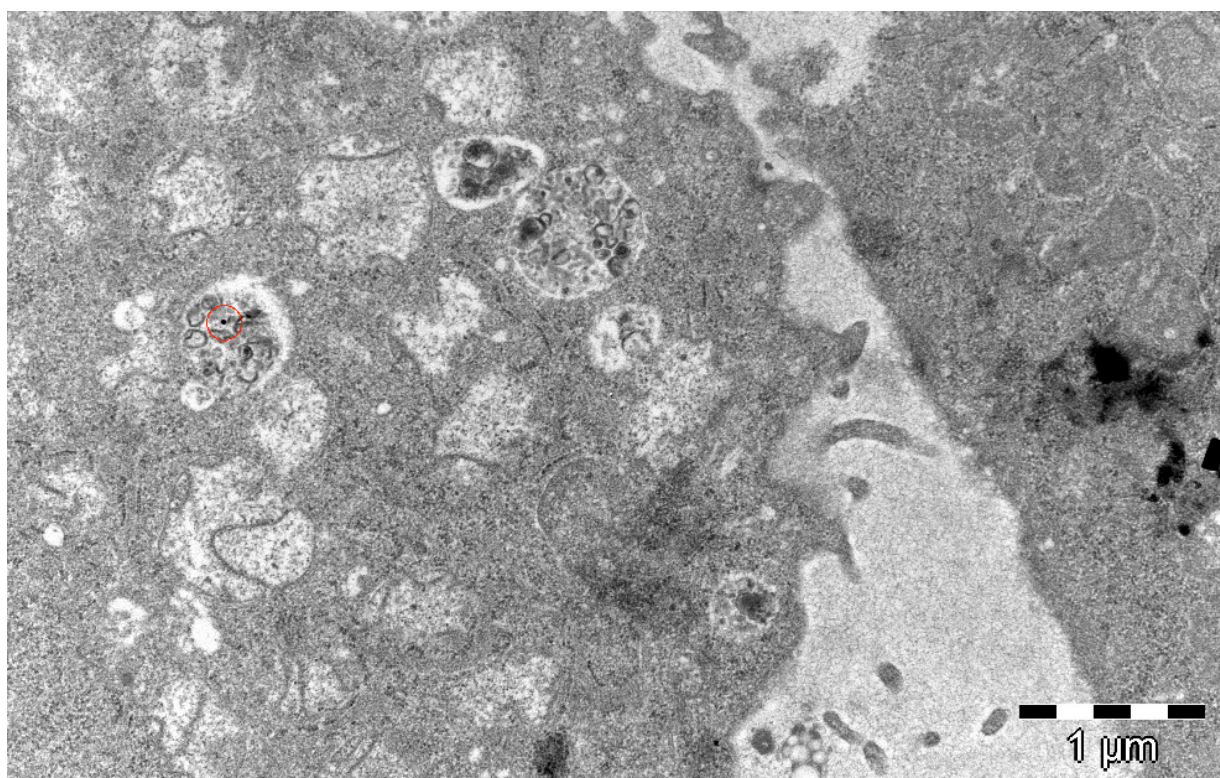
Figure 4.34: A cell from the $F_a=0$ (2% PEG)-treated sample containing many vesicles, one with a gold particle. Many of the shapes seen in this vesicle, and the large one to the right, were unique for the $F_a=0$ (2% PEG) samples, and could be nanoparticles. The scale bar is 1 μm.
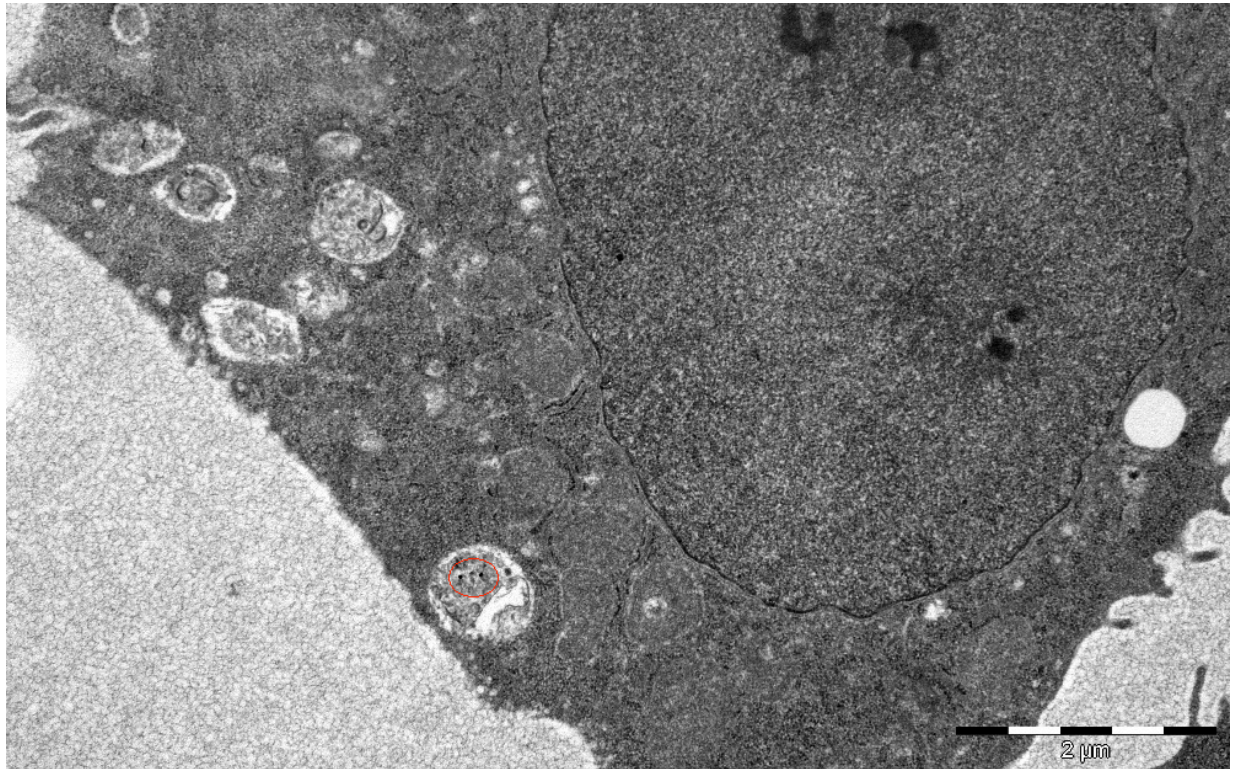
Figure 4.35: Another picture of a cell from the F_a=0 (2% PEG)-treated sample, containing several vesicles, one of them with two gold particles and possibly nanoparticles. The scale bar is 2 μm.
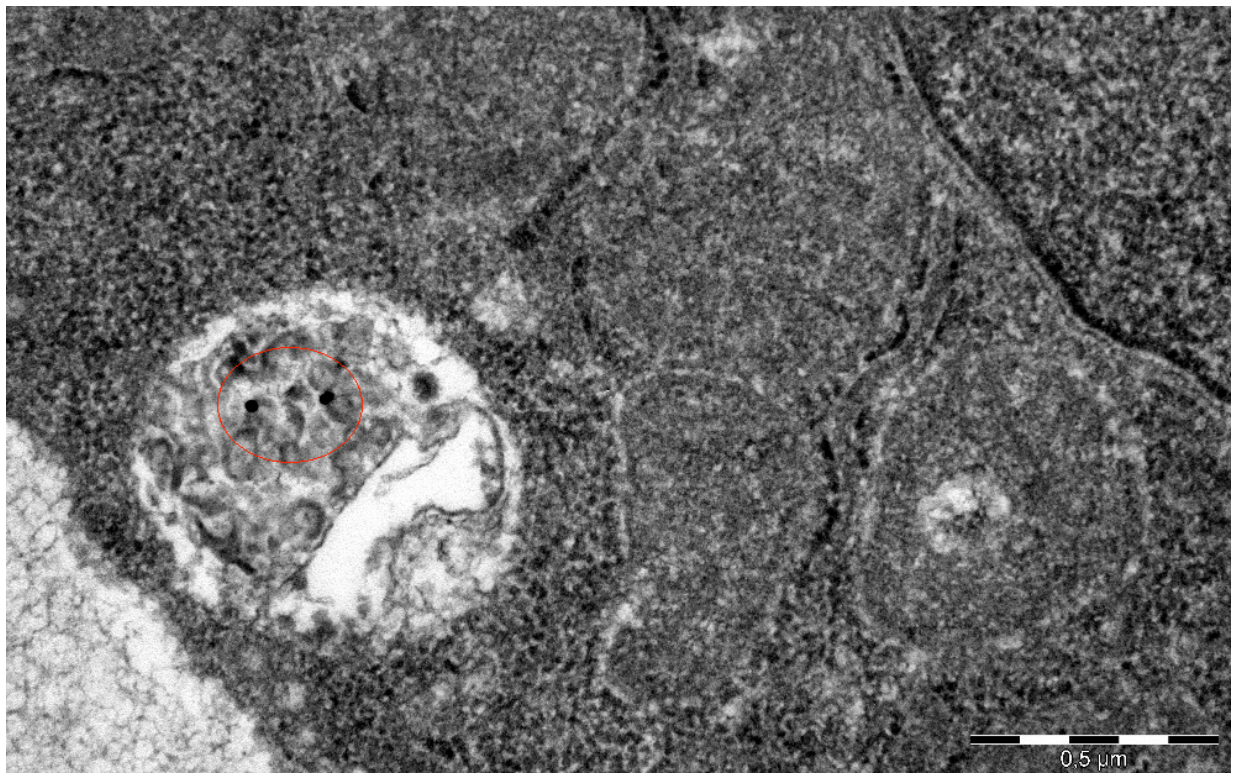
Figure 4.36: A close-up view of the vesicle from the previous figure, showing the intravesicular content and two gold particles. The picture is taken from the F_a=0 (2% PEG)-treated sample. The scale bar is 0.5 μm.

4.3.4 Samples treated with DP$_{85}$ (4AM)-based nanoparticles

Pictures obtained from the DP$_{85}$ (4AM)-treated samples are shown in Figure 4.37-4.42. The figures show that similar to the other chitosan samples, the gold particles were located mainly in large vesicles of sizes above 500 nm, again pointing toward uptake by macropinocytosis. Nanoparticle shape was easier to characterize with this chitosan, being more electron dense and having clearer shapes.
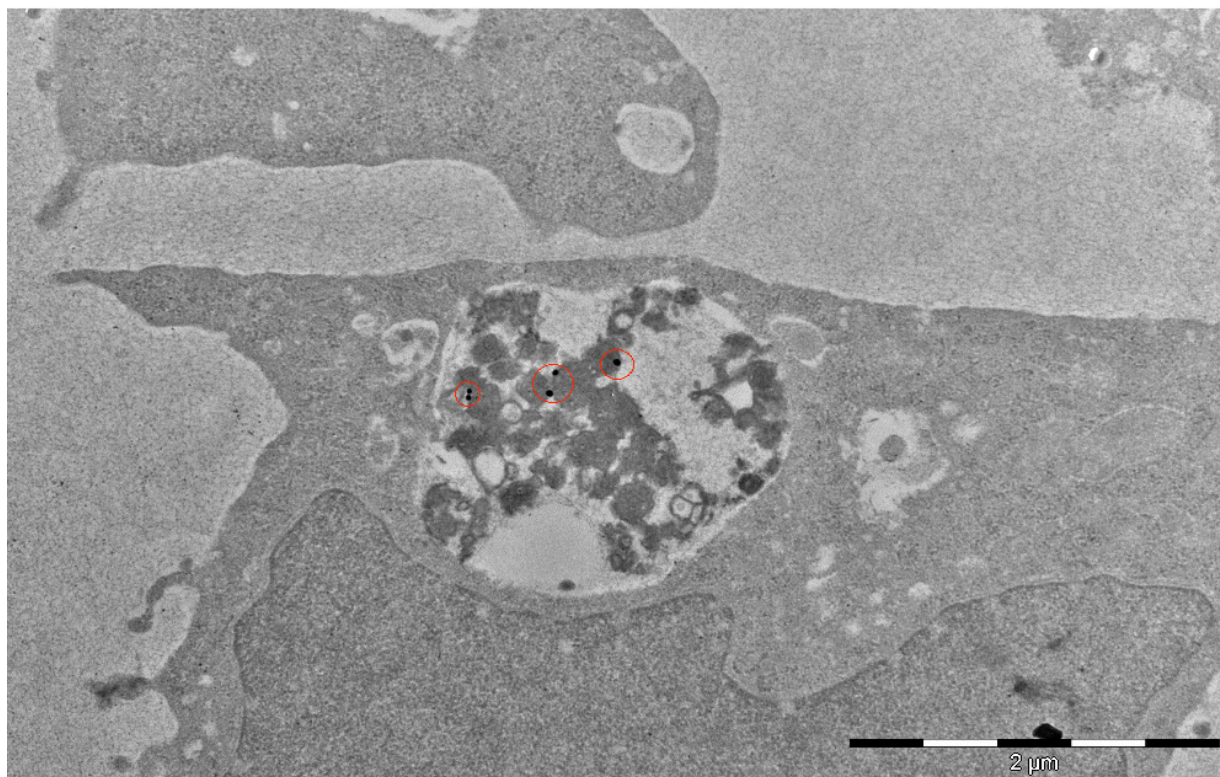
Figure 4.37: A vesicle with five gold particles and possible nanoparticles or aggregates. The picture is taken from the DP$_{85}$ (4AM)-treated sample. The scale bar is 2 µm.
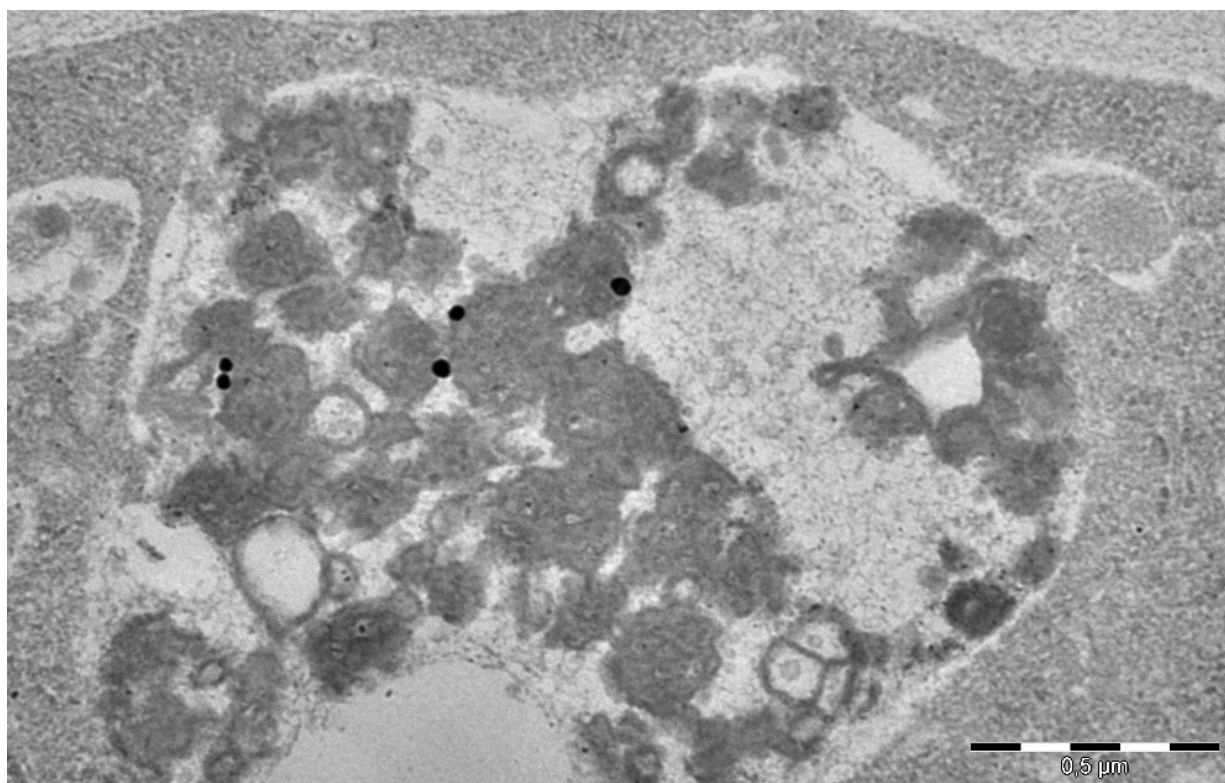
Figure 4.38: A close-up view of the vesicle from the previous figure, showing the five gold particles and many shapes that resemble nanoparticles, with sizes around 100-200 nm and possible aggregation of the nanoparticles several places. The picture is taken from the DP_{85} (4AM)-treated sample. The scale bar is 0.5 μm.
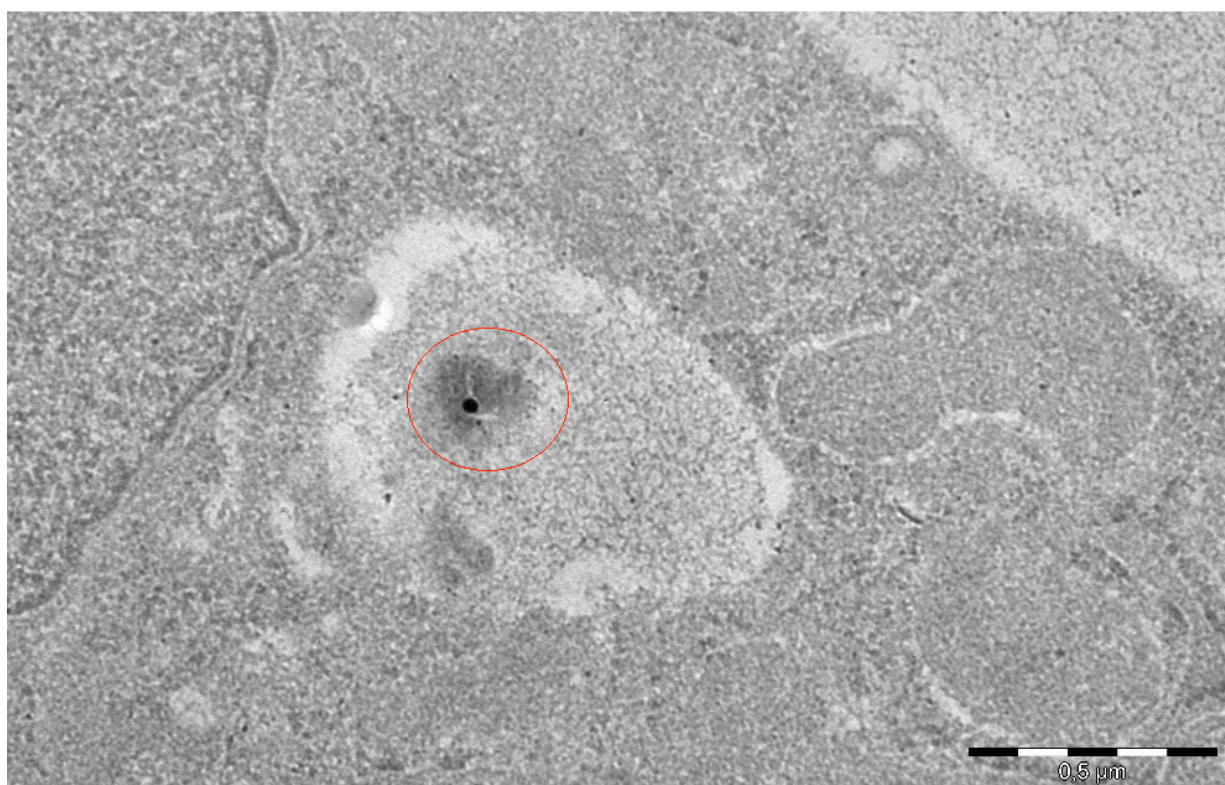
Figure 4.39: A vesicle containing one gold particle and possibly a nanoparticle with a size about 150-200 nm. The picture is taken from the DP_{85} (4AM)-treated sample. The scale bar is 0.5 μm.
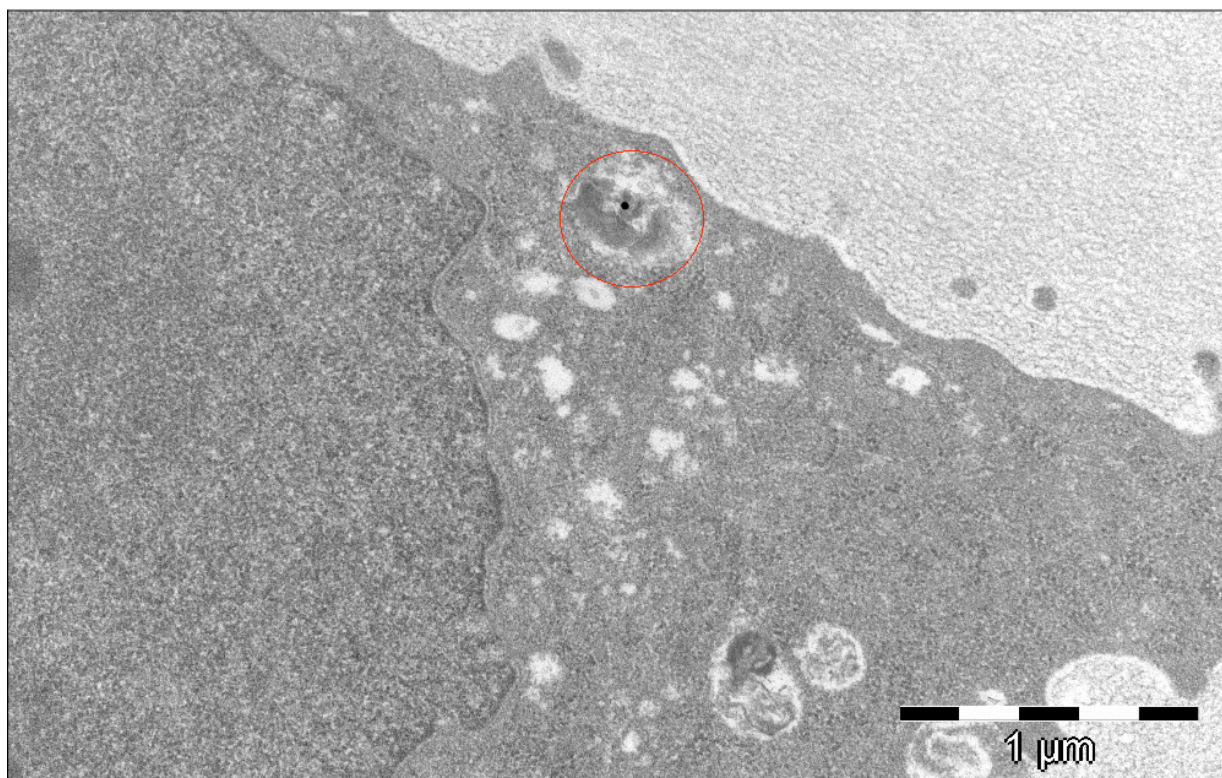
Figure 4.40: A gold particle inside a vesicle of about 200-300 nm, possibly with aggregated nanoparticles. Further inside the cell there are several smaller vesicles of around 100 nm, but these do not contain any visible cargo. The picture is taken from the DP_{85} (4AM)-treated sample. The scale bar is 1 μm.
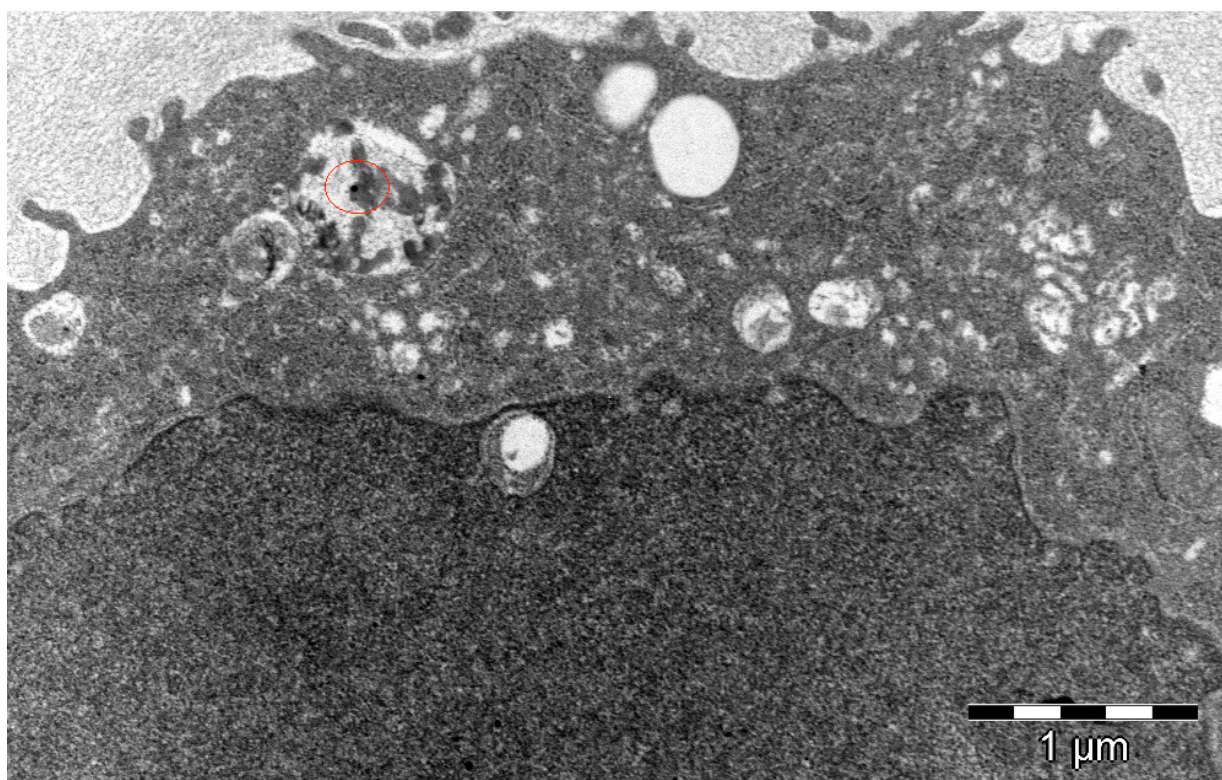
Figure 4.41: A cell from the DP_{85} (4AM)-treated sample with numerous vesicles of various sizes. The largest vesicle contains a gold particle and what could be nanoparticles. The scale bar is 1 μm.
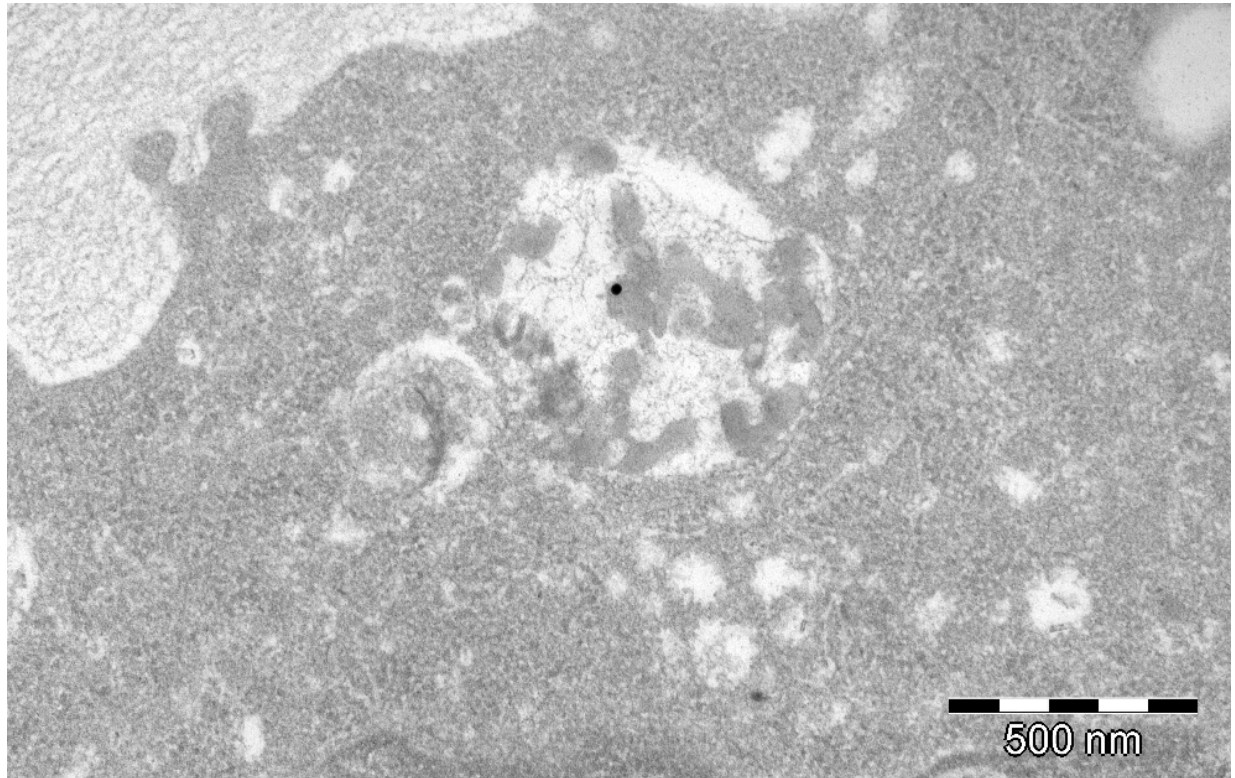
Figure 4.42: A close-up view of the gold-containing vesicle from the previous figure, showing the gold particle and particles or aggregates of sizes around 100-200 nm. The picture is from the DP_{85} (4AM)-treated sample. The scale bar is 500 nm.

4.3.5 Samples treated with gold particles

Pictures obtained from the gold particle-treated samples are shown in Figure 4.43-4.46. Although some gold particles were found inside vesicles, this was a rare observation; most gold particles found were outside the cells, indicating that it was the chitosan-based nanoparticles that were responsible for the cellular uptake of gold. Further, the gold-containing vesicles were usually smaller in size compared to the chitosan-treated samples, around 200-500 nm.
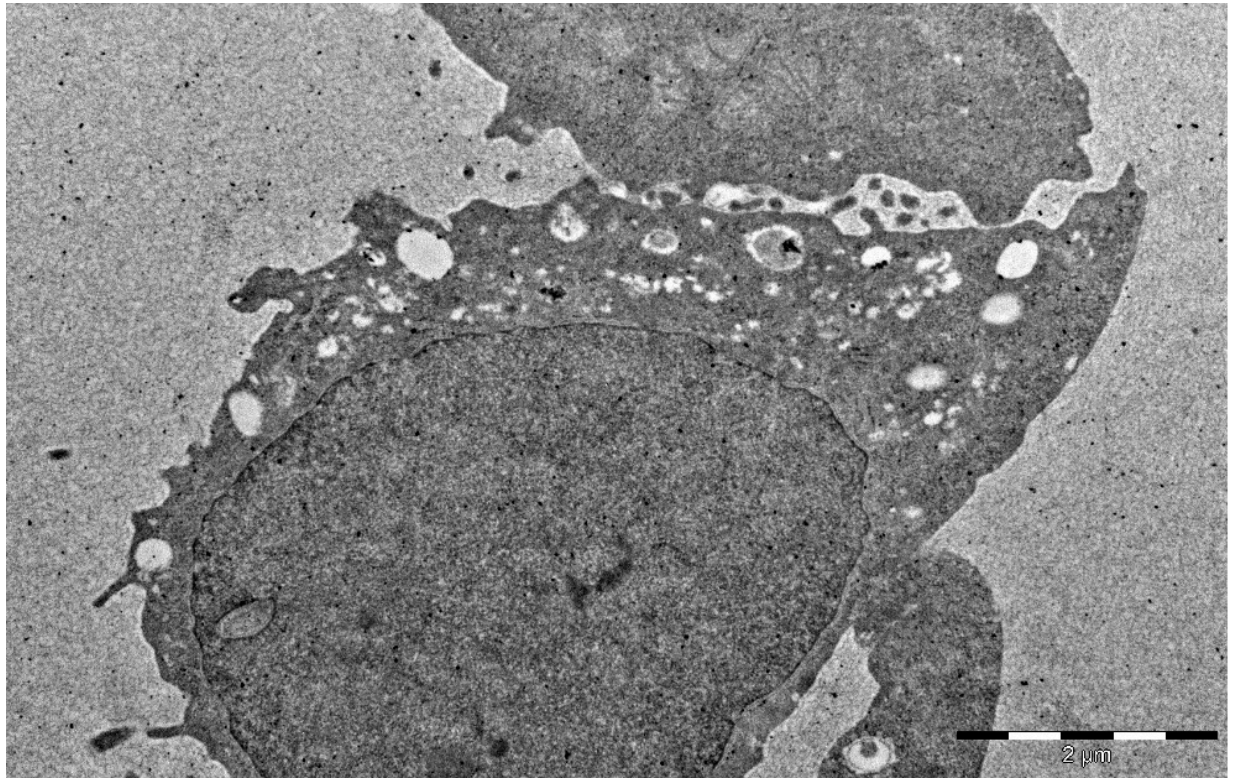
Figure 4.43: An overview of a cell from the gold-treated sample, containing numerous vesicles of different sizes. The scale bar is 2 μm.
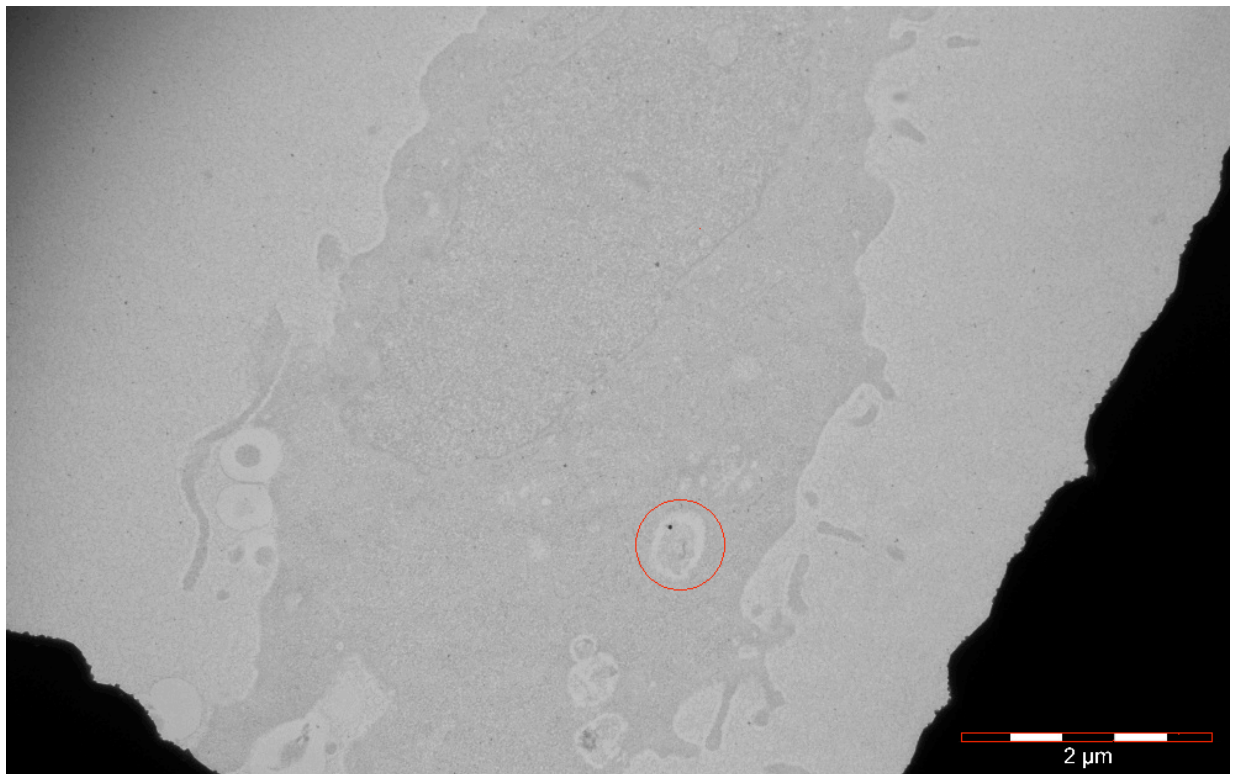
Figure 4.44: A cell from the gold-treated sample with several vesicles, one of them containing a gold particle. The scale bar is 2 μm.
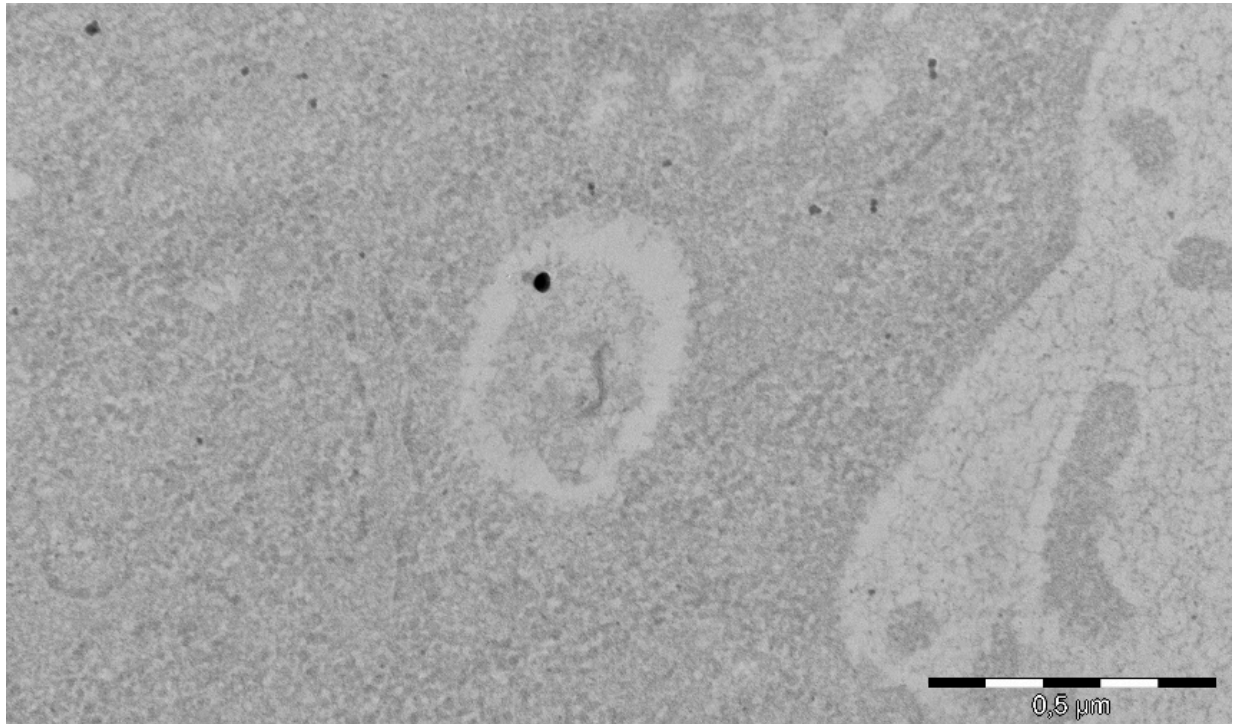
Figure 4.45: A close-up view of the gold-containing vesicle from the previous figure, from the gold-treated sample. The size of the vesicle is around 500 nm, and contains a gold particle and some undefined cargo of about 300-400 nm. The scale bar is 0.5 μm.
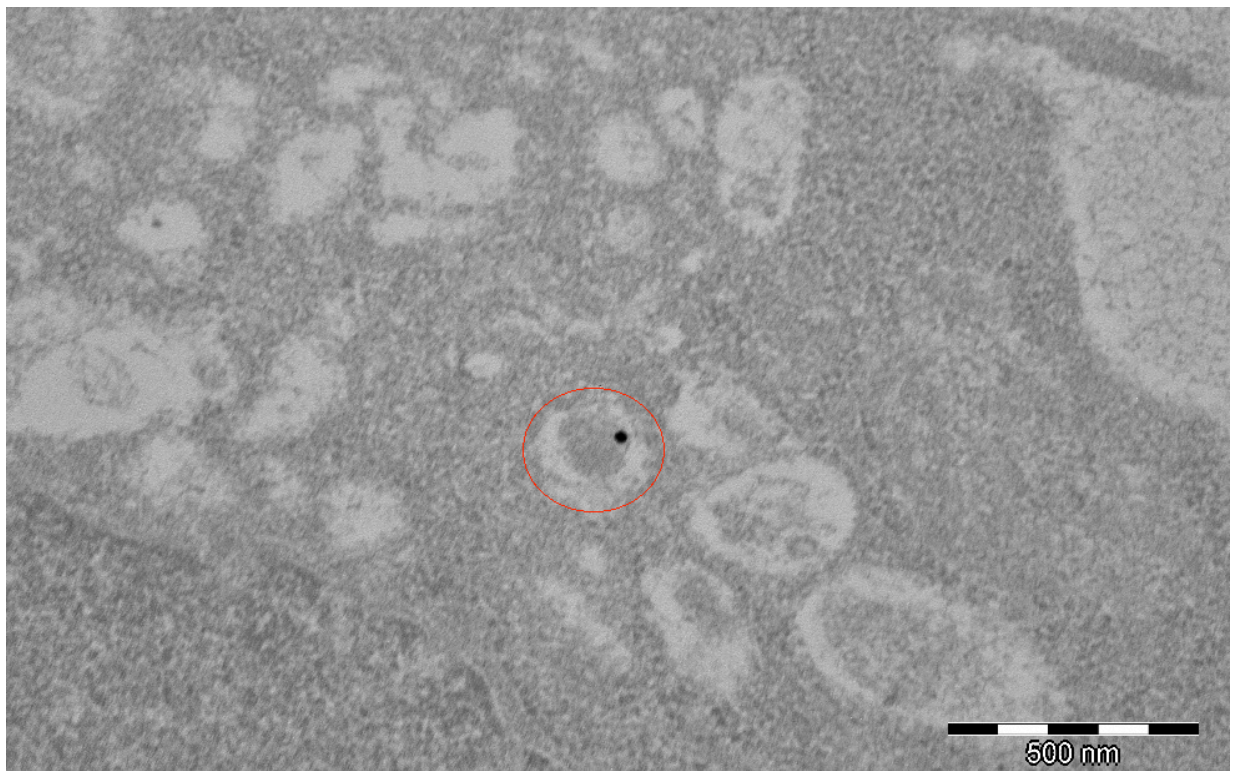
Figure 4.46: A network of vesicles inside a cell from the gold-treated sample, one of them containing a gold particle and some cargo. The size of most of the vesicles is around 200 nm. The scale bar is 500 nm.

4.3.6 Untreated control samples

Untreated cells were also included as control samples, and pictures taken from these samples are presented in Figure 4.47 and 4.48. The cell morphology was about the same as for the other samples, but with smaller vesicles than in the chitosan-treated samples.
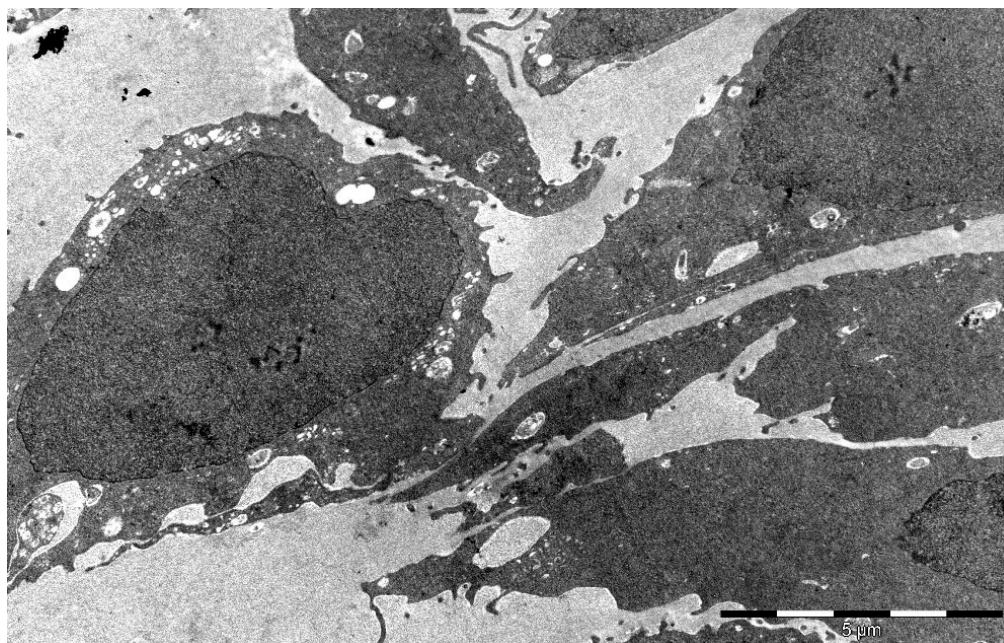
Figure 4.47: An overview of cell morphology from the untreated control sample. Vesicles of different sizes are present close to the cell membranes. The scale bar is 5 µm.
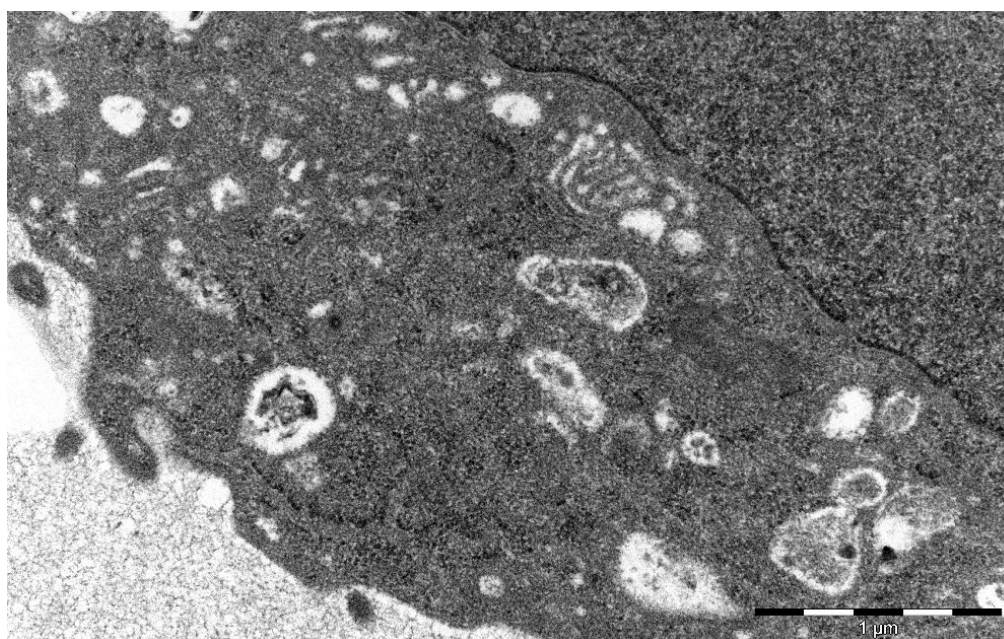
Figure 4.48: A cell from the untreated control sample, with vesicles of various sizes, and with different contents. The intravesicular content seen here is not similar to the content observed in the samples transfected with nanoparticles. The scale bar is 1 µm.

4.4 TEM and STEM characterization of the nanoparticles

In addition to the cell samples, pure solutions of the chitosan-gold-siRNA nanoparticles and a control with only gold particles were analyzed using TEM and scanning TEM (STEM) to investigate their shape and chemical content. The idea was to discover the shape of the nanoparticles in order to be able to identify their presence in the cell samples. However, only the F_a=0 (2% PEG) sample gave meaningful pictures with nanoparticles present.

4.4.1 TEM pictures of pure chitosan-gold-siRNA nanoparticles

Pictures from the sample containing F_a=0 (2% PEG) are shown in Figure 4.49 and 4.50. Both figures show nanoparticles with a size around 100-200 nm, and some of the nanoparticles contain gold particles as well, indicating proper assembly of chitosan-gold-siRNA complexes. In the other samples (LIN350, LIN350 w/HA and DP_{85} (4AM)), the nanoparticles had been degraded, aggregated or were impossible to spot, and the gold particles were found scattered around elsewhere in the sample. Figure 4.51 shows a picture from the sample containing LIN350, with possible LIN350 aggregates and degradation products, but without gold particles.
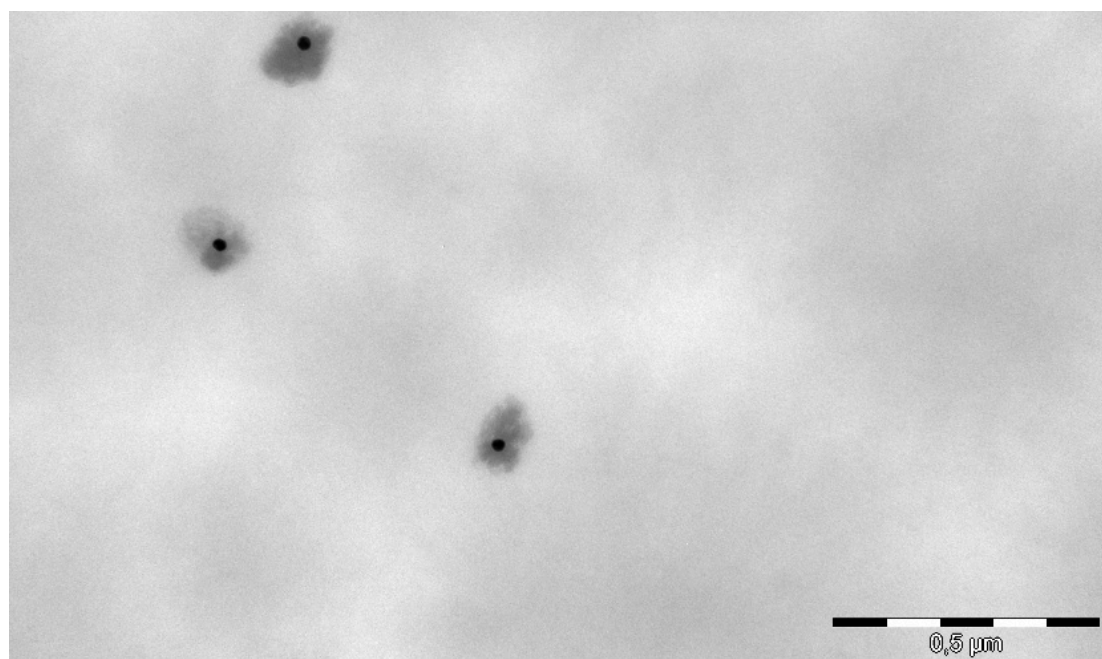
Figure 4.49: Three F_a=0 (2% PEG)-gold-siRNA nanoparticles, with sizes around 100-150 nm. The scale bar is 0.5 μm.
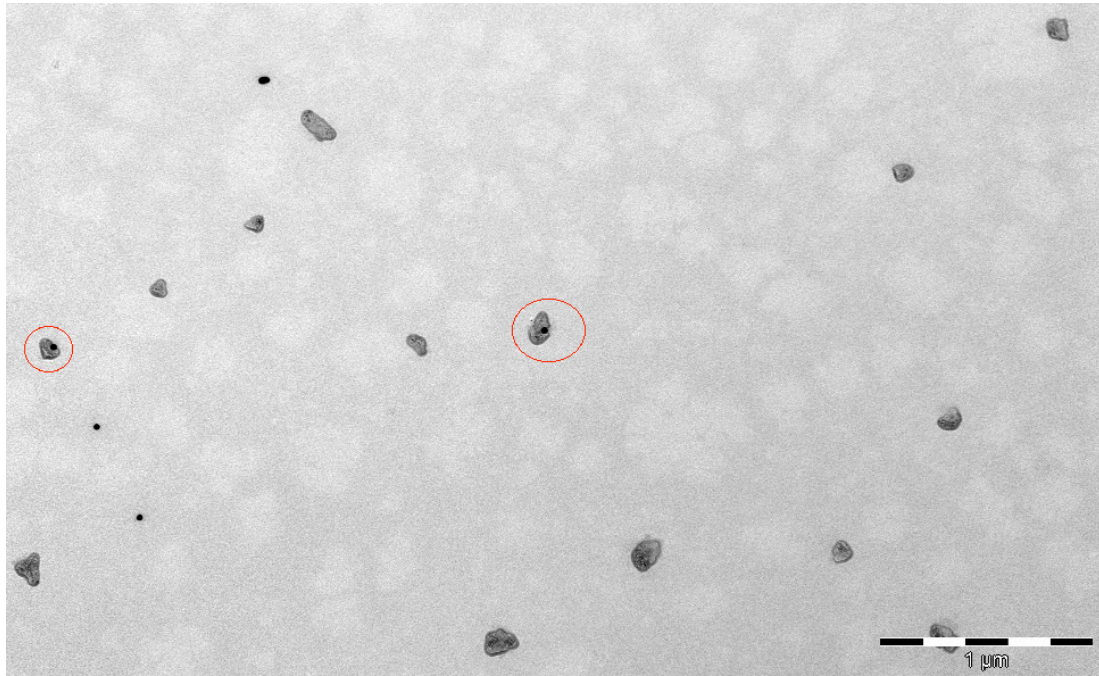
Figure 4.50: A picture from the F_a=0 (2% PEG) sample, showing nanoparticles with sizes around 100-200 nm. Some of the nanoparticles contained gold, as indicated by the red circles, but many did not contain gold, and there were some free gold particles as well. The scale bar is 1 μm.
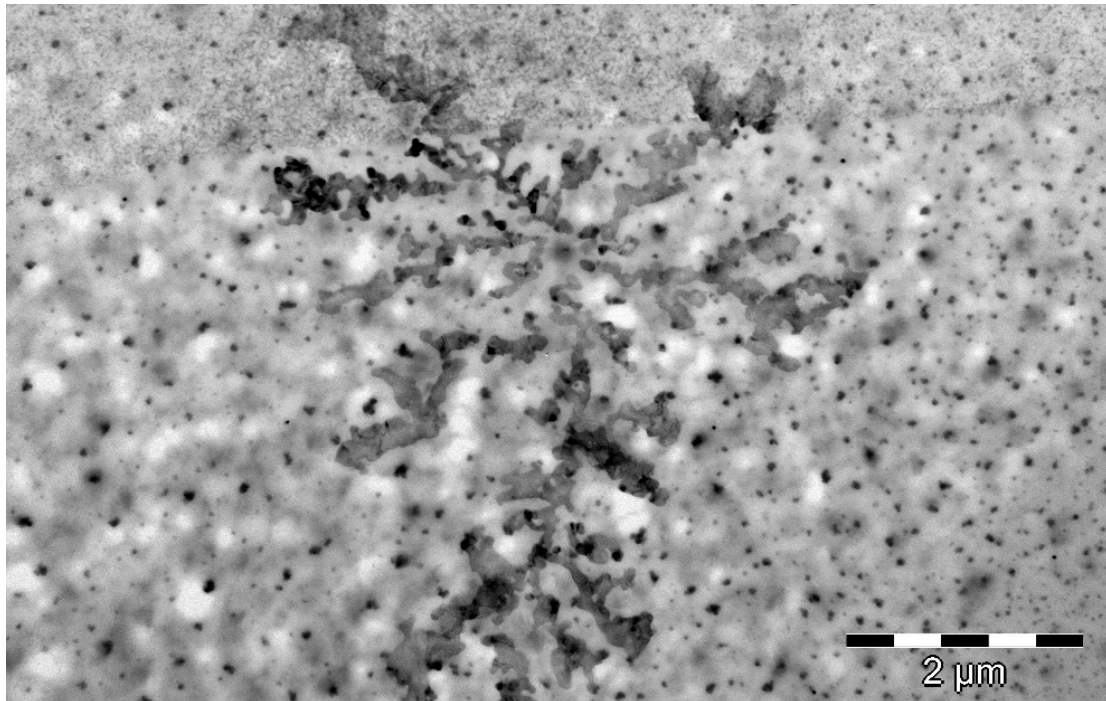
Figure 4.51: A picture from the LIN350 sample, showing possible aggregates and fragments of LIN350 chitosans. The picture does not show signs of gold particles. The scale bar is 2 μm.

4.4.2 STEM characterization of $F_a=0$ (2% PEG)-gold-siRNA nanoparticles and gold

The pure solutions of $F_a=0$ (2% PEG)-gold-siRNA nanoparticles and only gold were analyzed using STEM to discover what elements were present in the samples.

Figure 4.52 shows a picture taken from the gold sample, showing gold particles in a cluster. The left picture is a bright field (BF) image while the right picture is a dark field (DF) image. The graphs show energy levels (keV) of the elements present in the selected areas (given by the red squares). The left graph is from the area with gold particles, and the right graph is from an empty area. Gold particles had aggregated into a large cluster, and the graphs confirmed that the particles consisted of gold. The left graph showed presence of gold (Au), copper (Cu) and carbon I, given by the peaks. In the empty area Au was absent, shown in the right graph. Cu and C were present in both samples due to the copper grid and a thin carbon-based film that covered the samples.
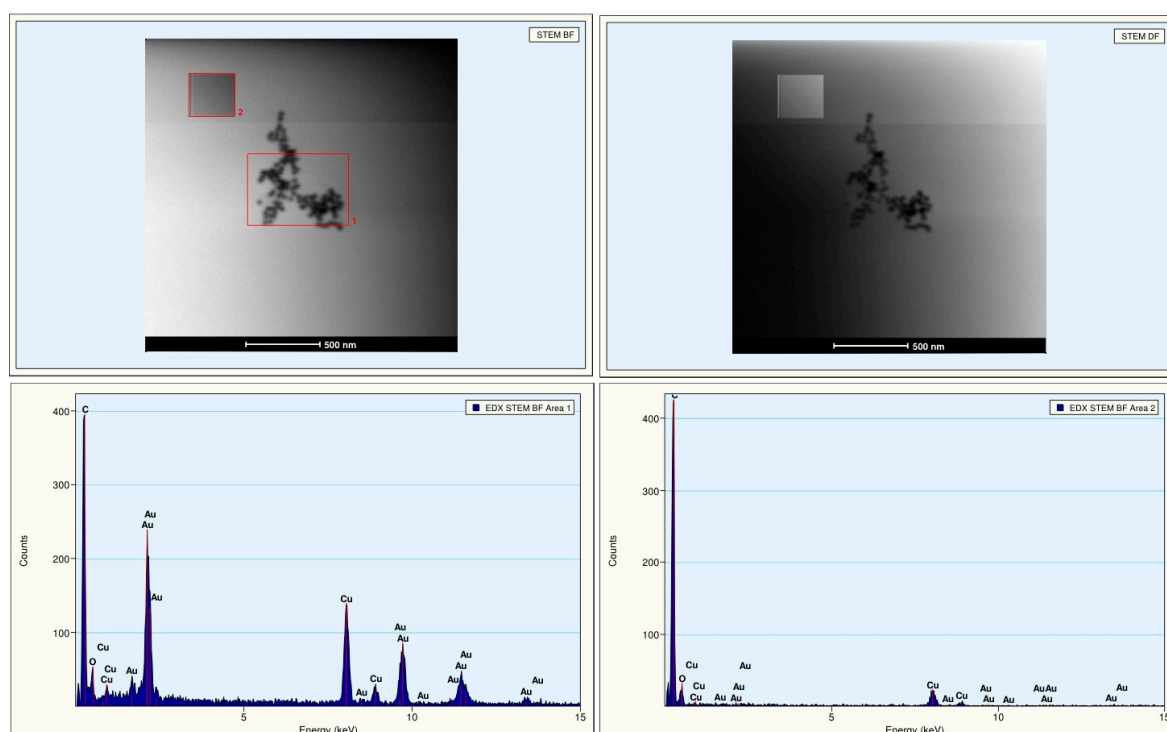
Figure 4.52: STEM analysis of gold particles from the gold control sample. Bright field (BF) and dark field (DF) images were obtained and areas covering gold (left graph) or empty space (right graph) were analyzed for presence of gold. The white reference bars are 500 nm.

Figure 4.53 shows a picture taken from the F_a=0 (2% PEG) sample. The left and right pictures are BF and DF images, respectively, and the graph represents the energy levels of elements from the middle of the chitosan-gold-siRNA nanoparticle (the red dot in the BF image). As the graph shows, carbon I, nitrogen (N), oxygen (O), phosphorus (P) and gold (Au) were all present in the analyzed area, confirming the presence of a nanoparticle in the F_a=0 (2% PEG) sample. The rightmost peak is Cu, while the two other peaks are chloride and calcium, present for unknown reasons. Carbon had a peak of about 2000 keV, and therefore it extends beyond the graph area presented here.
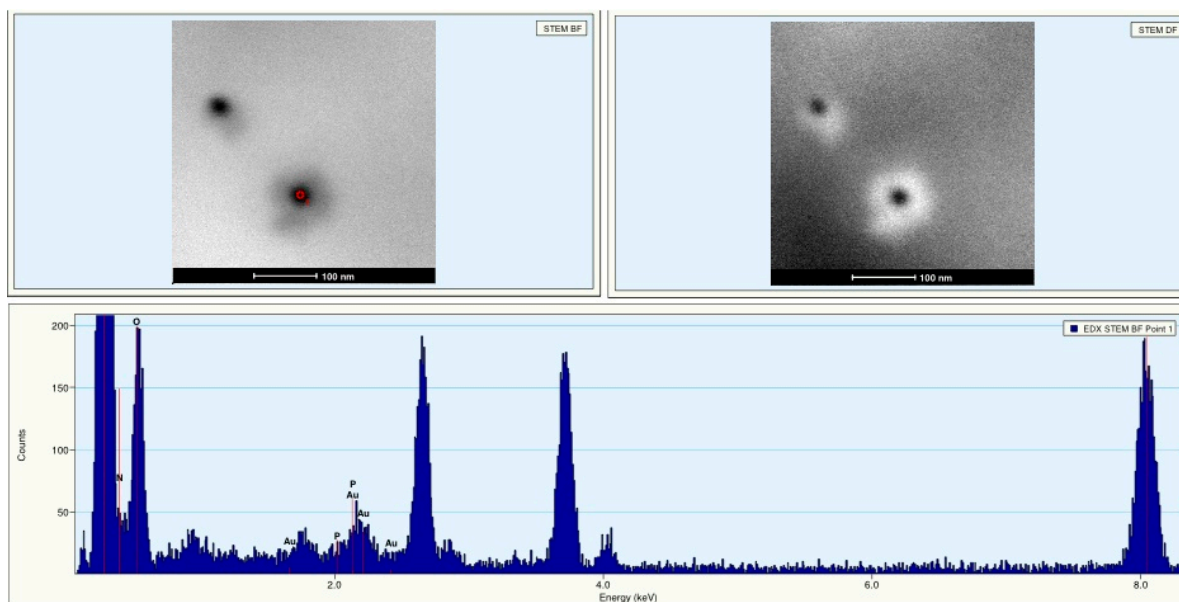
Figure 4.53: STEM analysis of a nanoparticle from the F_a=0 (2% PEG) sample. BF (left) and DF (right) images were taken, and the BF image was analyzed for energy peaks from elements (graph, from the red dot in the BF image). Carbon had a peak of about 2000 keV, and therefore it extends beyond the graph area presented here. The white reference bars are 100 nm.

5. Discussion

5.1 Choice of chitosans

The fully de-N-acetylated chitosans LIN350 and SB300 were selected because of their promising results as siRNA delivery vectors in other cell lines [93, 94, 95]. It has been suggested that siRNA delivery is optimized using fully de-N-acetylated chitosans, mainly because siRNA is a short molecule and requires a high charge density of its counterpart (e.g. chitosan) to form electrostatic interactions and stabilize the nanoparticle [45]. It is also well established that long polymer chains increase the stability, since there will be more charges to stabilize the short siRNA molecule [44]. This is in contrast to chitosans developed for pDNA delivery, since pDNA molecules can be thousands of base pairs long, and can form stable electrostatic interactions with its cationic counterpart even though the polymer chains are shorter and thereby have fewer charges [44]. Longer polymer chains and high charge density therefore seems like a good combination for siRNA delivery. However, there is likely a trade-off between stability and intracellular dissociation of siRNA. If the nanoparticle is too stable, siRNA will not easily dissociate and might be degraded or trapped in lysosomes instead of inducing an RNAi response. This has previously have been shown for the delivery of pDNA-chitosan complexes [37]. In this thesis, all experiments were carried out at physiological conditions (pH 7.2), and since fully de-N-acetylated chitosan has a pK_a around 6.5 not all amino groups will be charged at this pH, which strengthens the need for longer, fully de-N-acetylated polymer chains for chitosan-based siRNA delivery to retain the chitosan charge density.

The chitosans F_a=0 (2% PEG), DP_{85} (4 AM) and LIN350 w/HA were selected because their modifications are reported to improve *in vivo* serum stability of nanoparticles by increasing colloidal stability (resistance to aggregation) and by shielding the nanoparticles from the environment [44, 50, 55].

Because uptake and knockdown efficiencies using chitosan-siRNA nanoparticles has been shown to vary a lot between different cell lines [93, 94, 95], it is therefore difficult to directly compare the results discussed here with other studies.

5.2 The C6 cell line

Chitosan-based siRNA delivery in C6 cells has not been previously described in the literature, and was demonstrated for the first time herein.

5.2.1 N/P ratios and siRNA concentrations

It has previously been shown in several cell lines that cells treated with naked siRNA do not internalize the siRNA (Sabina Strand, unpublished results). As expected, this seems to apply for the C6 cell line as well (Figure 4.1), proving that a delivery vehicle is required for siRNA uptake.
Uptake of Alexa 647 siRNA was first measured using LIN350 and SB300 to optimize the N/P ratio (Figure 4.1A). Both chitosans mediated the highest uptake at N/P 30, with N/P 60 being almost as efficient as N/P 30 for SB300. N/P 10 mediated the lowest uptake for both chitosans, likely due to the lack of chitosan available for sufficient stabilization of the nanoparticle, and possible extracellular dissociation or intracellular degradation of the siRNA. This is in accordance with previous work using linear chitosans finding that chitosan-siRNA nanoparticles at N/P 10 gave low protection of siRNA against RNases due to poor stability, compared to N/P 30 and 60 [96].

However, it is preferable to use as low N/P ratios as possible, since a high dosage of chitosan can increase the chance of unspecific interactions both extra- and intracellularly [45]. Higher N/P ratios are also correlated with increased sizes of the nanoparticles because of the additional chitosan. One study using a linear fully de-N-acetylated chitosan of DP_n 320 and siRNA showed that the z-average size of the nanoparticles increased from 58.4 ± 4.2 nm to 89.3 ± 8.6 nm when comparing N/P 30 to N/P 60. The same study showed only a marginal size-difference between N/P 10 and 30 [45]. It could be that the extra chitosan added from N/P 10 to N/P 30 is utilized for proper complexation of the nanoparticles, whereas from N/P 30 to N/P 60 the nanoparticles are more "saturated" with chitosan, thus at N/P 60 there is an excess of chitosan that will lead to charge repulsions and a large increase in nanoparticle size [45].

An uptake experiment with LIN350, SB300 and RNAiMAX showed that all formulations mediated the highest uptake at a siRNA concentration of 100 nM (Figure 4.1B). The reason for this could be that at higher concentrations there will be more siRNA molecules available for internalization. Further, the increased concentration possibly increased the stability of the nanoparticles. However, it is of interest to use as low concentrations of siRNA as possible, since siRNAs can produce unwanted side-effects in a dose-dependent manner [97]. If the RNAi machinery is

saturated due to too much siRNA, endogenous miRNAs using the same pathways are possibly inhibited, which can be unfavorable. Furthermore, siRNAs have been shown to produce both specific and non-specific immune responses via several pathways, and can also lead to gene silencing if there is a partial complementarity to other mRNAs [97, 98]. One must therefore carefully assess the positive effects of higher siRNA concentrations in regards to knockdown efficiency against the negative effects that can be a consequence of using high doses when deciding which concentration to use. However, the side-effects can be limited by carefully designing the siRNA duplexes after general guidelines [6]. Since higher siRNA doses than 100 nM were not tested, this should be done to evaluate the possible side-effects or benefits of increased siRNA concentrations in this cell line.

From Figure 4.1B it is seen that using RNAiMAX instead of LIN350 or SB300 resulted in much higher uptake of Alexa 647 siRNA in C6 cells, as much as a four-fold higher uptake when comparing the nanoparticles at 100 nM. The reason for this is unclear. The uptake experiments carried out on RBE4 cells (Figure 4.7) showed that LIN350 mediated relatively higher siRNA uptake compared to C6 at identical experimental conditions. When comparing the median FI values between the two cell lines it looks like it was probably not RNAiMAX that gave abnormally good uptake results but rather the chitosans that mediated poor uptake in the C6 cell line. As seen from the TEM experiments from the LIN350-treated sample (Figure 4.15-4.22), the nanoparticles seem to be taken up in large aggregates and it could be that the C6 cells do not efficiently internalize such aggregates. Further, the main difference between the two vectors is that chitosan is a polymer and RNAiMAX is a lipid. While both formulations are cationic, RNAiMAX could associate better with the cell membrane due to its lipophilic properties, which would explain the increased uptake [21].

5.2.2 Knockdown efficiencies using the GAPDH assay

The results presented in Figure 4.2 shows that all three chitosans (LIN350, SB300 and RNAiMAX) mediated efficient knockdown of GAPDH. However, the chitosans with negative control siRNA showed reduction in GAPDH protein activity as well, compared to RNAiMAX with negative control siRNA and the untreated control. This implies that the chitosans had some cytotoxic effects in the C6 cells. The KDalert assay measures protein activity of GAPDH, and it can therefore be suggested that LIN350 and SB300 interfere with some cellular processes and reduce viability and the total protein levels in this cell line. It was somewhat strange that RNAiMAX with negative control siRNA did not give reduced GAPDH protein activity, since this vector has previously been found to be toxic in RBE4 and HEK293 cells [93, 94]. The reason for this is unknown, and other toxicity assays should be carried out to confirm whether the C6 cell line is resistant to RNAiMAX-mediated toxicity or not.

Since the KDalert results from the RBE4 cell line did not show signs of chitosan-induced toxicity (Figure 4.9 and 4.10), it is possible that chitosan may be more cytotoxic to tumor cells than normal cells. Chitosan toxicity specifically against certain tumor cell lines has been reported in the literature. One study using chitosans of different molecular weights showed that low-molecular weight chitosans (50-170 kDa) gave toxic effect in oral carcinoma cell lines but not in the normal control cells [99]. Furthermore, an *in vivo* experiment treating mice with sarcoma and hepatoma using chitosan derivatives showed that chitosan nanoparticles of sizes 40-100 nm gave a significant reduction in tumor sizes [100].

However, no intolerable toxicity has been observed when using similar chitosans to transfect tumor cell lines such as the human lung cancer cell line H1299 [95], but since it is suggested that chitosan-mediated toxicity is cell line specific this could be the reason why different cell lines respond in a different manners. The mechanisms behind the potential antitumor properties of chitosan remain unknown, and more studies are urgently needed to clear this matter out. If proven correct, chitosan´s specific toxicity against certain tumors would indeed serve as a beneficial side effect when using it as a vector for nucleic acid delivery.

5.2.3 P-glycoprotein expression measured using the R123 efflux assay and RT-PCR

The R123 efflux (Figure 4.3) and RT-PCR experiments (Figure 4.6) showed that the C6 cells did not express P-gp in significant amounts in early passage numbers. The slight increase in R123 accumulation in the chitosan-treated cells with or without siRNA indicates that LIN350 and SB300 may modulate or bind to the cell membrane so that more R123 can enter the cells, which also has been suggested in previous studies [94, 96]. If this is the case, it appears that these chitosans only makes it easier for cellular entry but not cellular escape, which might imply reduced expression or direct damage to the P-gp efflux pump itself. Although the C6 cells from px 4 did not contain sufficient amounts of P-gp to confirm this, the same trend was observed at px 19 as well, when the cells were confirmed to express P-gp (Figure 4.5A and 4.6). The flow cytometry was carried out about 2.5 h after R123 had been removed from the medium, and if the chitosans had damaged the cell membranes, some R123 would clearly have ended up back in the growth medium, but this did not seem to be the case as R123 levels were higher than in the untreated control sample. As discussed later on (Section 5.3.3), an increased amount of vesicles due to the internalization of the chitosan-siRNA nanoparticles could give an indirect increase of R123 uptake.

C6 cells that do not express P-gp have been reported in the literature [101], and to attempt to induce expression of this efflux pump the C6 cells were cultured with doxorubicin-containing growth medium. Figure 4.4 shows that it was not the doxorubicin treatment that induced P-gp expression, since R123 levels were comparable between untreated and doxorubicin-treated cells. This was somewhat surprising, since doxorubicin is a P-gp substrate and has been used previously to

induce expression of this efflux pump by gradually increasing its concentration in the growth medium of cultured cells [102]. However, the results can be rationalized from the fact that a very low, steady concentration of doxorubicin was used, and when the comparison was made, all cells were already expressing P-gp, and doxorubicin-treatment therefore seemed unnecessary. R123 efflux experiments were carried out a couple of times between px 4 (no expression of P-gp) and px 19 (P-gp expression). The flow cytometer charts from these in-between experiments show two distinct peaks regarding R123 accumulation, one peak gave low R123 values and the other gave high R123 values, and the peak with high R123 values had disappeared by px 19 (Figure C6, Appendix C). This indicates that the C6 cells gradually started to express P-gp. Either the C6 cell line had some innate properties that made the cells gradually starting to express P-gp after some passages, or the cells simply started to express P-gp because tumor cells are genetically and epigenetically unstable compared to normal cells and can therefore make sudden changes in which genes are expressed or not [78].

The cells had very low levels of R123 accumulation compared to the verapamil-treated cells. This can be explained by the fact that rat P-gp is encoded by two separate genes; *Abcb1a* and *Abcb1b* (also called *mdr1a* and *mdr1b*), creating two isoforms of P-gp. R123 is shown to be a substrate to both isoforms [103]. Furthermore, there is evidence of higher *Abcb1b* than *Abcb1a* mRNA expression in the C6 cell line; it has been shown in a study to express ten-fold higher levels of *Abcb1b* [91]. It should therefore be attempted to transfect the cells with siRNAs targeting both these genes simultaneously to produce a maximum knockdown effect. However, RBE4 cells have also been found to express substantially more *Abcb1b* than *Abcb1a* mRNA [104], and knockdown of *Abcb1b* in this cell line did not have any effect on P-gp function, although this could be due to the siRNA design (Jostein Malmo, unpublished results). Therefore it might seem strange that P-gp knockdown in these cells was more efficient than in C6 cells (Figure 4.11-4.13), but it became evident throughout the experiments from both cell lines that transfection efficiencies change over time, and it is thus difficult to compare results from different passage numbers. Ultimately, the RT-PCR experiments showed that the RBE4 cells expressed about four times as much *Abcb1a* mRNA as the C6 cells and this probably explains why P-gp silencing was more efficient in this cell line. More mRNA present in the cytosol will most likely give a higher chance for the siRNA-RISC complexes to find and degrade their target, and thus a relatively higher knockdown can be achieved compared to the untreated control, as seen for the RBE4 cells (Figure 4.11-4.13). However, it is contradicting that the RBE4 cells transfected with anti-Abcb1a siRNA had higher intracellular levels of R123 compared to the C6 cells, as there was four times more Abcb1a mRNA and therefore should be a higher amount of P-gp efflux pumps as well. This can again be explained by the presence of more Abcb1b mRNA in the C6 cells. If the P-gp knockdown is optimized, it seems likely that the C6 cells have the potential to be co-cultured in a glioma-BBB model along with RBE4 cells.

5.3 The RBE4 cell line

5.3.1 Uptake kinetics of Alexa 647 siRNA

The uptake kinetics experiment (Figure 4.8) showed that the intracellular levels of Alexa 647 siRNA rapidly decreased over time in the RBE4 cells for both nanoparticle formulations (LIN350 and SB300), and after 48 h the siRNA levels were comparable to the untreated control. There are two likely reasons for this: intracellular RNases degrade siRNA, and the siRNA is diluted due to cell division [11]. This experiment was carried out on actively dividing RBE4 cells. If used as an *in vitro* BBB model, the RBE4 cells should be confluent in order to mimic the *in vivo* situation. Therefore, another similar experiment but with confluent cells should be attempted, in order to reduce the impact of the dilution effect caused by cell division.

5.3.2 Knockdown of GAPDH using confluent cells

From Figure 4.10 it is clear that confluent RBE4 cells were easy to transfect; all nanoparticles at both concentrations (except LIN350 at 50 nM and N/P 10) mediated efficient reduction in GAPDH protein activity comparable to non-confluent cells, suggesting that this cell line is suitable for transfection studies by implementation in an *in vitro* transwell model of the BBB. The N/P 10 formulation with a 50 nM siRNA concentration did not mediate any GAPDH reduction, probably due to unstable nanoparticles. This was not apparent for N/P 10 at 100 nM, where there was a strong reduction in GAPDH protein activity, and this implies that an increase in siRNA concentration alone can be sufficient for nanoparticle stabilization, independent of increasing the N/P.

5.3.3 P-glycoprotein knockdown: kinetics and optimization

The results presented in Figure 4.11 showed that LIN350 gave a much higher absolute R123 value of median FI than SB300 at 48 h, but that they had similar values after 96 h. Since the R123 levels in the SB300-transfected cells did not change from 48 to 96 h, this might suggest that the siRNA is released more slowly from the SB300-siRNA nanoparticles, resulting in lower maximum P-gp knockdown, but with a steadier release of siRNA. However, since the difference between LIN350 and SB300 at 96 h was only slight it is difficult to conclude, and a longer knockdown experiment including measurements after 120 h should be carried out to elucidate this matter. Furthermore, the median FI values observed for LIN350 at 48 h were lower in the other P-gp experiments at similar experimental conditions (Figure 4.12 and 4.13). Since all P-gp knockdown experiments were carried out at different passage numbers, it seems evident that the transfection efficiency changes over time in RBE4 cells. This

could be because the P-gp expression varies from passage to passage, as previously shown [105].

The kinetics experiment (Figure 4.12) showed that repeated administration of nanoparticles resulted in prolonged RNAi. The effect was most evident when transfecting the cells three times (T3). After 7,500 cells were seeded in each well, the cells appeared to grow confluent after about four days. Since the third transfection was carried out four days after seeding the cells, the intracellular siRNA concentration in the T3 sample would therefore be less diluted compared to the other samples, due to a decreased growth rate, and this could explain the prolonged effect that was observed. However, the R123 levels continued to drop even after the cells were confluent, which suggests that both cell division and intracellular degradation of siRNA are responsible for the reduced RNAi observed over time. For future experiments, it should be attempted to use confluent cells from the beginning to better understand the relationship between the two mechanisms causing the loss of siRNA.

Furthermore, the kinetics experiment showed low P-gp knockdown efficiencies after 44 h (day 2). This was surprising since the previous experiment (Figure 4.11) provided high knockdown efficiencies after 48 h. It was later confirmed that the highest P-gp knockdown from LIN350-siRNA nanoparticles was after 72 h rather than 48 h (Figure 4.13), but the same experiment gave an efficient knockdown after 48 h as well. Since the delayed P-gp knockdown only occurred in the kinetics experiment, it is difficult to tell the reason for this. It was first hypothesized that the too-early measurement (after 44 h instead of 48 h) could be the reason, but this was rejected by the R123 efflux experiment presented in Figure 4.13, which gave similar absolute values of median FI after 43, 48 and 53 h.

All P-gp knockdown experiments carried out in the RBE4 cell line gave increased R123 levels for the LIN350 and SB300 samples with negative control siRNA compared to the untreated control, similar as for the C6 cell line. The trend was especially evident for LIN350. Since the chitosans with colloidal stability did not show this pattern for their negative control siRNA samples, it is probable that the modifications of these chitosans prevent potential damage caused by chitosan. The TEM pictures from the LIN350-treated samples (Figure 4.15-4.22) show that many cells had large leaky vesicle networks close to the cell membrane, and the extra R123 could have been internalized by exploiting these pathways.

5.3.4 Screening of chitosans with improved colloidal stability

5.3.4.1 F_a=0 (2% PEG)

PEGylation of chitosans for gene delivery has been shown to improve serum stability, decrease inter-particular aggregation and increase the transfection efficiency of several cell lines. However, most studies using PEGylated chitosan has focused on pDNA delivery, and other formulations might be needed for siRNA delivery for reasons already discussed. F_a=0 (2% PEG) mediated high uptake of Alexa 647 at both N/P 10 and 30. Surprisingly, the highest uptake was observed at N/P 10. F_a=0 (2% PEG) is a linear, fully de-N-acetylated chitosan and has a DP_n of 365, and is similar to LIN350 except for the PEGylation. Since LIN350 facilitated highest uptake at N/P 30 (Figure 4.1 and 4.7), it can be suggested that PEGylation stabilizes the nanoparticles to a high extent and that the effect of the N/P on uptake becomes negligible when comparing N/P 10 and 30.

In spite of good uptake, the F_a=0 (2% PEG)-based nanoparticles failed to mediate efficient RNAi in the RBE4 cells. There can be several reasons for this. If the nanoparticles become too stable they might not dissociate properly intracellularly, thus the siRNA will not be released from the endosomes and might end up being degraded or trapped in the lysosomes [25]. The TEM experiments suggested that the LIN350-siRNA nanoparticles - which mediated efficient RNAi in the RBE4 cell line - were taken up in large aggregates and filled the vesicles that they were internalized into (Figure 4.15-4.22). A gradual degradation of the chitosan chains inside the vesicle can lead to osmotic swelling due to the increased amount of oligo- and monosaccharides present [64, 65], and this could be the case with LIN350. Since F_a=0 (2% PEG)-siRNA nanoparticles are thought to have increased colloidal stability, they might be internalized more separately and thus produce a weaker osmotic swelling effect.

Transfection efficiencies using PEGylated chitosans for siRNA delivery have previously been found to negatively correlate with increasing amount of PEG in HEK293 cells [106]. It was found that the formulations with 5% PEG gave lower transfection efficiencies (both uptake and knockdown) than formulations without PEG or with 1% PEG. This was explained by the ability of PEG to shield the positive charges of chitosan, thus giving weaker complexation with siRNA and unstable nanoparticles. This does not seem to be the case with F_a=0 (2% PEG) in RBE4 cells, as uptake was higher than for LIN350. A formulation with PEGylated chitosans of lower DP_n could be of interest to produce nanoparticles with good serum-stability but with less intracellular stability due to fewer charges on the chitosan chain. This could enable an osmotic swelling of the endosomes, leading to increased release of siRNA into the cytoplasm.

5.3.4.2 DP$_{85}$ (4AM)

DP$_{85}$ (4AM) showed highly efficient uptake at N/P 30, and at N/P 10 the uptake was fairly efficient, similar to the linear chitosans. It is expected that the pentamer GlcNAc-GlcNAc-GlcNAc-GlcNAc-2,5 anhydro-mannofuranose (4AM) increases uptake of nanoparticles since mannofuranose – a mannose isomer – may associate with widely distributed cell-membrane lectins and thus facilitate endocytosis [51]. In addition to improved transfection rates, substitution of chitosan with AAM trimers has previously been shown to increase colloidal stability and does not increase the size of the nanoparticle to a large extent because the uncharged trimers are branched off the main polymer chain. Thus, the hydrodynamic volume will not increase significantly [50]. This is expected also to apply for the 4AM substitutions.

Since 4AM is not a charged molecule, it does not contribute to association between chitosan and siRNA, and could in fact reduce the availability of electrostatic interactions between the two due to steric hindrances [94]. This may explain why the N/P 10 formulation of DP$_{85}$ (4AM) was internalized at lower levels compared to N/P 30. DP$_{85}$ (4AM) has a number-average degree of polymerization of 85, and as previously discussed this is a relatively short chain length for siRNA delivery. At N/P 10 this might not be sufficient to provide stable complexation with the siRNA, resulting is extracellular dissociation and reduced uptake of the nanoparticle, which did not seem to be the case at N/P 30.

Although high uptake was observed for DP$_{85}$ (4AM), the knockdown experiments did not give promising results. As discussed earlier, chitosan-based siRNA delivery is suggested - at least to some extent - to be dependent on intravesicular degradation of the polymer chain to produce osmotic swelling and siRNA release. The TEM pictures from the DP$_{85}$ (4AM)-treated sample showed that the nanoparticles were taken up in large vesicles, but unlike the LIN350-treated sample, there were fewer nanoparticles in the vesicles, which most likely prevented sufficient osmotic swelling to occur. This can be explained by the increased colloidal stability by DP$_{85}$ (4AM) at N/P 30; since the nanoparticles did not form aggregates, they were not internalized together either.

5.3.4.3 Chitosans coated with Hyaluronic acid

LIN250 w/HA and LIN350 w/HA did not give efficient uptake of the Alexa 647 siRNA at neither N/P 10 nor N/P 30, compared to the other chitosans. Hyaluronic acid (HA) is an anionic polymer that is biocompatible, biodegradable and mucoadhesive, and the main purpose of using this molecule was to reduce the cationic surface charge of the nanoparticles for the possibility of increasing colloidal stability. Further, when used for nucleic acid delivery HA may enhance the uptake efficiency of the nanoparticle through interaction with the CD44 receptor, which is often present in the cell membranes of various cell types, including RBE4 cells [55]. However, the

relatively low uptake observed using HA-coated nanoparticles in this study suggests that the CD44 receptors did not efficiently internalize the nanoparticles. Since the HA was added to the nanoparticles in a 3:1 charge ratio against chitosan amino groups, there is likely that there was an excess of HA present, and that these free HA molecules bound the CD44 receptors and prevented nanoparticle-CD44 association. Reducing the charge ratio between HA and chitosan could therefore be a way to improve the uptake efficiency.

In accordance to the relatively low uptake, LIN250 w/HA and LIN350 w/HA did not mediate RNAi. The TEM pictures of the LIN350 w/HA sample (Figure 4.23-4.28) revealed nanoparticle-like structures inside large vesicles around 0.5-1 μm. If these intravesicular structures were indeed nanoparticles, it is somewhat strange that they did not provide an RNAi response, since many of the vesicles seemed to be filled with nanoparticles (see particularly Figure 4.26 and 4.27) and should be releasing their content according to the theories previously discussed. It seems like the addition of HA makes the nanoparticles more resistant to intracellular dissociation, which was to some extent confirmed with TEM, since the nanoparticles looked intact inside the vesicles in contrast to the LIN350 sample where they seemed to have dissociated. It is therefore likely that the nanoparticles followed the endosomal pathway and were subsequently degraded in the lysosome or trapped and diluted after multiple cell divisions.

5.3.4.4 Unmodified linear and self-branched chitosans

LIN250, LIN350 in addition to SB300 chitosans showed intermediate efficiency regarding Alexa 647 uptake in RBE4 cells compared to the other formulations used. Nevertheless, these were also the only formulations that successfully mediated RNAi (Figure 4.9 and 4.11). The experiments carried out with these chitosans show that they are able to efficiently transfect RBE4 cells, although SB300 mediated lower P-gp knockdown than LIN350 in spite of a slightly higher siRNA uptake (Figure 4.8), and one should continue to use them for further experiments. However, they are most likely best suited for *in vitro* experiments, since they are insufficiently stable in blood serum due to reasons already discussed (inter-particular aggregation, low solubility etc.). Therefore, the search for serum-stable chitosan formulations with increased colloidal stability and good shielding properties for the *in vivo* environment should continue, with the goal of finding the proper balance between serum stability and intracellular dissociation.

5.3.4.5 Obstacles during the TEM experiments

The results from the TEM experiments presented in Figure 4.14-4.48 showed that very few gold particles were present in the RBE4 cells inspected by TEM, compared to the initial number. Since the concentration of gold particles was $2.5 \cdot 10^8$/mL, more than one billion gold particles should be present in each sample prior to the TEM preparations since 4.3 mL nanoparticle solution was used for each. There were approximately 6 millions cells in each sample, and if all gold particles were taken up by the cells this mean there should be 100-200 gold particles in every cell. There are several reasons for the low number of gold particles observed. Obviously, not all gold particles were taken up because they were highly dependent on chitosan-siRNA nanoparticles for internalization as seen from the gold-only control sample, which showed minimal presence of intracellular gold. As previously discussed, the nanoparticles used for the TEM experiments (LIN350, LIN350 w/HA, F_a=0 (2% PEG) and DP_{85} (4 AM)) showed different degrees of cellular uptake in the RBE4 cell line, and this indicates that a portion of the nanoparticles are not internalized, and it could also be that the gold particles interfered with either nanoparticle complexation or cellular uptake. Furthermore, much of the gold was probably lost during the TEM preparations. The cell samples went through a number of preparation steps, and it is probable that some gold was lost during the process. Only a small piece of each cell sample was added onto the copper grid, and since the samples were sliced into 70 nm thick pieces, this means that most of the cell volume was not included in the sample, and most likely this contributed to the reduced number of gold particles observed.

The TEM results from the pure nanoparticle solutions showed that only the PEGylated nanoparticles (F_a=0 (2% PEG) were still assembled when investigated, while the other formulations gave no meaningful pictures. This is probably due to the preparation of the samples; a few μL of solution was put on a copper grid and dried over night without fixation. The electrostatic interactions between chitosan and siRNA are crucial for complexation of the nanoparticles, and since the charge of the chitosan amino groups is pH dependent, they are probably dependent on being in solution to associate with siRNA, and thus the drying process could have made the nanoparticles dissociate. It seems that the PEGylation protected the nanoparticle from this dissociation.

The TEM pictures of F_a=0 (2% PEG)-based nanoparticles (Figure 4.49 and 4.50) showed that if bound to gold, there is only one gold particle for every nanoparticle, and some nanoparticles had not associated with gold at all. The nanoparticles were compared with structures from the cell samples, and some similarities were found, which strengthens the suggestion that it was in fact nanoparticles that were observed in the cell samples. Although only the PEGylated nanoparticles were characterized, it is fair to assume that the other formulations had similar shapes and sizes.

5.4 Uptake mechanisms and intracellular trafficking

Although the TEM pictures from the cell samples revealed patterns of different shapes and structures for each of the nanoparticles used, the results show that all of the nanoparticle-treated samples had presence of gold particles internalized in large vesicles, ranging from 0.5-several μm.

This indicated that clathrin-mediated and caveolae-mediated endocytosis mechanisms are probably not the main pathways utilized for internalization of these nanoparticles, since these pathways are reported to internalize their cargo in vesicles smaller than 120 and 500 nm, respectively [27, 62]. This also seems to be in accordance with previous findings, where inhibitors of clathrin- and caveolae-mediated endocytosis did not give significant reduction in uptake or knockdown efficiencies for various chitosan-siRNA nanoparticles similar to the ones used herein [94, 106]. However, one must be careful to compare results from one chitosan formulation to another, since small modifications can change the characteristics, and thus the uptake, of the nanoparticle. Nevertheless, similarities in behavior are expected for different formulations, especially for unmodified chitosans.

Macropinocytosis seems like a possible route utilized by the nanoparticles in this study as this mechanism creates large vesicles up to several μm [27]. Although it was previously thought that this pathway was limited to the uptake of extracellular fluids and large particles such as bacteria [59], there is evidence that different nanoparticles, including hydrophobically modified chitosan nanoparticles, utilize macropinocytosis [58, 61, 107]. Since macropinosomes are large, and chitosan has poor buffering capacity, the nanoparticles should be taken up in large aggregates in order to destroy the vesicle to be released intracellularly and be able to carry out siRNA-mediated RNAi. This seems to be the case for the LIN350 nanoparticles, but from the knockdown experiments and the TEM results it does not seem to be the case for the other chitosans investigated herein. It is therefore likely that the nanoparticles with these chitosans travel along with the macropinosomes and end up being degraded in the lysosome. Further, macropinosomes have previously been reported to utilize transcytosis; a mechanism used for transporting the intravesicular cargo out to the extracellular environment on the other side of the cell [60]. Transcytosis has also been reported for PEGylated nanoparticles using clathrin-mediated endocytosis [108], and could be a possible *in vivo* route for the chitosans investigated in this study.

If proven correct, transcytosis of the chitosan-based nanoparticles could be advantageous for *in vivo* delivery across the BBB. Further, current nucleic acid delivery systems often show limited efficiency in deeply penetrating their target tissues such as solid tumors [25], thus transcytosis could improve the delivery as the nanoparticles would travel through the outer cell layers and be distributed into the tissue.

Another study investigated the intracellular trafficking of HA taken up via the CD44 receptor in keratinocytes [109]. This study found that inhibitors of clathrin- and

caveolae-mediated endocytosis and macropinocytosis failed to reduce the uptake of HA. Since the HA in the study was found in vesicles predominantly larger than 1 μm, it was suggested that another unknown pathway is responsible for HA uptake and trafficking, which is not macropinocytosis or phagocytosis. It was further hypothesized that most of the HA ended up for degradation in the lysosomes, which may explain the low transfection efficiencies of HA-coated nanoparticles seen in our study.

The results from the TEM experiments seem to clarify some of the unanswered questions behind the intracellular faith of chitosan-siRNA nanoparticles, since it appears that most formulations utilize macropinocytosis for uptake, possibly with LIN350 w/HA as an exception. It should therefore be attempted to inhibit this pathway by using a macropinocytosis inhibitor to confirm if this is true.

In this thesis it was shown that there seems to be a trade-off between stability and knockdown efficiency for chitosan-based siRNA delivery *in vitro*. While chitosans such as LIN350 seem to have high transfection efficiencies because they mediate osmotic swelling by filling the intracellular vesicles and dissociate, this does not seem to be the case with the colloidally stable chitosans. Although several successful chitosans have elsewhere been developed for pDNA delivery *in vivo*, siRNA delivery *in vivo* is still hampered by the fact that the siRNA molecules require longer chitosan chains for stabilization, with larger nanoparticles as a result. If these nanoparticles are internalized into large vesicles and have modifications that prevent aggregation such as the ones investigated herein, they might not induce osmosis and subsequent RNAi unless the vesicles are filled with nanoparticles and with a subsequent dissociation of the complexes. Therefore, it might be that completely new chitosan formulations have to be developed. These novel formulations should preferably utilize other internalization pathways than macropinocytosis that do not need large quantities of nanoparticles in each vesicle for efficient transfection, for example caveolae-mediated endocytosis, which creates smaller endosomes that do not fuse with lysosomes. However, it might be that minor modifications to the already existing formulations can increase knockdown efficiencies as well, for example by deceasing or increasing the DP_n slightly. This should be attempted before any major changes are initiated.

Furthermore, is also clear that if the nanoparticles are too big, they will have more obstacles in *in vivo* delivery [25]. Molecules such as HA can greatly increase the size of the nanoparticle [96], which stresses the need for modifications that do not contribute much to the overall size, for example 4AM.

6. Future studies

The results obtained in this thesis encourage further investigation of the C6 and RBE4 cell lines for an implementation in an *in vitro* glioma-BBB model, using transwells for co-culturing of these cell lines. To develop such a model, RBE4 cells could be grown confluent on the apical side of the transwell filter and C6 cells on the basolateral side or on the bottom of the well. To mimic the *in vivo* situation, the tight junctions of the RBE4 monolayer must be properly tight to prevent paracellular transport. To measure the tightness of the monolayer one could add Lucifer yellow, which is a fluorescent dye developed for such purposes [110], to the apical side of the transwell and measure the migration of the dye to the basolateral side. It is important to measure this both before and after transfection, since chitosans have been shown to modulate tight junctions *in vivo* [111]. The model could then be tested by silencing the P-gp expression in the RBE4 cells and add a P-gp substrate such as doxorubicin to the apical side, and see if the C6 cells eventually internalize this molecule.

If successfully developed, the transwell model will prove important for transfection studies of the BBB *in vitro*. Additionally, this model could confirm if the chitosan-based nanoparticles are transcytosed across the endothelial monolayer. If nanoparticles with Alexa 647 siRNA are added to the apical side of the confluent RBE4 cells, the C6 cells should internalize some of the nanoparticles if transcytosis has occurred.

When attempting to silence the P-gp efflux pump, both *Abcb1a* and *Abcb1b* mRNAs should be targeted in the C6 cells to get an improved knockdown effect. In addition, the toxicity indicated by the chitosans in the C6 cell line needs to be further investigated, for example by using the MTT or Alamar Blue viability assays.

As for the intracellular trafficking utilized by the nanoparticles, inhibition of macropinocytosis should be attempted using for example cytochalasin D or amiloride, to see if this influences transfection efficiencies by the chitosan-siRNA nanoparticles.

The chitosans with colloidal stability could be optimized in different ways.
F_a=0 (2% PEG) could be modified by decreasing the DP_n slightly, with the goal of keeping the stability but increasing the intracellular dissociation due to fewer electrostatic interactions between chitosan and siRNA.
For DP_{85} (4AM) it should be developed formulations with different degrees of substitution (d.s.) for the 4AM molecule. The chitosan used herein had a d.s. of 8 %, and it could be either increasing or decreasing the d.s. could improve transfection efficiencies, possibly in combination with changing the DP_n slightly.
When using HA to modify chitosans, it should be attempted to use a lower ratio between HA and chitosan to reduce the effect of the excess HA molecules on nanoparticle uptake.

7. Conclusion

The transfection efficiencies were similar for LIN350 and SB300 in the C6 cell line but SB300 seemed to be more cytotoxic than LIN350. LIN350 had superior transfection efficiency in the RBE4 cell line. Both formulations mediated the highest efficiency at N/P 30 and at a siRNA concentration of 100 nM. However, a further optimization of the P-gp knockdown experiments in C6 cells is needed to improve the efficiency. The transfectability of the confluent RBE4 and the C6 cells implies that these cell lines have the potential to be implemented in a transwell glioma-BBB model for P-gp transfection experiments mimicking *in vivo* conditions.

Macropinocytosis seems to be a major intracellular trafficking route utilized by the chitosan-siRNA nanoparticles investigated herein. The chitosans with improved colloidal stability did not mediate knockdown, possibly because they did not completely fill the macropinosomes, which are large and may require a large amount of nanoparticles to burst. New formulations should therefore be developed, preferably with small sizes and targeting another endocytosis route than macropinocytosis, with the goal of mediating efficient RNAi *in vivo*.

References

1. Fire, A., Xu S., Montgomery M., Kostas S., Driver S. and Mello C., *Potent and specific genetic interference by double-stranded RNA in Caenorhabditis elegans*, Nature, 1998. **391**: 806-811.

2. Nobelprice.org, The Official website of the Nobel Prize (Online), *The Nobel Prize in Physiology or Medicine 2006,* 2006
    Available from:
    http://www.nobelprize.org/nobel_prizes/medicine/laureates/2006/
    (Downloaded November 20, 2011).

3. Paddison, P., Caudy A., Bernstein E., Hannon G.J. and Conklin D., *Short hairpin RNAs (shRNAs) induce sequence-specific silencing in mammalian cells*, Genes Dev., 2002. **16**(8): 948–958.

4. Meenakshisundaram, K., Carmen L., Michela B., Diego D.B., Rosaria V and Gabriella M., *Existence of snoRNA, microRNA, piRNA characteristics in a novel non-coding RNA: x-ncRNA and its biological implication in Homo sapiens,* J.Bioinform. Seq. Anal, 2009. **1**(2): 031-040.

5. Invivogen (Online), *RNA interference review*. Last modified 2011.
    Available from: http://www.invivogen.com/review-rna-interference
    (Downloaded February 3, 2012).

6. Castanotto D. and Rossi J., *The promises and pitfalls of RNA-interference-based therapeutics,* Nature, 2009. **457**: 426-433.

7. Carthew R. and Sontheimer E., *Origins and Mechanisms of miRNAs and siRNAs*, Cell, 2009. **136**(4): 642-655.

8. Tomari Y. and Zamore P., *Perspective: Machines for RNAi*, Genes Dev., 2005. **19:** 517-529.

9. Pillai R., Bhattacharyya S., Filipowicz W., *Repression of protein synthesis by miRNAs: how many mechanisms?,* Trends Cell Biol., 2007. **17**(3): 118-126.

10. Lim L. et al, *Microarray analysis shows that some microRNAs downregulate large numbers of target mRNAs*, Nature, 2005. **433**: 769-773.

11. Whitehead K., Langer R. and Anderson D., *Knocking down barrier: Advances in siRNA delivery,* Nat. Rev. Drug Discovery, 2009. **8:** 129-138.

12. Bartlett D. and David M., *Insights into the kinetics of siRNA-mediated gene silencing from live-cell and live-animal bioluminescent imaging*, Nucleic Acids Res. 2005, **34**(1): 322-333.

13. Haley B. and Zamore P., *Kinetic analysis of the RNAi enzyme complex,* Nat. Stuct. Mol. Biol., 2004, **11**: 599-60.

14. Ghildiyal M. and Zamore P., *Small silencing RNAs: an expanding universe,* Nat. Rev. Genet., 2009. **10**(2): 94-108

15. Hutvágner, Zamore G. and Phillip D., *A microRNA in a Multiple-Turnover RNAi Enzyme Complex,* Science, 2002. **297**(5589): 2056-2060.

16. Stark G., Kerr I., Williams B., Silverman R. and Schreiber R., *How cells respond to interferons,* Annu. Rev. Biochem., 1998. **67**: 227-264.

17. Bonetta L., *RNAi: Silencing never sounded better,* Nat. Methods., 2004. **1**: 79 − 86.

18. Watts J., Deleavey G. and Damha M., *Chemically modified siRNA: tools and applications*, Drug Discov. Today, 2008. **13**(19-20): 842-855.

19. Akthar S. and Benter I., *Nonviral delivery of synthetic siRNAs in vivo,* J Clin Invest. 2007. **117**(12): 3623-3632.

20. Lam J., Liang W. and Chan H., *Pulmonary delivery of therapeutic siRNA,* Adv. Drug Delivery Rev., 2011. **64**(1): 1-15.

21. Gardlik R., Palffy R., Hodosy J., Lukacs J., Turna J. and Celec P., *Vectors and delivery systems in gene therapy,* Med Sci Monit., 2005. **11**(4): 110-121.

22. Promega (Online), *Protocols & Applications Guide: Transfection*, 2011. Available from: http://www.promega.com/resources/product-guides-and-selectors/protocols-and-applications-guide/transfection/ (Downloaded February 6, 2012).

23. Human Genome Project Information (Online). Source: U.S. Department of Energy Genome Programs, *Gene Therapy*. Last modified: August 24, 2011. Available from: http://www.ornl.gov/sci/techresources/Human_Genome/medicine/genetherapy.shtml (Downloaded January 26, 2012).

24. Thomas C., Ehrhardt A. and Kay M., *Progress and problems with the use of viral vectors for gene therapy*, Nat. Rev. Genet., 2003. **4**: 346-358.

25. Nguyen J. and Szoka F., *Nucleic Acid Delivery: The Missing Pieces of the Puzzle?*, Acc. Chem. Res., 2012 (Not yet published), Available online at: http://pubs.acs.org/doi/full/10.1021/ar3000162. (Downloaded March 26, 2012)

26. Grimm D. et al., *Fatality in mice due to oversaturation of cellular microRNA/short hairpin RNA pathways*, Nature, 2006. **441**: 537-541.

27. Hillaireau H. and Couvreur P., *Nanocarriers' entry into the cell: relevance to drug delivery*, Cell. Mol. Life Sci., 2009. **66:** 2873–2896.

28. Kono K. et al., *Novel gene delivery systems: complexes of fusigenic polymer-modified liposomes and lipoplexes,* Gene Ther., 2001. **8**(1): 5-12.

29. Mansouri S., Lavigne P., Corsi K., Benderdour M., Beaumont E. and Fernandes J.C., *Chitosan-DNA nanoparticles as non-viral vectors in gene therapy: strategies to improve transfection efficacy*, Eur. J. Pharm. Biopharm., 2004. **57**: 1-8.

30. Gene Therapy Net (Online), *Lipoplexes and Polyplexes*. Last modified: 2012. Available from: http://www.genetherapynet.com/non-viral-vectors/lipoplexes-and-polyplexes.html (Downloaded March 14 2012).

31. Patil S.D., Rhodes D. and Burgess D., *Biophysical characterization of anionic lipoplexes,* Biochim. Biophys. Acta, Biomembr., 2005. **1711**(1): 1-11.

32. Brown M., Schatzlein A. and Uchegbu I., *Gene delivery with synthetic (non-viral) carriers,* Int. J. Pharm., 2001. **229:** 1-21.

33. Akhtar S. and Benter I., *Toxicogenomics of non-viral drug delivery systems for RNAi: Potential impact on siRNA-mediated gene silencing activity and specificity*, Adv. Drug Delivery Rev., 2007. **59**(2-3): 164-182.

34. Zauner W., Ogris M. and Wagner E., *Polylysine-based transfection systems utilizing receptor-mediated delivery*, Adv. Drug Delivery Rev., 1998. **30**(1-3): 97-113.

35. Tripathi S., Goyal R., Kumar P. and Gupta K., *Linear polyethylenimine-graft-chitosan copolymers as efficient DNA/siRNA delivery vectors in vitro and in vivo*, Nanomedicine, 2012. **8**(3): 337-345.

36. Strand S., Issa M.M., Christensen B.E., Vårum K.M. and Artursson P., *Tailoring of Chitosans for Gene Delivery: Novel Self-Branched Glycosylated Chitosan Oligomers with Improved Functional Properties*, Biomacromolecules, 2008. **9**: 3268–3276.

37. Strand S., Lelu S., Reitan N., de Lange Davies C., Artursson P. and Vårum K.M., *Molecular design of chitosan gene delivery systems with an optimized balance between polyplex stability and polyplex unpacking*, Biomaterials, 2009. **31**(5): 975-987.

38. Moghimi M., Symonds P., Murray J.M., Hunter A.C., Debska G. and Szewczyk A., *A two-stage poly (ethylenimine)-mediated cytotoxicity: implications for gene transfer/therapy*, Mol. Ther., 2005. **11**: 990-995.

39. Smidsrød O., Moe S.T., *Biopolymer Chemistry*, Tapir Academic Press, Trondheim, 2008. 398 pp.

40. Christensen B.E., *Compendium for TBT4135 Biopolymer Chemistry, Part 1, Chapter 1.3: Chitin and chitosans,* NOBIPOL, Department of Biotechnology, NTNU, 2011. 5 pp.

41. Wikimedia commons (Online), *Chitosan Synthese.jpg,* Last modified: 2008. Available from:
https://commons.wikimedia.org/wiki/File:Chitosan_Synthese.svg
(Downloaded November 21, 2011).

42. Strand S., Tømmeraas K., Vårum K.M. and Østgaard K., *Electrophoretic Light Scattering Studies of Chitosans with Different Degrees of N-acetylation*, Biomacromolecules, 2001. **2**(4): 1310-1314.

43. Vårum K.M. and Smidsrød O., *Structure-Property Relationship in Chitosans*, Polysaccharides: Structural Diversity and Functional Versatility, Second edition, 2004. 1224 pp.

44. Mao S., Sun W. and Kissel T., *Chitosan-based formulation for delivery of DNA and siRNA*, Adv. Drug Deliv. Rev., 2009. **62**(1): 12-27.

45. Malmo J., Sørgård H., Vårum K. M., Strand S., *siRNA delivery with chitosan nanoparticles: Molecular properties favoring efficient gene silencing*, J. Controlled Release, 2012. **158**(2): 261-268.

46. Liu X. et al., *The influence of polymeric properties on chitosan/siRNA nanoparticle formulation and gene silencing*, Biomaterials, 2007. **28**(6): 1280-1288.

47. Malmo J., Vårum K.M., Strand S., *Effect of Chitosan Chain Architecture on Gene Delivery: Comparison of Self-Branched and Linear Chitosans,* Biomacromolecules, 2011. **12**(3): 721–729.

48. Dash P., Read M., Barrett L., Wolfert M and Seymour L., *Factors affecting blood clearance and in vivo distribution of polyelectrolyte complexes for gene delivery*, Gene Ther., 1999. **6**(4): 643-650.

49. Mao S., Shuai X., Unger F., Wittmar M., Xie X. and Kissel T., *Synthesis, characterization and cytotoxicity of poly(ethylene glycol)-graft-trimethyl chitosan block copolymers*, Biomaterials, 2005. **26**(32): 6343-6356.

50. Tømmeraas K., Köping-Höggård M., Vårum K.M., Christensen B.E., Artursson P. and Smidsrød O., *Preparation and characterisation of chitosans with oligosaccharide branches,* Carbohydr. Res., 2002. **337**(24): 2455-2462.

51. Issa M., Köping-Höggård M., Tømmeraas K., Vårum K. M., Christensen B., Strand S. and Artursson P., *Targeted gene delivery with trisaccharide-substituted chitosan oligomers* in vitro *and after lung administration* in vivo, J. Controlled Release, 2006. **115**(1): 103-112.

52. Fisher D., Osburg B., Petersen H., Kissel T and Bickel U., *Effect of Poly(ethylene imine) molecular weight and pegylation organ distribution and pharmacokinetics of polyplexes with oligodeoxynucleotides in mice*, Drug Metab. Dispos., 2004. **32**(9): 983-992.

53. Lee H., Jeong J. and Park T., *PEG grafted polylysine with fusogenic peptide for gene delivery: high transfection efficiency with low cytotoxicity*, J. Controlled Release, 2002. **79**(1-3): 283-291.

54. Zhang Y. et al., *A novel PEGyaltion of chitosan nanoparticles for gene delivery, Biotechnol Appl. Biochem.*, 2007. **46**: 197-204.

55. Rampon C. et al., *Molecular mechanism of systemic delivery of neural precursor cells to the brain: assembly of brain endothelial apical cups and control of transmigration by CD44*, Stem Cells, 2008. **26**(7): 1673-1682.

56. Lu H.D., Zhao H.Q., Wang K. and Lv L.L., *Novel hyaluronic acid–chitosan nanoparticles as non-viral gene delivery vectors targeting osteoarthritis*, Int. J. Pharm., 2011. **420**(2): 358-365.

57. Mansouri S. et al., *Characterization of folate-chitosan-DNA nanoparticles for gene therapy*, Biomaterials, 2006. **27**(9): 2060-2065.

58. Sahay G., Alakhova D.Y., Kabanov A., *Endocytosis of nanomedicines*, J. Controlled Release, 2010. **145**(3): 182-195.

59. Conner S.D. and Schmid S. L., *Regulated portals of entry into the cell*, Nature, 2003. **422**: 37-44.

60. Lukyanenko V. et al., *Enterohemorrhagic Escherichia coli infection stimulates Shiga toxin 1 macropinocytosis and transcytosis across intestinal epithelial cells*, Am. J. Physiol. Cell Physiol., 2011. **301**(5): 1140-1149.

61. Nam H.Y. et al., *Cellular uptake mechanism and intracellular fate of hydrophobically modified glycol chitosan nanoparticles*, J. Controlled Release, 2009. **135**(3): 259-267

62. Rejman J., Oberle V., Zuhorn I. and Hoekstra D., *Size-dependent internalization of particles via the pathways of clathrin- and caveolae-mediated endocytosis*, Biochem. J., 2004. **377**: 159-169.

63. van der Aa M.A.E.M. et al., *Cellular Uptake of Cationic Polymer-DNA Complexes Via Caveolae Plays a Pivotal Role in Gene Transfection in COS-7 Cells*, Pharm. Res. 2007. **24**(8): 1590–1598.

64. Köping-Höggård M., Tubulekas I., Guan H., Edwards K., Nilsson M., Vårum K. M. and Artursson P., *Chitosan as a nonviral gene delivery system. Structure-property relationships and characteristics compared with polyethylenimine in vitro and after lung administration in vivo*, Gene Ther., 2001. **8**(14): 1108-1121.

65. Mao H-Q. et al., *Chitosan-DNA nanoparticles as gene carriers: synthesis, characterization and transfection efficiency*, J. Controlled Release, 2001. **70**(3): 399-421.

66. Behr J-P., *The Proton Sponge: a Trick to Enter Cells the Viruses Did Not Exploit*, Chimia Int. J. Biochem., 1997. **51**: 34-36.

67. Medina-Kauwe LK., Xie J. and Hamm-Alvarez S., *Intracellular trafficking of non-viral vectors,* Gene Ther., 2005. **12**: 1734-1751.

68. Sonawane N.D., Szoka F. and Verkman A.S., *Chloride Accumulation and Swelling in Endosomes Enhances DNA Transfer by Polyamine-DNA Polyplexes*, J. Biol. Chem., 2003. **278**(45): 44826-44831.

69. Abbott J. N., Patabendige A., Dolman D., Yusof S and Begley D., *Structure and function of the blood-brain barrier,* Neurobiol. Dis., 2010. **37**: 13-25.

70. Pardrigde W., *Blood-brain barrier biology and methodology*, J. Neurovirol., 1999, **5:** 556-569.

71. Löscher W. and Potschka H., *Role of drug efflux transporters in the brain for drug disposition and treatment of brain diseases*, Prog. Neurobiol., 2005. **76**: 22-76.

72. Fromm M., *Importance of P-glycoprotein at blood-tissue barriers*, Trends Pharmacol. Sci., 2004. **25**(8): 423-429.

73. Schinkel A., *P-glycoprotein, a gatekeeper in the blood-brain barrier,* Adv. Drug Delivery Rev., 1999. **36**(2-3): 179-194.

74. The International Transporter Consortium (Giacomini K. et al), *Membrane Transporters in drug development,* Nat. Rev. Drug Discovery, 2010. **9**: 215-236.

75. Oesterheld J., GenemedRX (Online), *P-gp (ABCB1) Introduction*, Last modified: 2008.
Available from: http://www.genemedrx.com/PGP_Introduction.php
(Downloaded February 6, 2012).

76. Deeken J. and Löscher W., *The Blood-Brain Barrier and Cancer: Transporters, Treatment, and Trojan Horses*, Clin Cancer Res., 2007. **13**: 1663-1674.

77. Summers M., Moore J. and McAuley J., *Use of Verapamil as a Potential P-Glycoprotein Inhibitor in a Patient with Refractory Epilepsy*, Ann. Pharmacother, 2004. **38**(10): 1631-1634.

78. Gottesman M., Fojo T. and Bates S., *Multidrug Resistance in Cancer: Role of ATP-dependent Transporters,* Nat. Rev. Cancer, 2002. **2**: 48-58.

79. Sawada T., Kato Y., Sakayori N., Takekawa Y. and Kobayashi M., *Expression of the multidrug-resistance P-glycoprotein (Pgp, MDR-1) by endothelial cells of the neovasculature in central nervous system tumors*, Brain Tumor Pathol., 1999. **16**: 23-27.

80. Bradley G. and Ling V., *P-glycoprotein – multidrug resistance and tumor progression,* Cancer Metastasis Rev., 1994. **13**: 223-233.

81. Abbott J. N., *Astrocyte–endothelial interactions and blood–brain barrier permeability*, J Anat., 2002. **200**(6): 629–638.

82. Lee SW. et al., *SSeCKS regulates angiogenesis and tight junction formation in blood-brain barrier*, Nat. Med., 2003. **9**: 900-906.

83. Givan A., *Flow Cytometry - An Introduction,* Methods Mol. Biol., 2011. **699**: 1-29.

84. Holla H., Flow Cytometry Facility (Online). Source: U.C. Berkeley, *Basic Principles in Flow Cytometry*, (No date given).
Available from: http://biology.berkeley.edu/crl/about_flow_cytometry.html
(Downloaded April 13, 2012).

85. Lady Davis Institute for Medical Research (Online). Source: Jewish General Hospital, *Introduction to Flow Cytometry*, 2010.
Available from: http://ladydavis.ca/en/introductionflowcytometry
(Downloaded April 13, 2012).

86. van Pelt-Verkuli E., van Belkum A. and Hays J., *Principles and Technical Aspects of PCR Amplification,* Springer, First edition, 2008. 325 pp.

87. Life Technologies™, Applied Biosystems™ (Online), *Taqman® and SYBR® Green Chemistries*, 2011.
Available from:
http://www.appliedbiosystems.com/absite/us/en/home/applications-technologies/real-time-pcr/taqman-and-sybr-green-chemistries.html
(Downloaded April 26, 2012).

88. Williams D.B. and Carter C.B., *Transmission Electron Microscopy, A Textbook for Material Science,* Spinger, Second edition, 2009. 757 pp.

89. Esau K., Cheadle Center for Biodiversity and Ecological Restoration (Online). Source: UC Santa Barbara, *Transmission Electron Microscope*, Last modified: 28/1-11. Available from: http://www.ccber.ucsb.edu/research/esau/topics-of-study/microscopes/
(Downloaded April 13, 2012).

90. Atomic World, Physics World webpage (Online). Source: Physics Department and Faculty of Education, CUHK, *Basic principle of transmission electron microscope*,
Available from: http://www.hk-phy.org/atomic_world/tem/tem02_e.html
(Downloaded April 13, 2012).

91. Declèves X., Bihorel S., Debray M., Yousif S., Camenisch G. and Scherrmann J.M., *ABC transporters and the accumulation of imatinib and its active metabolite CGP74588 in rat C6 glioma cell,* Pharmacol. Res., 2008. **57**(3): 214-222.

92. Wilson R., *The use of gold nanoparticles in diagnostics and detection*, Chem. Soc. Rev., 2008. **37**: 2028-2045.

93. Sørgård, H.K., *Chitosan-mediated siRNA delivery in a blood-brain barrier model* in vitro, Master thesis, Department of Biotechnology, NTNU, 2011.

94. Malmo J., *Gene Therapy: Chitosan-based nanoparticles for siRNA-delivery in human cells,* Master thesis, Department of Biotechnology, NTNU, 2009.

95. Auganes H., *Chitosan-based nanoparticles for siRNA-mediated downregulation of P-glycoprotein in rat brain endothelial cells in vitro*, Master thesis, Department of Biotechnology, NTNU, 2011.

96. Dille, M., *Kitosanbaserte nanopartikler for siRNA-levering i humane celler*, Master thesis, Department of Biotechnology, NTNU, 2010.

97. Martin S.E. and Caplen N.J., *Applications of RNA interference in Mammalian Systems*, Annu. Rev. Genomics Hum. Genet., 2007. **8:** 81-108

98. Sledz C.A., Holko M., de Veer M.J., Silverman R.H. and Williams B.R.G., *Activation of the interferon system by short-interfering RNAs,* Nat. Cell Biol., 2003. **5:** 834-839.

99. Wimardani Y.S., Suniarti D.F., Freisleben H-J., Wanandi S.I. and Ikedi M-A., *Cytotoxic effects of chitosan against oral cancer cell lines is molecular-weigh dependent and cell-type specific*, Int. J. Oral Res. 2012. **3:**e1

100.   Qi L. and Zu Z., *In vivo antitumor activity of chitosan nanoparticles*, Bioorg. Medicinal Chem. Lett., 2006. **16**(16): 4243-4245.

101.   Taki T., Ohnishi T., Arita N., Hiraga S. and Hayakawa T., *In vivo etoposide-resistant C6 glioma cell line: Significance of altered DNA topoisomerase II activity in multi-drug resistance,* J. Neurooncol., 1998. **36:** 41-53.

102.   Bennis S., Chapey C., Couvreur P. and Robert J., *Enhanced cytotoxicity of doxorubicin encapsulated in polyisohexylcyanoacrylate nanospheres against multi-drug resistant tumour cells in culture*, Eur. J. Cancer, 1994. **30A**(1): 89-93.

103.   Hirsch-Ernst K.I., Ziemann C., Foth H., Kozian D., Schmitz-Salue C. and Kahl G.F., *Induction of mdr1b mRNA and P-Glycoprotein Expression by Tumor Necrosis Factor Alpha in Primary Rat Hepatocyte Cultures,* J. Cell. Physio., 1998. **176**: 506-515.

104.   Schinkel A.H. et al., *Normal viability and altered pharmacokinetics in mice lacking mdr1-type (drug-transporting) P-glycoproteins*, PNAS, 1997. **94**(8): 4028-4033.

105.   Makhey V.D., Guo A., Norris D.A., Hu P., Yan J. and Sinko P.J.*, Characterization of the Regional Intestinal Kinetics of Drug Efllux in Rat and Human Intestine and in Caco-2 Cells,* Pharmaceut. Res., 1998. **15**(8): 1160-1167.

106.   Klemetsaune L.K., *Gene Therapy: Chitosan Based Nanoparticles for siRNA delivery in Human Cells,* Master thesis, Department of Biotechnology, NTNU, 2009.

107.   Martins S., Costa-Lima S., Carneiro T., Cordeiro-da-Silva A., Souto E.B. and Ferreira D.C., *Solid lipid nanoparticles as intracellular drug transporters: An investigation of the uptake mechanism and pathway,* Int. J. Pharm., 2012. **430**(1-2): 216-227.

108.   Harush-Frenkel O., Rozentur E., Benita S. and Altschuler Y., *Surface Charge of Nanoparticles Determines Their Endocytic and Transcytotic Pathway in Polarized MDCK Cells,* Biomacromolecules, 2008. **9**(2): 435-443.

109.   Tammi R. et al., *Hyaluronan Enters Keratinocytes by a Novel Endocytic Route for Catabolism,* J. Biol. Chem., 2001. **276**: 35111-35122.

110.   Poller B. et al., *The human brain endothelial cell line hCMEC/D3 as a human blood-brain barrier model for drug transport studies,* J. Neurochem., 2008. **107**: 1358-1368.

111.   Casettari L., Vllasaliu D., Castagnino E., Stolnik S., Howdle S. and Illum L., *PEGylated chitosan derivatives: Synthesis, characterizations and pharmaceutical applications,* Prog. Polym. Sci., 2012. **37**(5): 659-685.

112.   Gao S. et al., *The effect of Chemical Modification and Nanoparticle Formulation on Stability and Biodistribution of siRNA in Mice*, Mol. Ther., 2009. **17**(7): 1225-1233.

Appendices

A: Product numbers of reagents

Production Numbers of reagents:

Allstars Neg. siRNA AF 647 (Alexa 647)	1027295	Qiagen
Silencer® Select: Abcb1a siRNA	4390771	Ambion ®
Silencer® Select: GAPDH siRNA (Hs. Mm. Rn.)	4390849	Ambion®
Silencer® Select: negative control siRNA	4390843	Ambion®
Luciferase GL3 duplex siRNA	D-001400-01-20	Dharmacon®
Lipofectamine™ RNAiMAX	13778075	Invitrogen®
Rhodamine 123 (R123)	62669-70-9	Sigma-Aldrich®
DMEM	41965-039	Gibco®/Invitrogen®
α-MEM	22571-020	Gibco®/Invitrogen®
PBS	14190-094	Gibco®/Invitrogen®
MBG Water	2900136	5 Prime
MEM NEAA	11140-035	Gibco®/Invitrogen®
Opti-MEM ®	31985	Gibco®/Invitrogen®
HBSS	14025-050	Gibco®/Invitrogen®
KDalert Lysis Buffer	8790G	Ambion®
KDalert Master Mix	8791G/8792G/8793G	Ambion®
Heparin	H3393-10KU	Sigma-Aldrich®
FBS	F7524	Sigma-Aldrich®
Trypsin/EDTA	25300096	Gibco®/Invitrogen®
Adriamycin® (Doxorubicin hydrochloride)	012948	Pharmacia
Verapamil	152-11-4	Sigma-Aldrich®
HEPES	H3375	Sigma-Aldrich®
Mannitol	103304Y	BDH-AnalaR®
Rat tail type I collagen	354249	BD Biosciences
PEST	P0781	Sigma-Aldrich®
Hyaluronic acid	Not given	Novamatrix™
G418	A1720	Sigma-Aldrich®
bFGF	13256-029	Invitrogen®

B: Calculation examples

This section gives calculation examples from the different calculations carried out during the experiments.

B1. Formulation of the nanoparticles

96-well plates were used for cell experiments, using three, four or six parallels for each sample. With a volume of 50 µL/well and a 10 % loss rate, the total volume of solution for six wells would be 50 µL × 6 wells × 1.1 = 330 µL. The formulations were diluted 1:1 with hypertonic Opti-MEM, thus 165 µL nanoparticle solution was made. An example of the composition of different formulations is shown in Table B.1, taken from GAPDH experiment in RBE4 cells, presented in

siRNA
The volume of siRNA is calculated from the concentration of the siRNA stock solution (66.5 µg/mL) and the number of parallels for each sample. For a 100 nM siRNA concentration, the dosage is 66.67 ng/well, which gives the following calculation of siRNA volume for six wells from the stock solution:

$$\left(\frac{66.67 \; ng \; siRNA}{well} \times 6 \; wells \right) \times 1.1 = 440 \; ng = 0.44 \; \mu g$$

$$\frac{0.44 \; \mu g \; siRNA}{66.5 \frac{\mu g \; siRNA}{mL}} = 6.62 \; \mu L \; siRNA$$

Chitosan
For a linear chitosan with $F_a = 0$, the relationship between chitosan and siRNA at N/P 1 is 0.584 µg chitosan to 1 µg siRNA. Since the stock solutions of chitosans were 0.1 µg/µL, the volume of chitosan added for N/P 30 for six wells becomes:

$$\frac{\frac{0.584 \; \mu g \; chitosan}{1 \; \mu g \; siRNA} \times 0.44 \; \mu g \; siRNA}{0.1 \frac{\mu g}{\mu L}} \times 30 = 77.1 \; \mu L$$

For substituted chitosans the amount of chitosan must increase for the same N/P due to lower charge density. At N/P 30, 100 nM siRNA, the amount of F_a=0 (2 % PEG) was 115.3 µL and the amount of DP_{85} (4AM) was 111.4, from stock solutions of 0.1 µg/µL.

MBG Water
The required volume of MBG water for six wells with the above given siRNA and chitosan volumes would be 165 µL – 77.1 µL – 6.62 µL = 81.3 µL.

Gold particles and Hyaluronic acid
The amount of gold particles added was 2.5 x 10^8/mL, and from a stock solution of 1 x 10^{11} this was 2.5 µL stock solution/mL.
The amount of HA (1 mg/mL) added for six wells at N/P 30 and 100 nM siRNA was 23.1 µL.

Table B.1: The composition of different nanoparticles from the uptake experiment presented in Figure 4.9, Section 4.2.2. LIN250, LIN250 w/HA, LIN350, LIN350 w/HA, DP_{85} (4AM) or $F_a=0$ (2% PEG) chitosans with N/P 10 and 30 and Alexa 647 siRNA were used. Untreated cells and cells treated with naked siRNA (siRNA) were included as controls.

	LIN250			LIN350		
	1:0 HA	1:3 HA	1:3 HA	1:0 HA	1:3 HA	1:3 HA
N/P	30	10	30	30	10	30
siRNA (μL), 66.5 ug/ml	6.6	6.6	6.6	6.6	6.6	6.6
chitosan (μL), 0.1 mg/ml	77.1	25.6	77.1	77.1	25.6	77.1
HA (μL) 1 mg/ml	0	7.7	23.1	0	7.7	23.1
MBG water (μL)	81.3	125.1	58.2	81.3	125.1	58.2
Total (μL)	**165**	**165**	**165**	**165**	**165**	**165**
	DP85 (4AM)		**Fa=0 (2% PEG)**		**siRNA**	**Untreated**
	4AM	4AM	5 %PEG	5 %PEG	-	-
N/P	10	30	10	30	-	-
Anti-GAPDH (μL), 66.5 ug/ml	6.6	6.6	6.6	6.6	6.6	0.0
chitosan (μL), 0.1 mg/ml	37.2	111.4	38.4	115.3	0.0	0.0
HA (μL) 1 mg/ml	0.0	0.0	0.0	0.0	0.0	0.0
MBG water (μL)	121.2	47.0	120.0	43.1	158.4	165.0
Total (μL)	**165**	**165**	**165**	**165**	**165**	**165**

B2. RNAiMAX

To make lipoplexes, siRNA and RNAiMAX were added to two separate tubes containing Opti-MEM, before adding the volume with RNAiMAX to the siRNA-containing tube, as seen in Table B.2. The example here gives a siRNA concentration of 100 nM.

Table B.2: An Opti-MEM/RNAiMAX solution (tube 2) was transferred to Opti-MEM and siRNA (tube 1) to make RNAiMAX lipoplexes at a 100 nM siRNA concentration.

100 nM	Tube 1 (μL)	Tube 2 (μL)
siRNA	6.61	-
RNAiMAX	-	5.87
Opti-mem	158.39	159.13
Total	165	165

B3. GAPDH knockdown

GAPDH activity causes a reduction in A_{615} in the samples, and the GAPDH activity (ΔA_{615}) for a given sample is calculated by subtracting the A_{615} from the sample ($A_{615\text{-sample}}$) from the average A_{615}-value from the Master mix control ($A_{615\text{-blank}}$):

$\Delta A_{615\text{-sample}} = A_{615\text{-blank}} - A_{615\text{-sample}}$

To determine the percentage remaining GAPDH activity in a sample, the ratio between ΔA_{615} of the sample and the average value from the untreated control sample is determined:

$$100 \times \frac{\Delta A615 \text{ (sample)}}{\Delta A615 \text{ (untreated)}} = \text{\% remaining GAPDH expression}$$

An example is taken from the from the C6 cells, using parallel 1 of the sample transfected with LIN350 and anti-GAPDH siRNA (T) at 50 nM, (appendix D, Table D.1):

$0.380 - 0.296 = 0.084 = \Delta A_{615\text{-sample}}$

$100 \times \frac{0.084}{0.244} = 34.4 \text{ \%} = \text{\% remaining GAPDH expression of the untreated control}$

B4. RT-PCR

To calculate the levels of *Abcb1a* mRNA found from the RT-PCR experiments, the comparative critical threshold method (2ddCt) was used, using C_t (threshold values) from the amplification plots of *Abcb1a* and *ATCB* mRNAs (Appendix E, Figure E.1 and E.2) to determine mRNA levels relative to the RBE4 cells. The mean C_t values were determined from the RBE4 C_t values for each mRNA.

$$2ddCt = 2^{-((Ct\,Abcb1a - Ct\,ATCB) - (Mean\,Ct\,Abcb1a - Mean\,Ct\,ACTB))}$$

$$\% \, mRNA \, compared \, to \, RBE4 \, cells = \frac{2ddCt \times 100}{average \, 2ddCt \, from \, RBE4}$$

An example is given from the C6 px 19 sample (parallel 1, from Table D.15). The average 2ddCt from RBE4 was 1.186:

$$2ddCt \, (C6 \, px \, 19 \, parallel \, 1) = 2^{-((24.24 - 16.201) - (23.08 - 16.39))} = 0.393$$

$$\% \, mRNA \, compared \, to \, RBE4 \, cells = \frac{0.393 \times 100}{1.186} = 33.1 \text{ \%}$$

C: Flow Cytometry diagrams

A dot plot generated by the forward-scatter and side-scatter detectors makes it possible to select appropriate gating of the cells in a sample. An example of such a plot, as well a typical plot obtained from the FL1 channel measuring intracellular R123 is shown in Figure C.1.

Overlay plots of the median FI values of samples from all the different experiments are presented in Figure C2-Cx, showing selected examples from each experiment. In all figures anti-Abcb1a siRNA is designated T, while negative control
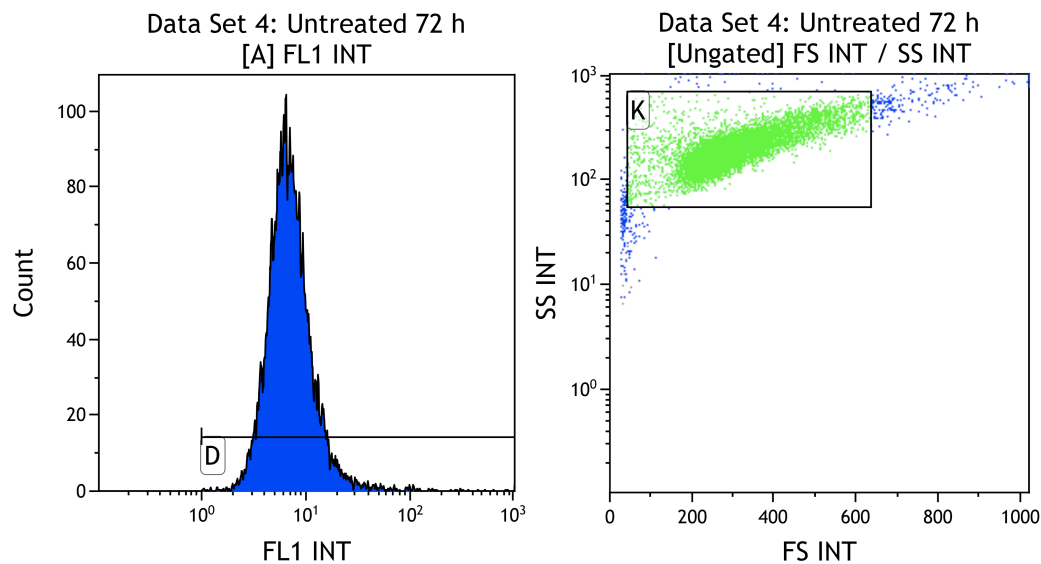
Figure C.1: Showing two plots from an untreated cell sample from the P-gp kinetics experiment in RBE4 cells, after 72 h.
Left: An example of a fluorescence plot of R123 in the FL1 channel, giving median fluorescence intensities on a logarithmic scale (FL1 INT, the x-axis) and the cell count (Count, y-axis).
Right: A dot plot generated from the side-scatter (SS INT, y-axis) vs. forward scatter (FS INT, x-axis) of the cells, giving number of cells on a linear scale. The square (K) is selected for the area with highest cell density for appropriate gating of the cells.
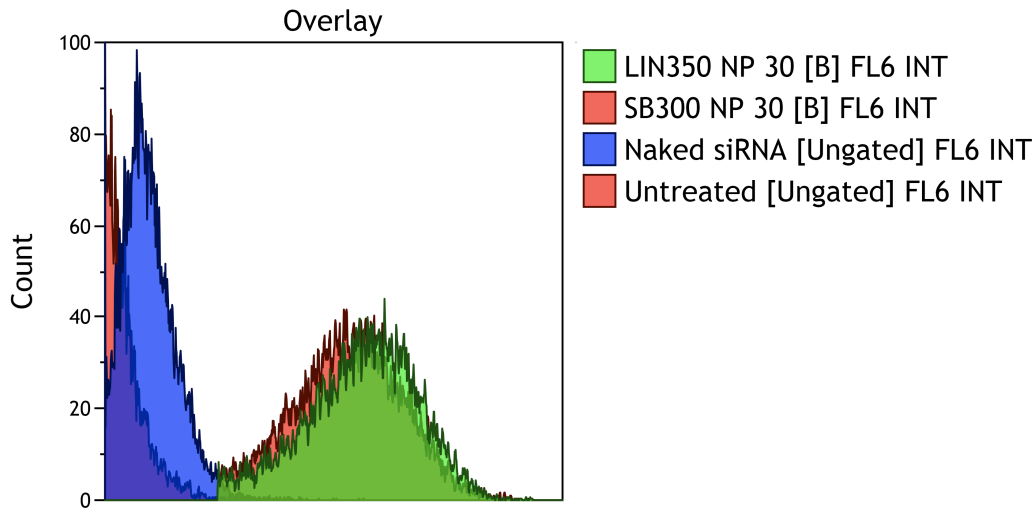
Figure C.2: An overlay plot of different samples from an uptake experiment in C6 cells, showing LIN350 and SB300 at N/P 30, naked siRNA and untreated cells. The y-axis gives the cell count for each sample. The data are presented in Figure 4.1A, section 4.1.1, and raw data are found in appendix D.

Figure C.3: An overlay plot of different samples from an uptake experiment in C6 cells, showing LIN350, SB300 and RNAiMAX with 50 or 100 nM siRNA concentrations, naked siRNA and the untreated control. The y-axis gives the cell count for each sample. The data are presented in Figure 4.1B, section 4.1.1, and raw data in Appendix D.

Figure C.4: An overlay plot of different samples from an uptake experiment in RBE4 cells, showing LIN350, LIN350 w/HA, F_a=0 (2% PEG), DP_{85} (4AM) at N/P 30, naked siRNA and the untreated control. The y-axis gives the cell count for each sample. The data are presented in Figure 4.7, section 4.2.1.1, and the raw data are found in Appendix D.
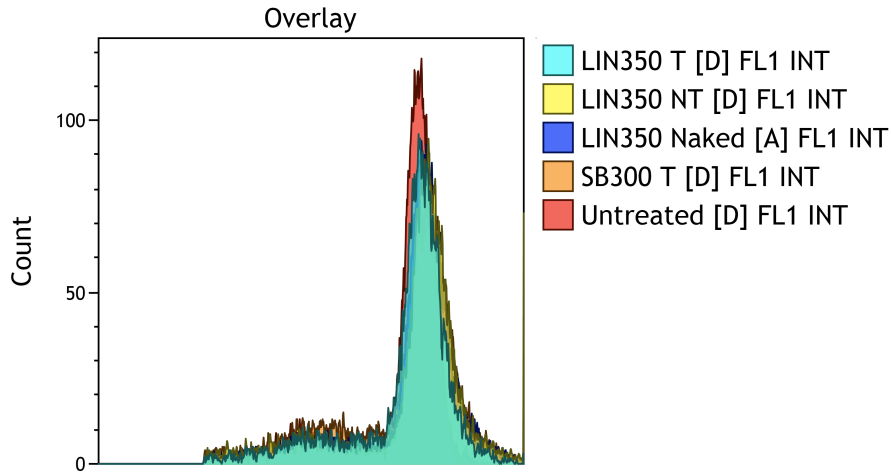
Figure C.5: An overlay plot of different samples from the R123 experiment in C6 px 4-cells, using LIN350 and SB300 with anti-Abcb1a (T) or negative control (NT) siRNA, or naked chitosan, and untreated cells. The y-axis gives the cell count for each sample. The data are presented in Figure 4.3, section 4.1.3, and the raw data are found in Appendix D.
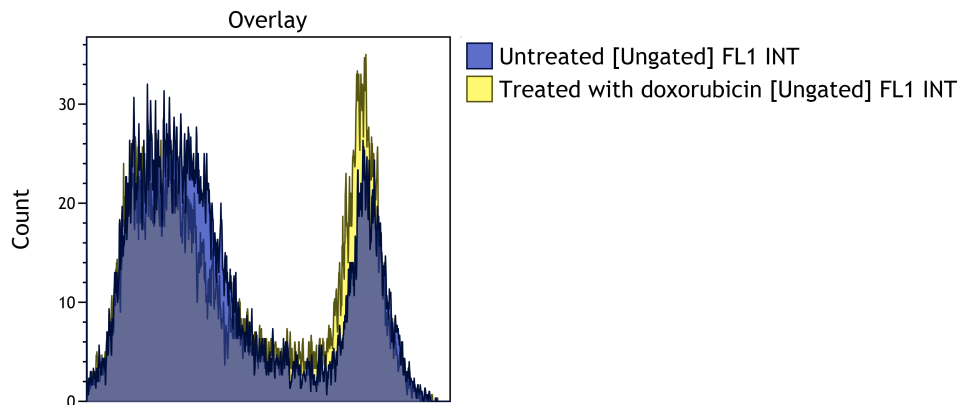
Figure C.6: An overlay plot comparing untreated cells and cells grown in doxorubicin-containing medium, measuring R123 levels. There were two distinct peaks in both samples, indicating that some of the cells had high R123 levels and some has low R123 levels. The y-axis gives the cell count for each sample. The data are presented in Figure 4.4, section 4.1.3, and the raw data are found in Appendix D.
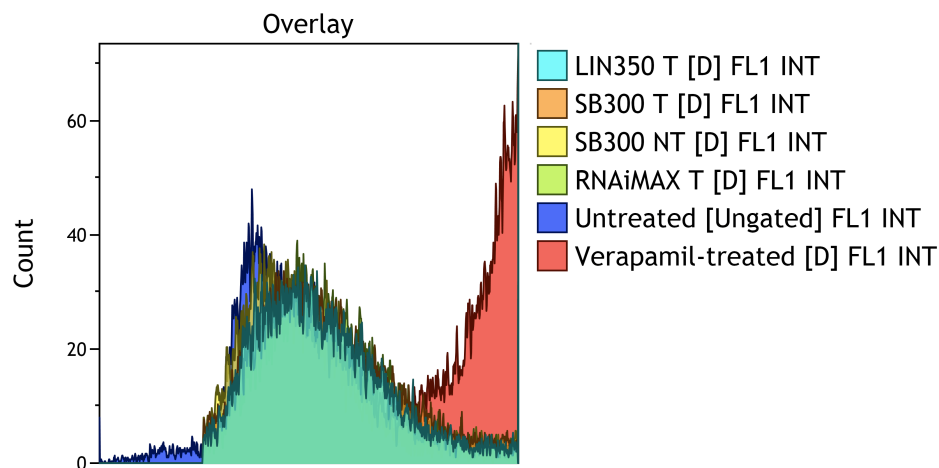
Figure C.7: An overlay plot of different samples from the R123 experiment in C6 px 19-cells, using LIN350, SB300 and RNAiMAX, as well as untreated cells with or without verapamil. The y-axis gives the cell count for each sample. The data are presented in Figure 4.5, section 4.1.3, and the raw data are found in Appendix D.
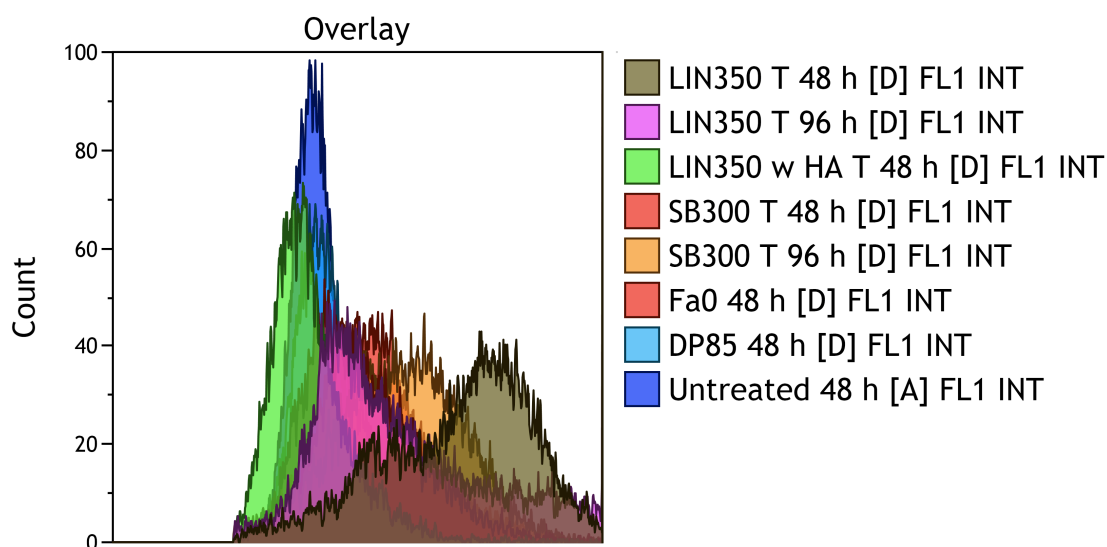
Figure C.8: An overlay plot of the different samples from an R123 efflux experiment in RBE4 cells. The examples shown here are LIN350, LIN350 w/HA, SB300, $F_a=0$ (2% PEG), DP_{85} (4AM) at 48 or 96 h. The y-axis gives the cell count for each sample. The data are presented in Figure 4.11, section 4.2.3.1, and the raw data are found in Appendix D.
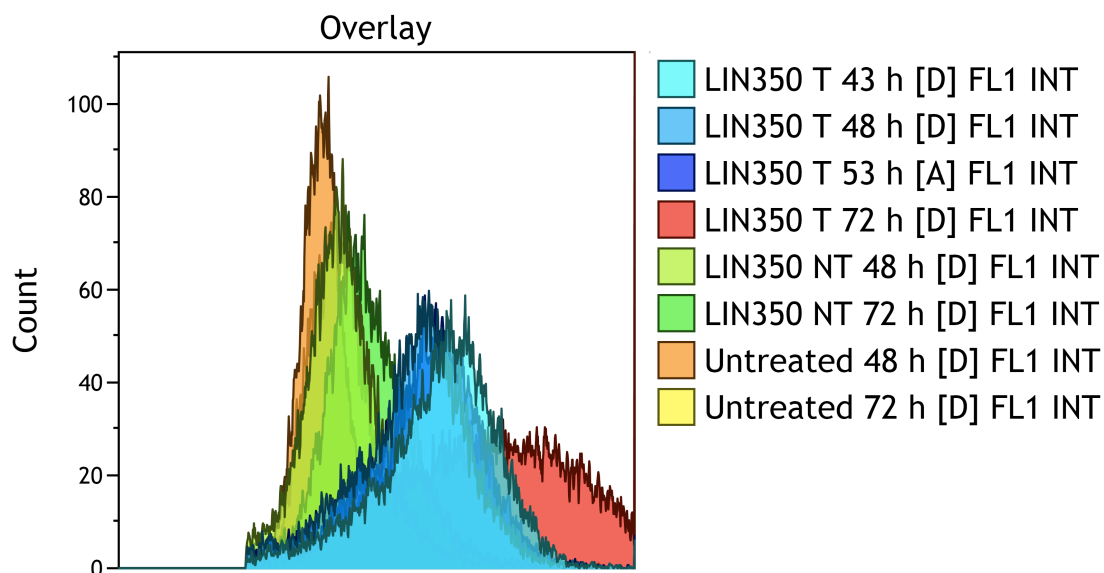
Figure C.9: An overlay plot of the different samples from an R123 efflux experiment in RBE4 cells. LIN350 at 43, 48, 53 and 72 h was compared in regards to R123 efflux. The y-axis gives the cell count for each sample. The data are presented in Figure 4.13, section 4.2.3.2, and the raw data are found in Appendix D.
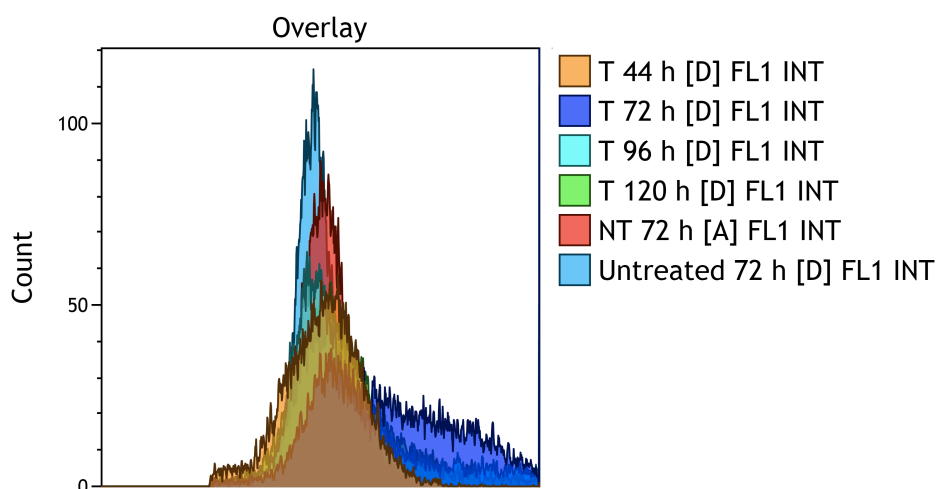
Figure C.10: An overlay plot of the different samples from the R123 kinetics experiment in RBE4 cells, showing cells transfected one time (T1) with LIN350, and measured after 44, 72, 96 and 120 h. Untreated cells are also shown. The y-axis gives the cell count for each sample. The data are presented in Figure 4.12, section 4.2.3.2, and the raw data are found in Appendix D.
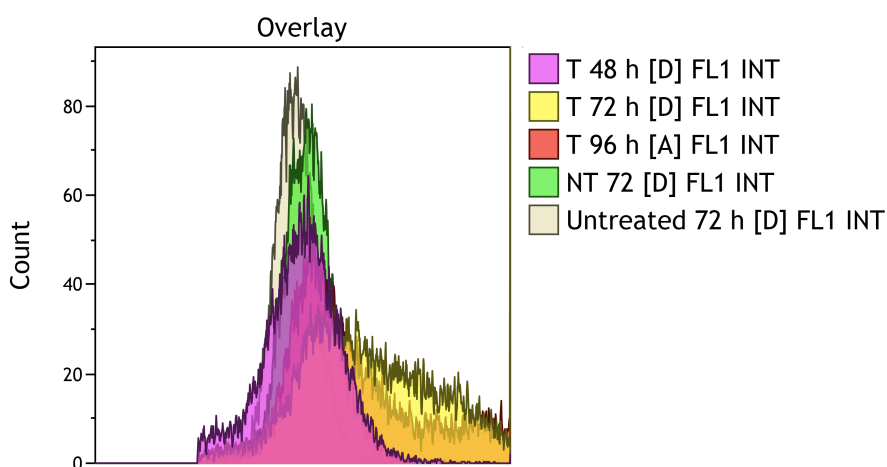
Figure C.11: An overlay plot of the different samples from the R123 kinetics experiment in RBE4 cells, showing cells transfected two times (T2) with LIN350, and measured after 44 (48), 72 and 96 h and. Untreated cells are also shown. The y-axis gives the cell count for each sample. The data are presented in Figure 4.12, section 4.2.3.2, and the raw data are found in Appendix D.
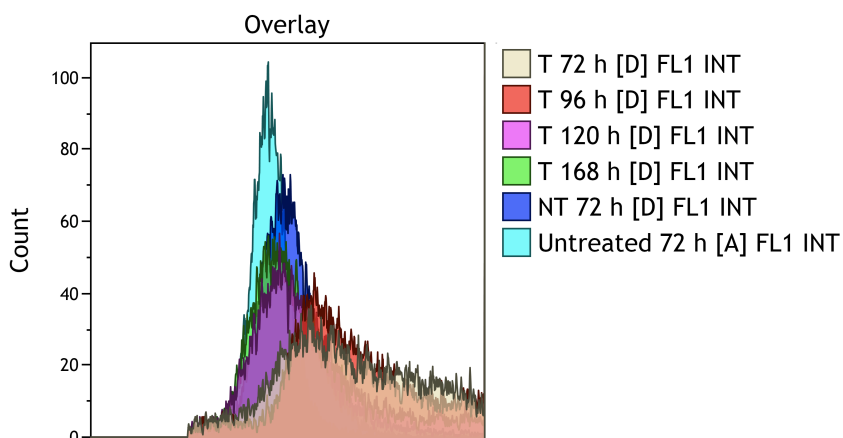
Figure C.11: An overlay plot of the different samples from the R123 kinetics experiment in RBE4 cells, showing cells transfected three times (T3) with LIN350, and measured after 72, 96, 120 and 168 h.

Untreated cells are also shown. The y-axis gives the cell count for each sample. The data are presented in Figure 4.12, section 4.2.3.2, and the raw data are found in Appendix D.
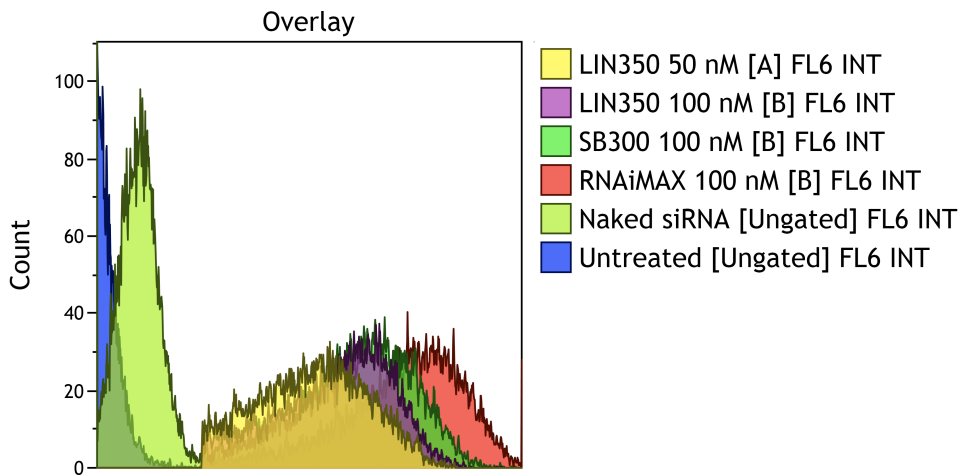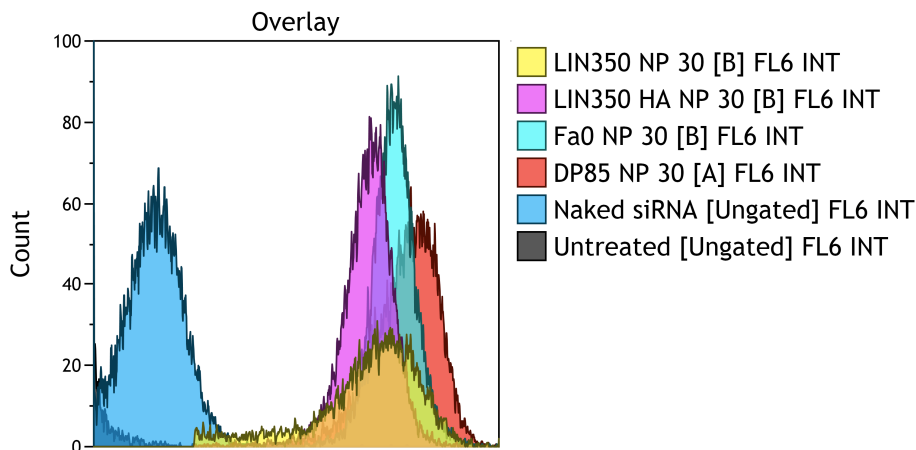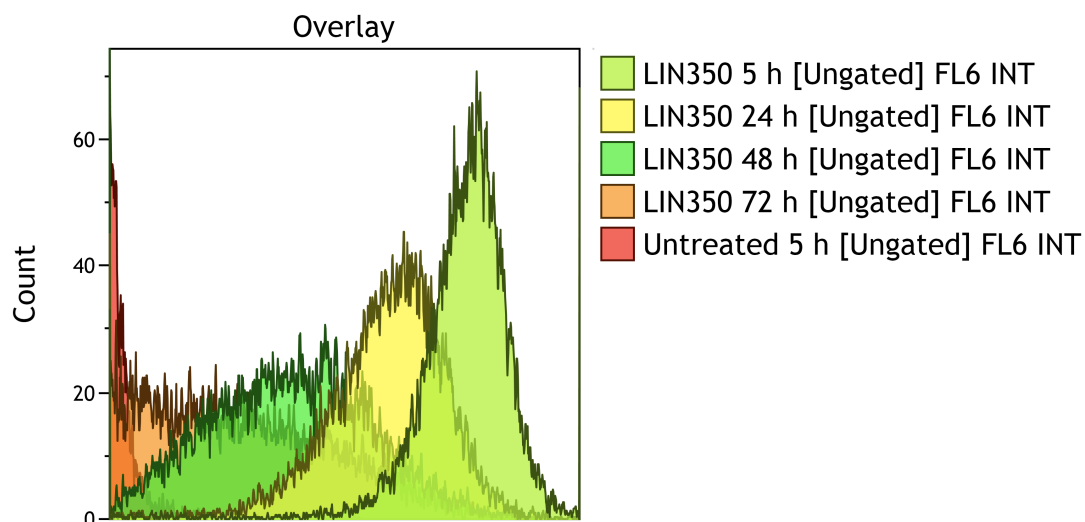

Figure C.12: An overlay plot of different samples from the uptake kinetics experiment in RBE4 cells, with LIN350-Alexa 647 siRNA nanoparticles measured for fluorescence intensities after 5, 24, 48 and 72 h, giving the cell count (y-axis). Untreated cells measured after 5 h were included as a control. The data are presented in Figure 4.8, section 4.2.1.2, and raw data in Appendix D.
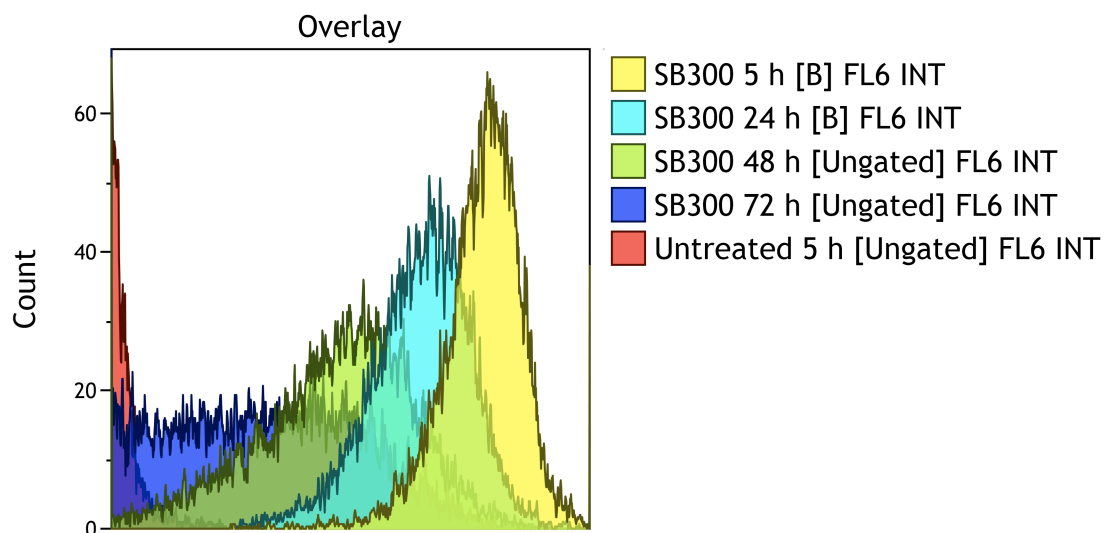
Figure C.13: An overlay plot of different samples from the uptake kinetics experiment in RBE4 cells, with SB300-Alexa 647 siRNA nanoparticles measured for fluorescence intensities after 5, 24, 48 and 72 h, giving the cell count (y-axis). Untreated cells measured after 5 h were included as a control. The data are presented in Figure 4.8, section 4.2.1.2, and raw data in Appendix D.

D: Experimental data

This sections gives an overview of all the raw data underlying the results presented in Section 4. The data are shown in Table D.1-D.15, giving data and calculations from the KDalert GAPDH assays, the flow cytometry experiments, and from the RT-PCR.

Table D.1: The raw data and calculations obtained from the KDalert GAPDH assay from the C6 cells 48 h after transfection. LIN350, SB300 and RNAiMAX (RMAX) with anti-GAPDH (T) or negative control (NT) siRNA at 50 or 100 nM concentrations and N/P 30 (for the chitosans) formed the nanoparticles. Naked siRNA (siRNA), untreated cells (Untr.) and MBG water + Master Mix (Blank) were included as controls. Absorbance was measured at 615 nm (A_{615}) 15 minutes after adding the Master Mix, and $\Delta A615$ and % remaining GAPDH of the untreated control cells were calculated for each sample using these absorbance values. Cell density was 5,000 cells/well.

	LIN350 50 nM		LIN350 100 nM		SB300 50 nM		SB300 100 nM		RMAX 50 nM		RMAX 100 nM		siRNA	Untr.	Blank
	T	NT	T	NT	T	NT	T	NT	T	NT	T	NT			
A_{615}	0.296	0.147	0.304	0.192	0.326	0.193	0.345	0.274	0.341	0.076	0.324	0.111	0.098	0.120	0.381
	0.294	0.172	0.306	0.187	0.314	0.190	0.336	0.256	0.336	0.107	0.331	0.093	0.104	0.138	0.377
	0.292	0.165	0.297	0.181	0.322	0.191	0.337	0.272	0.351	0.151	0.341	0.172	0.068	0.119	0.376
	0.289	0.168	0.293	0.185	0.321	0.185	0.335	0.278	0.345	0.168	0.348	0.203	0.138	0.168	0.384
Average															0.380
ΔA_{615} (blank - sample)	0.084	0.232	0.075	0.187	0.054	0.187	0.034	0.105	0.039	0.304	0.056	0.268	0.282	0.260	
	0.085	0.207	0.074	0.192	0.065	0.190	0.044	0.123	0.044	0.273	0.048	0.287	0.276	0.242	
	0.087	0.215	0.083	0.199	0.058	0.188	0.043	0.108	0.028	0.229	0.039	0.208	0.312	0.261	
	0.090	0.212	0.087	0.195	0.059	0.194	0.045	0.102	0.034	0.212	0.031	0.177	0.242	0.212	
Average														0.244	
% remaining GAPDH	34.38	95.27	30.90	76.85	21.99	76.64	14.07	43.16	15.96	124.61	22.77	110.04	115.62	106.72	
	35.04	85.05	30.20	78.90	26.83	77.83	17.89	50.55	17.97	111.89	19.82	117.80	113.20	99.25	
	35.78	88.09	33.89	81.53	23.63	77.22	17.52	44.31	11.65	93.92	15.88	85.18	127.93	107.09	
	37.05	86.90	35.70	79.80	24.21	79.76	18.34	41.73	14.03	86.94	12.88	72.58	99.13	86.94	
Average	**35.56**	**88.83**	**32.67**	**79.27**	**24.17**	**77.86**	**16.96**	**44.94**	**14.90**	**104.34**	**17.84**	**96.40**	**113.97**	**100.00**	
St dev.	1.14	4.47	2.58	1.95	2.01	1.36	1.95	3.89	2.70	17.12	4.35	21.11	11.81	9.42	

Table D.2: The raw data and calculations obtained from the KDalert GAPDH assay from the RBE4 confluent cells 48 h after transfection. LIN350 and RNAiMAX (RMAX) with anti-GAPDH (T) or negative control (NT) siRNA at 50 or 100 nM concentrations and N/P 10 or 30 (for LIN350) formed the nanoparticles. Untreated cells (Untr.) and MBG water + Master Mix (Blank) were included as controls. Absorbance was measured at 615 nm (A_{615}) 15 minutes after adding the Master Mix, and ΔA615 and % remaining GAPDH of the untreated control cells were calculated for each sample using these absorbance values. Cell density was 30,000 cells/well.

	LIN350 50 nM				LIN350 100 nM				RMAX 50 nM		Untr.	Blank
	T	T	T	NT	T	T	T	NT	T	NT		
N/P	**10**	**30**	**60**	**60**	**10**	**30**	**60**	**60**				
A_{615}	0.077	0.182	0.277	0.064	0.227	0.279	0.257	0.069	0.277	0.059	0.064	0.391
	0.063	0.244	0.257	0.093	0.257	0.258	0.270	0.061	0.280	0.061	0.060	0.377
	0.061	0.194	0.237	0.063	0.200	0.252	0.271	0.063	0.263	0.061	0.060	0.381
Average												0.383
ΔA$_{615}$ (blank - sample)	0.306	0.201	0.106	0.319	0.156	0.104	0.126	0.314	0.106	0.324	0.319	
	0.320	0.139	0.126	0.290	0.126	0.125	0.113	0.322	0.103	0.322	0.323	
	0.322	0.189	0.146	0.320	0.183	0.131	0.112	0.320	0.120	0.322	0.323	
Average											0.321	
% remaining GAPDH	95.05	62.57	33.07	99.19	48.44	32.33	39.11	97.82	33.11	100.78	99.10	
	99.66	43.19	39.05	90.23	39.20	38.80	35.25	100.09	31.89	100.19	100.47	
	100.22	58.93	45.40	99.63	57.06	40.82	34.88	99.47	37.40	100.16	100.44	
Average	**98.31**	**54.90**	**39.17**	**96.35**	**48.24**	**37.32**	**36.41**	**99.13**	**34.13**	**100.37**	**100.00**	
St. dev.	2.834	10.303	6.161	5.304	8.931	4.437	2.343	1.174	2.894	0.351	0.782	

Table D.3: The raw data and calculations obtained from the KDalert GAPDH assay from the RBE4 cells 48 h after transfection. LIN250, LIN250 w/HA, LIN350, LIN350 w/HA, DP$_{85}$ (4AM) and F$_a$=0 (2% PEG) with anti-GAPDH (T) or negative control (NT) siRNA at 50 or 100 nM concentrations and N/P 10 or 30 formed the nanoparticles. Untreated cells (Untr.) and MBG water + Master Mix (Blank) were included as controls. Absorbance was measured at 615 nm (A$_{615}$) 15 minutes after adding the Master Mix, and ΔA615 and % remaining GAPDH of the untreated control cells were calculated for each sample using these absorbance values. Cell density was 5,000 cells/well. The table continues on the next page…

	LIN250		LIN250 w/HA			LIN350		LIN350 w/HA			Untr.	Blank
	T	NT	T	T	NT	T	NT	T	T	NT		
N/P	30	30	10	30	30	30	30	10	30	30		
A$_{615}$	0.201	0.069	0.068	0.070	0.069	0.218	0.076	0.071	0.070	0.068	0.066	0.368
	0.187	0.075	0.070	0.072	0.071	0.285	0.073	0.069	0.067	0.068	0.067	0.363
	0.221	0.070	0.069	0.071	0.070	0.237	0.074	0.075	0.072	0.071	0.066	0.369
Average												0.367
ΔA$_{615}$ (blank - sample)	0.166	0.298	0.299	0.297	0.298	0.149	0.291	0.296	0.297	0.299	0.300	
	0.179	0.292	0.297	0.294	0.296	0.082	0.294	0.298	0.299	0.299	0.300	
	0.145	0.296	0.298	0.296	0.296	0.130	0.293	0.291	0.295	0.295	0.301	
Average											0.300	
% remaining GAPDH	55.33	99.33	99.67	99.00	99.33	49.67	97.00	98.67	99.00	99.67	100.00	
	59.67	97.33	99.00	98.00	98.67	27.33	98.00	99.33	99.67	99.67	100.00	
	48.33	98.67	99.33	98.67	98.67	43.33	97.67	97.00	98.33	98.33	100.33	
Average	**54.44**	**98.44**	**99.33**	**98.56**	**98.89**	**40.11**	**97.56**	**98.33**	**99.00**	**99.22**	**100.11**	
St. Dev.	5.719	1.018	0.333	0.509	0.385	11.510	0.509	1.202	0.667	0.770	0.192	

Continued on next page

Table D.3 continues.

N/P	DP$_{85}$ (4AM)			F$_a$=0 (2% PEG)			siRNA	Untr.	Blank
	T 10	T 30	NT 30	T 10	T 30	NT 30			
A$_{615}$	0.065	0.067	0.067	0.068	0.070	0.066	0.065	0.066	0.368
	0.064	0.07	0.069	0.068	0.069	0.067	0.067	0.067	0.363
	0.062	0.068	0.068	0.067	0.067	0.069	0.066	0.066	0.369
Average									0.367
ΔA$_{615}$ (blank - sample)	0.302	0.300	0.300	0.299	0.297	0.300	0.301	0.300	
	0.302	0.297	0.298	0.299	0.298	0.300	0.300	0.300	
	0.305	0.299	0.298	0.299	0.300	0.298	0.301	0.301	
Average								0.300	
% remaining GAPDH	100.67	100.00	100.00	99.67	99.00	100.00	100.33	100.00	
	100.67	99.00	99.33	99.67	99.33	100.00	100.00	100.00	
	101.67	99.67	99.33	99.67	100.00	99.33	100.33	100.33	
Average	**101.00**	**99.56**	**99.56**	**99.67**	**99.44**	**99.78**	**100.22**	**100.11**	
St. dev.	0.577	0.509	0.385	0.000	0.509	0.385	0.192	0.192	

Table D.4: Raw data of the median fluorescence intensity values of Alexa 647 siRNA from the C6 cells, measured 5 h after transfection by flow cytometry. The data are presented in Figure 4.1A (Section 4.1.1). LIN350 and SB300 at N/P 10, 30 and 60 with a siRNA concentration of 50 nM were used. Naked siRNA (siRNA) and untreated cells (Untr.) were included as controls. The cell density was 10,000 cells/well.

	N/P	Parallel 1	Parallel 2	Parallel 3	Average	Stdev
LIN350	10	10.55	11.98	14.41	**12.3**	2.0
	30	17.99	19.27	18.37	**18.5**	0.7
	60	13.3	15.62	14.49	**14.5**	1.2
SB300	10	9.34	9.37	9.51	**9.4**	0.1
	30	14.1	15.2	13.31	**14.2**	0.9
	60	12.36	13.61	11.6	**12.5**	1.0
siRNA	-	0.22	0.22	0.22	**0.2**	0.0
Untr.	-	0.1	0.1	0.1	**0.1**	0.0

Table D.5: Raw data of the median fluorescence intensity values of Alexa 647 siRNA from the C6 cells, measured 5 h after transfection by flow cytometry. The data are presented in Figure 4.1B (Section 4.1.1). LIN350 and SB300 at N/P 30 and RNAiMAX were used along with Alexa 647 siRNA at 50 or 100 nM. Naked siRNA (siRNA) and untreated cells (Untr.) were included as controls. The cell density was 10,000 cells/well.

	siRNA concentration	Parallel 1	Parallel 2	Parallel 3	Average	Stdev
LIN350	50 nM	8.94	8.28	8.82	**8.7**	0.4
	100 nM	16.52	17.8	14.22	**16.2**	1.8
SB300	50 nM	15.34	18.69	17.31	**17.1**	1.7
	100 nM	26.44	24.71	23.24	**24.8**	1.6
RNAiMAX	50 nM	60.83	55.09	55.93	**57.3**	3.1
	100 nM	82.87	85.1	92.91	**87.0**	5.3
siRNA		0.25	0.31	0.27	**0.3**	0.0
Untr.		0.1	0.1	0.1	**0.1**	0.0

Table D.6: Raw data of the median fluorescence intensity values of Alexa 647 siRNA from the RBE4 cells, measured 5 h after transfection by flow cytometry. The data are presented in Figure 4.7 (Section 4.2.1.1). LIN250, LIN250 w/HA, LIN350, LIN350 w/HA, DP$_{85}$ (4AM) and F$_a$=0 (2% PEG) at N/P 10 and 30 with Alexa 647 siRNA concentration of 50 nM were used. Naked siRNA (siRNA) and untreated cells (Untr.) were included as controls. The cell density was 10,000 cells/well. LIN250 w/HA and LIN350 at N/P 30 had fewer than 10,000 cells in each parallel, seen from the notations.

	N/P	Parallel 1	Parallel 2	Parallel 3	Average	Stdev	Notation
LIN250	30	71.03	73.99	78.54	**74.52**	3.78	
LIN250 w/HA	10	56.62	58.05	51.99	**55.55**	3.17	
	30	35.8	32.82		**34.31**	2.11	Only 7,774 & 5,334 cells
LIN350	30	66.07	74.73		**70.40**	6.12	Only 6,218 & 8,203 cells
LIN350 w/HA	10	30.97	30.56	29.61	**30.38**	0.70	
	30	54.33	52.56	56.58	**54.49**	2.01	
DP85 (4AM)	10	53.47	58.08	51.64	**54.40**	3.32	
	30	133.33	127.15	125.91	**128.80**	3.97	
Fa=0 (2%PEG)	10	127.28	125.67	121.36	**124.77**	3.06	
	30	93.42	93.5	90.21	**92.38**	1.88	
siRNA		0.43	0.43	0.41	**0.42**	0.01	
Untr.		0.1	0.1	0.1	**0.10**	0.00	

Table D.7: Raw data of the median fluorescence intensity values of Alexa 647 siRNA from the RBE4 cells, measured 5, 24, 48, 72 and 96 h (Day 0-4) after transfection by flow cytometry. The data are presented in Figure 4.8 (Section 4.2.1.2). LIN350 and SB300 at N/P 10, 30 and 60 with Alexa 647 siRNA at 50 nM were used. Naked siRNA (siRNA) and untreated cells (Untr.) were included as controls. The cell density was 10,000 cells/well.

	Day0	Day1	Day2	Day3	Day4
LIN350	119.35	27.31	3.27	0.89	0.84
	120.25	26.69	3.34	0.79	0.85
	124.88	28.82	3.27	0.78	0.86
Average	**121.49**	**27.61**	**3.29**	**0.82**	**0.85**
St. Dev.	2.97	1.10	0.04	0.06	0.01
SB300	157.35	41.15	7.74	1.52	1.23
	141.5	42.82	8.79	1.75	1.2
	146.68	43.08	8.57	1.89	1.55
Average	**148.51**	**42.35**	**8.37**	**1.72**	**1.33**
St. Dev.	8.08	1.05	0.55	0.19	0.19
Untreated	0.1	0.1	0.1	0.1	0.1
	0.1	0.1	0.1	0.1	0.1
	0.1	0.1	0.1	0.1	0.1
Average	**0.1**	**0.1**	**0.1**	**0.1**	**0.1**

Table D.8: Raw data of the median fluorescence intensity values of R123 from the C6 cells, measured 48 h after transfection by flow cytometry. The data are presented in Figure 4.3 (Section 4.1.3). LIN350 and SB300 at N/P 30 with anti-Abcb1a (T) or negative control (NT) siRNA at 50 nM were used. Naked chitosan (Naked), naked siRNA (siRNA) and untreated cells (Untr.) were included as controls. The cell density was 7,500 cells/well.

		Parallel 1	Parallel 2	Parallel 3	Average	Stdev
LIN350	T	109	107	133	**116**	14.5
	NT	127	115	116	**119**	6.7
	Naked	123	122	118	**121**	2.6
SB300	T	121	127	115	**121**	6.0
	NT	135	125	124	**128**	6.1
	Naked	116	121	113	**117**	4.0
siRNA	-	103	101	101	**102**	1.2
Untr.	-	104	98	101	**101**	3.0

Table D.9: Raw data of the median fluorescence intensity values of R123 from the C6 cells, measured 48 h after transfection by flow cytometry. The data are presented in Figure 4.4 (Section 4.1.3). Untreated cells (Normal C6) and cells cultured with doxorubicin-containing medium for five weeks (C6 w/doxorubicin) were used. The cell density was 7,500 cells/well.

	Parallel 1	Parallel 2	Parallel 3	Parallel 4	Average	Stdev
Normal C6	1.46	1.77	1.64	1.49	**1.59**	0.14
C6 w/doxorubicin	2.02	2.44	2.07	2.26	**2.20**	0.19

Table D.10: Raw data of the median fluorescence intensity values of R123 from the C6 cells, measured 48 h after transfection by flow cytometry. The data are presented in Figure 4.5 (Section 4.1.3). LIN350 and SB300 at N/P 30 and RNAiMAX with anti-Abcb1a (T) or negative control siRNA at 100 nM were used. Untreated cells with or without verapamil (Untr. And Untr w/verapamil) were included as controls. The cell density was 7,500 cells/well.

		Parallel 1	Parallel 2	Parallell 3	Average	St. Dev.
LIN350	T	10.47	13.18	11.66	**11.8**	1.36
	NT	7.34	8.12	7.57	**7.7**	0.40
SB300	T	11.44	10.04	9.72	**10.4**	0.91
	NT	7.61	6.66	6.49	**6.9**	0.60
RNAiMAX	T	12.91	13.05	11.63	**12.5**	0.78
	NT	4.53	4.45	4.28	**4.4**	0.13
Untr.		6.49	4.50	4.98	**5.3**	1.04
Untr. w/verapamil		692	681	696	**690**	7.94

Table D.11: Raw data of the median fluorescence intensity values of R123 from the RBE4 cells, measured 48 h and 96 h after transfection by flow cytometry. The data are presented in Figure 4.11 (Section 4.2.3.1). Chitosans: LIN250, LIN250 w/HA, LIN350, LIN350 w/HA, DP_{85} (4AM) and $F_a=0$ (2% PEG). siRNAs: anti-Abcb1a (T) and negative control (NT) at 100 nM. Untreated cells (Untr.) were included as a control. The cell density was 7,500 cells/well.

48 h	LIN350		LIN350 w/HA		SB300		$F_a=0$ (2% PEG)		DP_{85} (4AM)		Untr.
	T	NT	T	NT	T	NT	T	NT	T	NT	
	76.51	16.46	8.28	6.90	21.91	7.55	12.92	3.60	5.84	4.33	4.50
	76.41	15.88	7.16	4.38	28.84	8.14	10.17	5.70	6.31	4.95	3.79
	106.66		7.44	3.99	19.86	6.39	8.02	5.87	5.66	3.76	3.65
Average	**86.53**	**16.17**	**7.63**	**5.09**	**23.54**	**7.36**	**10.37**	**5.06**	**5.94**	**4.35**	**3.98**
St. Dev.	17.44	0.41	0.58	1.58	4.71	0.89	2.46	1.26	0.34	0.60	0.46
96 h	LIN300		LIN350 w/HA		SB300		$F_a=0$ (2% PEG)		DP_{85} (4AM)		Untr.
	T	NT	T	NT	T	NT	T	NT	T	NT	
	11.98	6.16	3.55	2.85	22.24	4.48	3.28	3.85	3.18	2.99	3.32
	25.92	8.66	3.88	3.16	29.65	4.98	3.64	4.15	6.27	2.96	4.30
	21.96	7.42	3.93	3.86	25.28	4.94	3.76	3.51	4.84	3.14	
Average	**19.95**	**7.41**	**3.79**	**3.29**	**25.72**	**4.80**	**3.56**	**3.84**	**4.76**	**3.03**	**3.81**
St. Dev.	7.18	1.25	0.21	0.52	3.72	0.28	0.25	0.32	1.55	0.10	0.69

Table D.12: Raw data of the median fluorescence intensity values of R123 from the RBE4 cells, measured 43, 48, 53 and 72 h after transfection by flow cytometry. The data are presented in Figure 4.13 (Section 4.2.3.2). LIN350 and SB300 at N/P 30 with anti-Abcb1a (T) or negative control (NT) siRNA at 50 nM were used. Untreated cells (Untr) were included as a control. The cell density was 7,500 cells/well.

	43 h			48 h			53 h			72 h		
	T	NT	Untr	T	NT	Untr	T	NT	Untr	T	NT	Untr
	34.09	5.71	4.17	19.94	5.27	4.17	24.81	5.6	3.91	56.54	7.42	4.95
LIN350	35.14	6.94	3.68	23.9	9.53	3.68	31.64	5.81	3.68	56.42	8.22	3.25
	33.33	6.68	4.25	34.36	8.94	4.25	27.88	7.27	3.9	66.24	15.2	4.07
Average	**34.19**	**6.44**	**4.03**	**26.07**	**7.91**	**4.03**	**28.11**	**6.23**	**3.83**	**59.73**	**10.28**	**4.09**
St. Dev.	0.91	0.65	0.31	7.45	2.31	0.31	3.42	0.91	0.13	5.64	4.28	0.85

Table D.13: Raw data of the median fluorescence intensity values of R123 from the RBE4 cells, measured 24, 44, 72, 96, 120 and 168 h after the first transfection by flow cytometry (Day 1, 2, 3, 4, 5 and 7, respectively). The data are presented in Figure 4.12 (Section 4.2.3.2). The cells were transfected with LIN350 at N/P 30 with anti-Abcb1a (T) or negative control (NT) siRNA at 100 nM one (T1, NT1), two (T", NT2) or three times (T3, NT3). Untreated cells (Untr) were included as a control. The cell density was 7,500 cells/well. The values given here are averages of the three parallels from each measurement.

	T1	NT1	T2	NT2	T3	NT3	Untr.
Day1	**6.32**	**5.64**	**5.59**	**4.78**	**5.46**	**4.40**	**3.52**
St. Dev.	0.20	1.41	0.29	0.32	0.50	0.39	0.49
Day2	**11.77**	**5.82**	**9.41**	**5.57**	**9.05**	**4.60**	**3.77**
St. Dev.	1.33	0.51	1.52	1.20	1.22	0.48	0.12
Day3	**30.60**	**10.64**	**35.51**	**12.01**	**35.88**	**10.73**	**8.14**
St. Dev.	2.59	0.48	1.11	1.48	3.81	1.58	1.27
Day4	**13.31**	**8.53**	**20.93**	**12.02**	**28.52**	**12.68**	**10.12**
St. Dev.	1.96	0.61	1.43	1.67	6.40	1.02	2.63
Day5	**12.47**	**7.51**	**10.02**	**5.28**	**25.96**	**6.38**	**4.61**
St. Dev.	2.56	2.45	0.41	0.01	5.34	0.99	0.91
Day7	**8.33**	**6.69**	**9.71**	**6.96**	**11.51**	**6.41**	**4.39**
St. Dev.	1.72	0.60	2.32	0.13	3.46		0.22

Table D.14: Raw data from the kinetics experiment, showing the values for all parallels from each day.

Day 1	T1	NT1	T2	NT2	T3	NT3	Untr.
LIN350	6.23	4.84	5.69	5.12	6.03	3.96	3.27
	6.55	4.81	5.82	4.73	5.27	4.72	3.20
	6.17	7.26	5.27	4.48	5.08	4.51	4.09
Average	**6.32**	**5.64**	**5.59**	**4.78**	**5.46**	**4.40**	**3.52**
St. Dev.	0.20	1.41	0.29	0.32	0.50	0.39	0.49

Day 2	T1	NT1	T2	NT2	T3	NT3	Untr.
LIN350	13.30	5.26		4.56	10.40	4.68	1.20
	11.10	6.24	10.48	6.89	8.71	5.03	1.01
	10.90	5.97	8.33	5.26	8.03	4.09	0.97
Average	**11.77**	**5.82**	**9.41**	**5.57**	**9.05**	**4.60**	**1.06**
St. Dev.	1.33	0.51	1.52	1.20	1.22	0.48	0.12

Note day 2: T2, Parallel 1 had a median FI value of 65, and was not included in the results.

Day 3	T1	NT1	T2	NT2	T3	NT3	Untr.
LIN350	27.79	10.64	36.78	10.89	40.22	10.10	9.13
	31.14	11.12	34.78	11.45	34.36	9.56	8.57
	32.88	10.16	34.96	13.69	33.07	12.52	6.71
Average	**30.60**	**10.64**	**35.51**	**12.01**	**35.88**	**10.73**	**8.14**
St. Dev	2.59	0.48	1.11	1.48	3.81	1.58	1.27

Day 4	T1	NT1	T2	NT2	T3	NT3	Untr.
LIN350	15.46	8.12	19.9	11.22	24.65	12.17	7.77
	11.61	8.24	20.33	13.94	35.90	12.01	12.96
	12.86	9.24	22.56	10.91	25.00	13.85	9.63
Average	**13.31**	**8.53**	**20.93**	**12.02**	**28.52**	**12.68**	**10.12**
St. Dev.	1.96	0.61	1.43	1.67	6.40	1.02	2.63

Day 5	T1	NT1	T2	NT2	T3	NT3	Untr.
LIN350	9.52	6.07	10.50	5.27	22.18	5.98	4.65
	13.81	10.34	9.82	5.29		5.65	3.69
	14.09	6.12	9.75		29.73	7.50	5.50
Average	**12.47**	**7.51**	**10.02**	**5.28**	**25.96**	**6.38**	**4.61**
St. Dev.	2.56	2.45	0.41	0.01	5.34	0.99	0.91

Note day 5: NT2, Parallel 3 had a median FI value of 12.6. T3, Parallel 2 had a median Fi value of 11.5. These were not included in the results.

Day 7	T1	NT1	T2	NT2	T3	NT3	Untr.
LIN350	8.76	7.12	8.07		15.48		4.57
	6.44	6.00	11.35	6.86	9.15	6.41	4.14
	9.80	6.94		7.05	9.89		4.46
Average	**8.33**	**6.69**	**9.71**	**6.96**	**11.51**	**6.41**	**4.39**
St. Dev.	1.72	0.60	2.32	0.13	3.46		0.22

Note day 7: T2, parallel 3 had a median FI value of 28. NT2, parallel 1 had a median FI value of 12. NT3, parallels 1 and 3 had median FI values of 12.2 and 16.4. These values were not included in the results

Table D.15: Ct, mean Ct and 2ddct values as well as percentages Abcb1a mRNA of RBE4 cells from the RT-PCR experiments, obtained and calculated from the amplification plots of Abcb1a and ACTB mRNAs in RBE4, C6 px 4 and C6 px 19 cells.

	Ct	Mean Ct	2ddct	Average 2ddct	% mRNA of RBE4	Average	St. Dev.
Abcb1a **C6 px 4**	n.a	23.08	0.000		0	**0.000**	
	n.a	23.08	0.000		0		
	n.a	23.08	0.000		0		
C6 px 19	24.24	23.08	0.393		33.11895263	**25.704**	**6.46**
	24.25	23.08	0.316		26.62270288		
	24.20	23.08	0.206		17.37071392		
RBE4	22.87	23.08	1.244	1.186	104.9519487	**100.000**	**4.95**
		23.08					
	22.94	23.08	1.127		95.04805131		
ACTB **C6 px 4**	Ct 23.29	16.39					
	23.55	16.39					
		16.39					
C6 px 19	16.201	16.39					
	15.892	16.39					
	15.226	16.39					
RBE4	16.497	16.39					
	16.264	16.39					
	16.419	16.39					

E: RT-PCR amplification plots

This section presents the amplification plots that were the basis of the data presented in Table D.15, shown in Figure E.1 and E.2. These figures show *Abcb1a* and *ACTB* cDNA amplification, respectively, from the RBE4, C6 px 4 and C6 px 19 cell samples.
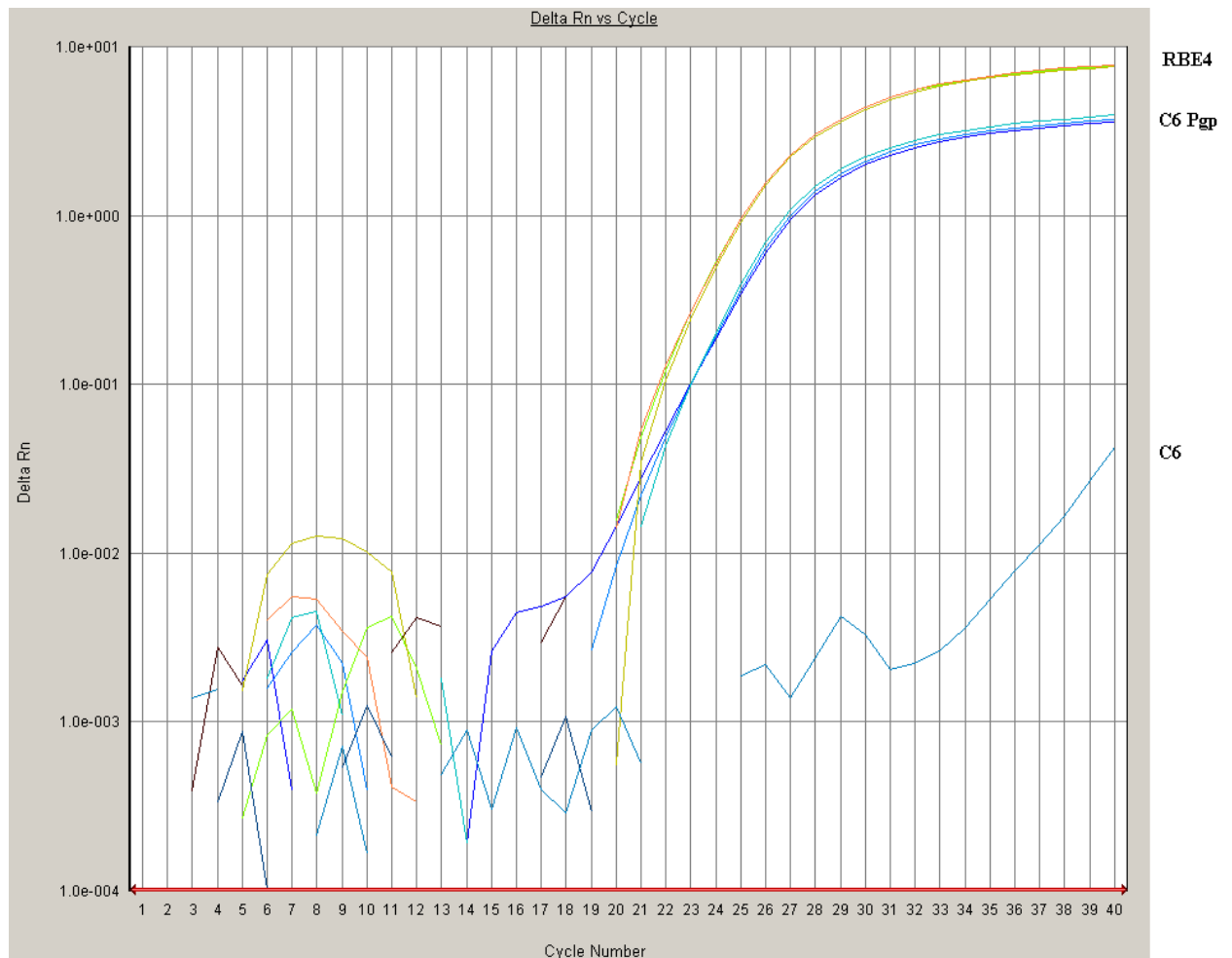

Figure E.1: RT-PCR amplification plot of the Abcb1a cDNA, showing a comparison between the C6 px 4 (C6, blue line bottom right), C6 px 19 (C6 pgp, blue curve top) and RBE4 (yellow curve). The amplification curves from RBE4 and C6 px 19 cells extend above the zero value of Delta Rn, and are therefore positive for Abcb1a mRNA. RBE4 cells had a higher level of Abcb1a mRNA, seen by the earlier amplification given by the cycle number. The C6 cells from px 4 samples did not contain Abcb1a mRNA.
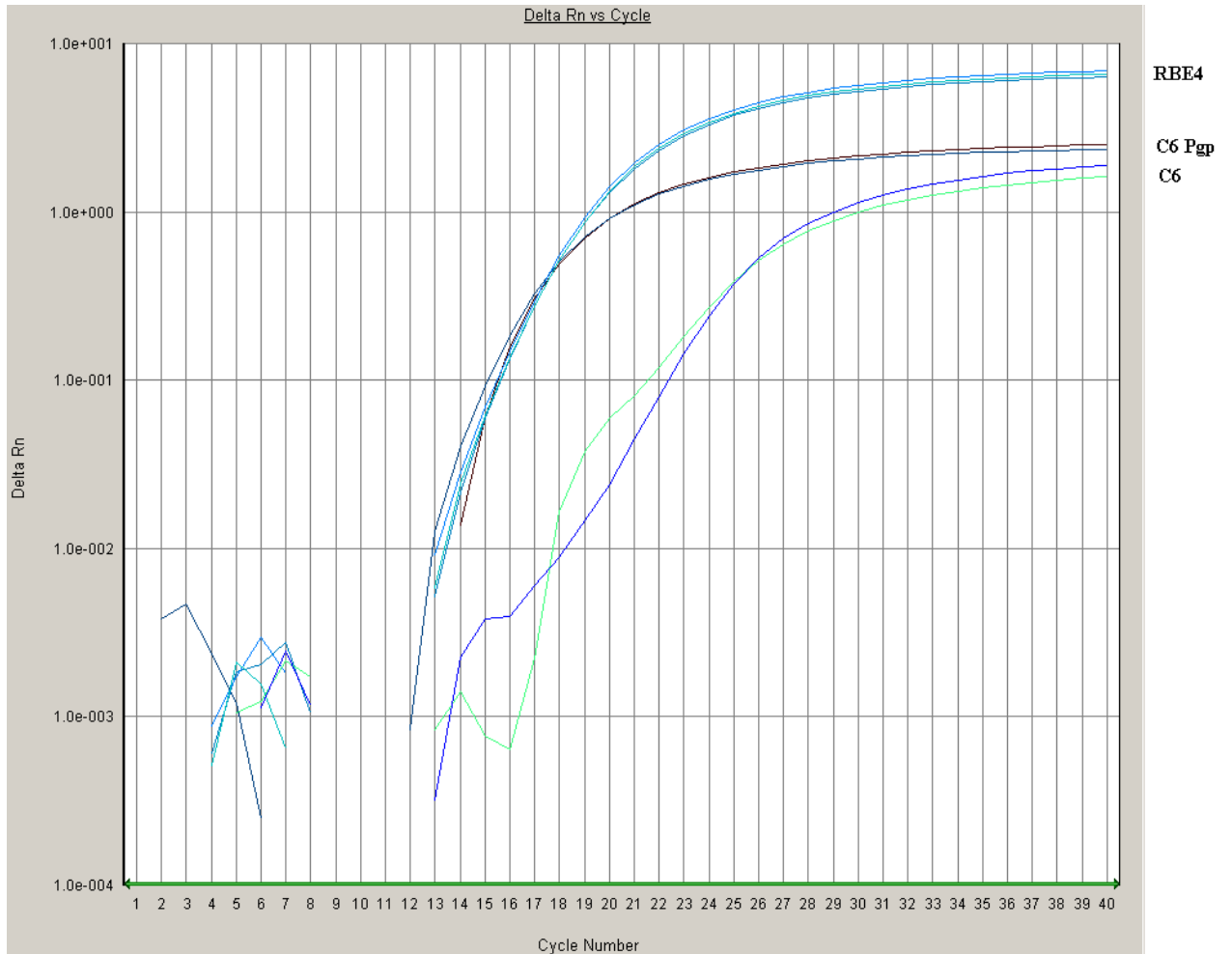
Figure E.2: RT-PCR amplification plot of the ATCB internal control cDNA, showing a comparison between C6 px 4 (C6, green and blue curve), C6 px 19 (C6 pgp, black curves) and RBE4 samples (turquoise curves). The RBE4 samples had higher amounts of ATCB mRNA, as seen by the earlier amplification of the cDNA, whereas C6 px 4 had the lowest levels of ATCB mRNA.